

Systematic Analysis of Unmanned Aerial Vehicle (UAV) Derived Product Quality

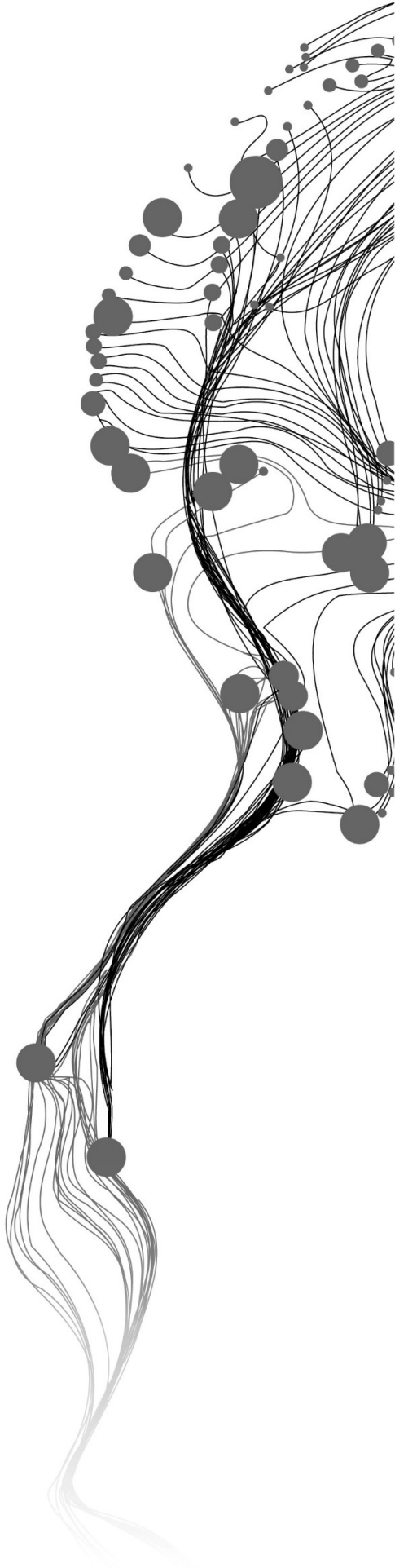
ASGAN RIZA NASRULLAH

February 2016

SUPERVISORS:

dr.ing. Markus Gerke

dr. Francesco Nex



Systematic Analysis of Unmanned Aerial Vehicle (UAV) Derived Product Quality

ASGAN RIZA NASRULLAH

Enschede, the Netherlands, February 2016

Thesis submitted to the Faculty of Geo-Information Science and Earth
Observation of the University of Twente in partial fulfilment of the
requirements for the degree of Master of Science in Geo-information Science
and Earth Observation.

Specialisation: Geoinformatics

SUPERVISORS:

dr.ing. Markus Gerke

dr. Francesco Nex

THESIS ASSESSMENT BOARD:

prof.dr.ir. M.G. Vosselman (Chair)

prof.dr.ing. H.J. Przybilla (External Examiner, Bochum University of Applied
Sciences, Germany)

DISCLAIMER

This document describes work undertaken as part of a programme of study at the Faculty of Geo-Information Science and Earth Observation of the University of Twente. All views and opinions expressed therein remain the sole responsibility of the author, and do not necessarily represent those of the Faculty.

ABSTRACT

Unmanned aerial vehicles are used today as a standard tool to derive very high-resolution geospatial data (e.g. 3D height models, orthophotos). The workflow from images to products is very often just an easy-to-use black box processing. However, in contrast to traditional photogrammetry with very high-quality hardware and proven processing standards, in the case of current UAV-based production such reliable hardware and processes are not available. This means that the user does not have good control over the achievable quality, or in other words, the user does not know which parameters influence the final product quality. This thesis will show and discuss results of a systematic analysis of the most mentioned influencing parameters. In the block adjustment process, several tests conducted to analyse the influence of camera lens types, quality of image initial positions, number and distribution of ground control points, flight altitudes, motion blur disturbances, additional cross strips and oblique configurations, and the percentage of forward overlapping images. Several tests also arranged to check the influence of some parameters on the dense image matching results such as image exposure, motion blur, and surface covers. Various flight configurations have been carried out using three different UAV platforms, in total performing 19 flights above a test area in Gronau, Germany. The results demonstrate that accurate initial positions and the number and distribution of ground control points become the main influencing parameters in reducing the deformation in the block adjustment processes. The impact of flight altitude changes varies with different types of lenses. Motion blurred images and forward overlap reductions tend to aggravate the achievable accuracy. Additional cross strips are only beneficial in the bundle block adjustment with fewer control points while oblique configurations give a better achievable accuracy in most scenarios. A rigid and textured surface cover will generate a denser yet more accurate point cloud than a non-rigid surface cover.

Keywords: UAV, photogrammetry, structure from motion, accuracy assessment, block deformation

ACKNOWLEDGEMENTS

In the name of ALLAH, the Most Gracious, the Most Merciful. *بِسْمِ اللَّهِ الرَّحْمَنِ الرَّحِيمِ*

I am using this opportunity to express my sincere thankfulness and appreciation to my supervisors dr.ing. Markus Gerke and dr. Francesco Nex. Their aspirational guidance, invaluable constructive criticism, and friendly advice have helped me to complete this research. I would also like to express my sincere gratitude to dr.ir. S.J. Oude Elberink for his valuable insights during the early process of this research.

I would also like to thank Ioulia Leventi, Watse S. Siderius, Caroline M. Gevaert, Triyoga Widiastomo, Yohannes K. Boedihardja, and John R. Bergado for their helpful assistance during data acquisition process.

I would like to extend my thanks to the Ministry of Energy and Mineral Resources of the Republic of Indonesia for provisioning such valuable scholarship. It provides me a lifetime opportunity to study and work together with a multicultural environment in ITC. Thanks to all my classmates of GFM 2014-2016 for their support in various matters during past one and a half year.

My utmost gratitude to my beloved family and my wife Meirisa Hilda Sukasa for their immeasurable support during my study. Finally yet importantly, I would like to dedicate my thesis to my son Prabaswara Rayyan Nasrullah. I know heaven is a beautiful place because they've got you.

TABLE OF CONTENTS

Table of Contents.....	i
List of Figures	iii
List of Tables.....	v
Abbreviations	vi
1. Introduction.....	1
1.1. Motivation and problem statement.....	1
1.2. Research identification.....	2
1.2.1. Research objectives.....	2
1.2.2. Research questions.....	2
1.2.3. Innovation.....	3
1.3. Thesis structure	3
2. Literature Review.....	4
2.1. Brief history of UAV-based photogrammetry	4
2.2. UAV classification	4
2.3. The influencing parameters in the derived UAV-based photogrammetry product quality	5
2.3.1. The use of non-metric camera.....	5
2.3.2. Motion blur.....	7
2.3.3. Acquisition mode.....	8
2.3.4. Flight altitude	8
2.3.5. RTK GNSS-based Direct Georeferencing.....	9
2.3.6. Image overlap	10
2.3.7. Flight pattern	10
2.3.8. Distribution of GCPs.....	11
2.4. Modulation Transfer Function	11
2.5. Structure from Motion.....	12
3. Methodology.....	14
3.1. Overview	14
3.2. Research preparation.....	15
3.2.1. Overlapped area estimation.....	15
3.2.2. Expected motion blur.....	16
3.2.3. Theoretical vertical accuracy	16
3.2.4. Empirical Error Measurements of the Residual in Checkpoints.....	17
3.3. Data acquisition.....	18
3.4. Data preparation	20
3.5. Data processing and analysis.....	21
3.5.1. Ground Sampling Distance and Ground Resolved Distance calculations	21
3.5.2. Automatic aerial triangulation and bundle block adjustment	23
3.5.3. Influencing parameters analysis	23
3.5.4. Cross flight and oblique images comparison.....	23
3.5.5. Point cloud comparison.....	24
4. Study Area and Data Acquisition.....	26
4.1. Study area	26
4.2. Flight planning.....	26
4.3. GNSS survey	30
4.4. UAV image data acquisition.....	31
5. Results.....	33

5.1.	Data Preparation.....	33
5.1.1.	GNSS Survey.....	33
5.1.2.	The resulting UAV images	34
5.2.	Ground Sampling Distance and Ground Resolved Distance	35
5.3.	Theoretical vertical accuracy.....	37
5.4.	Impact of GPS initial position on the resulting accuracy of BBA.....	37
5.4.1.	Experiment results.....	37
5.4.2.	Main findings.....	39
5.5.	Impact of distribution and number of GCPs on the resulting accuracy of BBA	40
5.5.1.	Experiment results.....	40
5.5.2.	Main findings.....	44
5.6.	Impact of flight altitude on the BBA accuracy.....	44
5.6.1.	Experiment results.....	44
5.6.2.	Main findings.....	46
5.7.	Impact of Motion blur on the BBA accuracy	46
5.7.1.	Experiment results.....	46
5.7.2.	Main findings.....	47
5.8.	Impact of cross flights and oblique images addition on the BBA accuracy.....	47
5.8.1.	Experiment results.....	47
5.8.2.	Main findings.....	50
5.9.	Impact of flight overlaps on the BBA accuracy	50
5.9.1.	Experiment results.....	50
5.9.2.	Main findings.....	54
5.10.	The influence of land surfaces on the accuracy of the resulting DEM	54
5.10.1.	Experiment results.....	54
5.10.2.	Main findings.....	59
6.	Discussion.....	60
7.	Conclusion and Recommendation.....	63
7.1.	Conclusion.....	63
7.2.	Recommendation.....	64
	List of References.....	65
	Appendices	71

LIST OF FIGURES

Figure 1. Examples of UAV types	5
Figure 2. Types of symmetrical distortions	6
Figure 3. Sharp image and motion-blurred image	7
Figure 4. RTK GNSS-based direct georeferencing.....	9
Figure 5. Sample of flight line with 60%, 75%, and 90% forward overlap.....	10
Figure 6. MTF patterns at several attenuation	11
Figure 7. Flow diagram of the research.....	14
Figure 8. Theoretical image motion.....	16
Figure 9. Aerial triangulation relationships.....	17
Figure 10. Real-Time Kinematic (RTK) methods.....	19
Figure 11. Ebee RTK configurations	19
Figure 12. Two back-and-forth flights in one flight configuration	20
Figure 13. Data preparation workflow	20
Figure 14. Data processing and analysis workflow	21
Figure 15. Normal images from Aibot X6 and strongly sharpened image from DJI Phantom 2.....	22
Figure 16. Cross flight pattern.....	23
Figure 17. Workflow of point cloud comparison.....	24
Figure 18. Nearest neighbourhood distance calculation	25
Figure 19. The study area	26
Figure 20. Aibot X6 flight configurations in Aibotix AiProFlight software.....	27
Figure 21. Example of targets: signalised target and natural targets: corner of concretes, manhole	31
Figure 22. UAV employed on the research: Aibot X6, DJI Phantom 2 Vision +, and Ebee RTK.....	32
Figure 23. The Siemens Star and Koren Chart.....	32
Figure 24. Distribution of the 3D control points for image acquisitions on 21 October 2015, 23 October 2015, and 27 November 2015	33
Figure 25. Distribution of 3D profile points and its resulting TIN	34
Figure 26. Inaccurate initial GCP marking due to the remaining error from lens distortion.....	35
Figure 27. Correlation of the motion blurs with the GRD.....	36
Figure 28. Residuals of XYZ at checkpoints on a block adjustment without GCPs	39
Figure 29. GCPs and checkpoints distributions	40
Figure 30. The resulting accuracy from different GCP scenarios	41
Figure 31. Deformation of point cloud in different number of GCPs.....	43
Figure 32. Differences in residuals at checkpoints in the 4-GCP configuration of Aibot X6.....	44
Figure 33. Impact of altitude on BBA accuracy	45
Figure 34. The resulting BBA accuracy from different flight altitudes with respect to GSD size	45
Figure 35. Average direction and magnitude of the reprojection error in DJI Phantom 2 camera and Aibot X6.....	46
Figure 36. The effects of motion blur on the resulting accuracy.....	47
Figure 37. Impact of cross flights and oblique images addition to the resulting BBA accuracy	49
Figure 38. The comparison of block deformation of the single flight, cross flights addition and oblique image configuration in 4-GCPs and undistributed 5-GCPs.....	50
Figure 39. The number of overlapping images in 80/50 overlap and 70/50 overlap of Aibot X6	51
Figure 40. The number of overlapping images in 80/50 overlap and 70/50 overlap of DJI Phantom 2 Vision+	51
Figure 41. The number of overlapping images in 70/40 overlap configuration of Ebee RTK	52

Figure 42. The comparison of resulting accuracies from 90/50, 80/50 and 70/50 percent image overlaps52

Figure 43. The resulting accuracy of Ebee RTK in 70/50 image overlaps.....53

Figure 44. The resulting Sigma of dense point cloud compared with its fitting plane.....55

Figure 45. Number of automatic tie points produced on paving setts and grasses.....56

Figure 46. The residuals at checkpoints of dense point clouds obtained with 2D-search method57

Figure 47. Residuals at checkpoints in the range of 80 to 90 and 175 to 185 of the 3D reference heights .58

Figure 48. The distance measurement error in 2D search method.....58

LIST OF TABLES

Table 1. The tested parameters	15
Table 2. Aibot X6, DJI Phantom 2 Vision+ and Ebee RTK specification comparison	27
Table 3. UAV flight configuration	28
Table 4. List of flight configurations used to analyse the tested parameters	29
Table 5. The expected motion blur on the image	29
Table 6. The expected forward overlap of the Aibot X6 in cruising mode	30
Table 7. Forward overlap percentage of the derived image-sets	30
Table 8. GSD and GRD comparison	36
Table 9. Theoretical vertical accuracy	37
Table 10. Residuals on the checkpoints of the BBA without ground control point	38
Table 11. Residuals at checkpoints of cross flight and oblique image configurations	48
Table 12. The measurement result of densified point clouds compared with its 2.5D Quadratic plane	55
Table 13. The results of the nearest neighbour search	57

ABBREVIATIONS

2D	2 Dimensional
3D	3 Dimensional
ALS	Aerial Laser Scanning
AAT	Automatic Aerial Triangulation
BBA	Bundle Block Adjustment
DSM	Digital Surface Model
DTM	Digital Terrain Model
DGPS	Differential Global Positioning System
GCP	Ground Control Point
GNSS	Global Navigation Satellite System
GPS	Global Positioning System
GRD	Ground Resolved Distance
GSD	Ground Sampling Distance
IMU	Inertial Measuring Unit
MTF	Modulation Transfer Function
RTK	Real Time Kinematic
SfM	Structure from Motion
UAV	Unmanned Aerial Vehicle

1. INTRODUCTION

1.1. Motivation and problem statement

Civil Unmanned Aerial Vehicle (UAV) technology has become commercially available at a very reasonable price for a number of diverse applications. MarketsandMarkets (2015) reveals global UAV market revenue in 2015 is valued at \$10.1 Billion and expected to grow up to \$14.9 Billion in 2020. In the photogrammetry and remote sensing fields, UAVs facilitate novel solutions for very high-resolution image data collection. Entrepreneurship between geomatic and computer vision has established a new paradigm in aerial remote sensing and mapping approaches (Colomina, Blázquez, Molina, Parés, & Wis, 2008). Seemingly, UAV technology already has a future; as suggested by the Government of Trinidad and Tobago in their tender notice announcement for a UAV System “to provide coloured map and imagery products to serve the identical purpose of conventional aerial survey and to satisfy the needs of a demanding spatial data market” (Trinidad and Tobago. Ministry of Finance and the Economy, 2013).

Manned aircraft is one of the well-established platforms for numerous remotely sensed 3D data acquisitions. 3D point clouds generated from stereo images or laser scanners are used in several domains such as 3D building modeling reconstruction (Caroti, Martínez-Espejo Zaragoza, & Piemonte, 2015; Vosselman & Dijkman, 2001), structural damage assessment (Dong & Shan, 2013), and documentation and preservation of heritage building or archaeological areas (Chiabrando, Nex, Piatti, & Rinaudo, 2011). Although ALS can provide an accurate point cloud, the major drawbacks of laser scanner datasets are that they are expensive and unable to acquire specular surfaces.

The benefits of UAV over manned aerial vehicle technology are varied. UAV itself does not require a pilot to be on board. Due to this, UAV is not constrained by a pilot’s physical limits. They can be autonomously programmed to complete repetitive yet precise missions, and also have the capability to enter unsafe environments (Unmanned Aerial Vehicle System Association, 2015). Conventional aircraft operate from existing airfields, sharing airspace with all other air traffic. Eventually, this will lead to operational costs that are too high for most science projects or surveying practices in small areas. Its cost-effectiveness compared with manned aerial vehicles makes UAV technology attractive. Project expenditure related to aerial survey flight can be minimised. Moreover, UAV has high repeatability and flexibility in the data acquisition process.

However, UAV technology has a few disadvantages. Payload limitations have always been a major issue for UAVs. Small coverage for each image will increase the number of images that need to be processed. UAVs tend to produce significant geometric distortion due to the use of non-metric cameras (Tahar & Ahmad, 2013). Besides these technical limitations, UAV technology also has drawbacks from a regulatory aspect. Countries such as Thailand and the United States have strict rules on the use of UAVs; which may even diminish its competitive advantages (Fairfield, 2015; Koebler, 2013; Who, 2013). Other nations such as Canada, Germany, Australia, New Zealand, Brazil, and the United Kingdom have been more UAV-friendly in their regulation (ArcadiaSky, 2015; Häcki, 2014). Nevertheless, many more countries in the world still have unclear policies regarding the use of UAVs.

As the payload capacity is a crucial point with low-altitude UAVs, miniaturisation of the sensors becomes inevitable. In traditional photogrammetry, metric large-frame cameras with a high accuracy GPS and IMU sensor are normally used. In the case of lightweight UAV-based production, no such reliable hardware can be attached. Due to its carriage limitations, data acquisition is mostly done by a light digital camera. Since the low-cost digital camera has not been designed for a photogrammetric purpose, this means that the user does not have a strong ability to control the derived 3D product quality.

Before generating final photogrammetry products such as DSM and orthophoto, it is necessary to take care of earlier associated chain processes such as Aerial Triangulation and Bundle Block Adjustment. These

stages are crucial to ensure the quality of the final product, as influencing parameters are involved in determining the output. Apart from random errors, an accumulated error from the influencing parameters can cause large block deformation. Further, the quality of dense image matching is affected by additional parameters such as surface textures and dark parts of the object (Remondino et al., 2013).

Nowadays, several algorithms mainly developed by the computer vision community have considerably sped up the image processing workflow. Different software packages are currently available for executing image orientation up to generating the 3D point cloud in an entirely automated way, in both open source and commercial products. Several publications have been issued in recent years, focusing on the integration of photogrammetry and Structure from Motion (SfM) in specific real case studies (Chiabrando et al., 2011; Remondino et al., 2013; Westoby, Brasington, Glasser, Hambrey, & Reynolds, 2012). Nevertheless, the complexity and diversity of the methods applied in each software product make it tough to do an in-depth analysis of the performance and reliability of the existing software.

Several parameters influencing the geometry of final UAV-based product quality have been investigated such as the quality of the sensor including geometric and radiometric distortion (Cramer, 2010; Vallet, Panissod, Streacha, & Tracol, 2011), flight modes (Eisenbeiss & Sauerbier, 2011), path planning (Bailey, 2012), and motion blur disturbances (Sieberth, Wackrow, & Chandler, 2014). However, most research has only considered one parameter and neglected the influence of other parameters on the results.

Therefore, systematic research assessing the quality of UAV derived products by considering all known influencing parameters needs to be conducted. Only by this approach, users can have an improved ability to control the quality of the derived product. This research has to be comprehensive, examining the impact of various aspects of the parameters in the associated process chain of UAV-based product generation. Moreover, this research is decisive in evaluating whether a UAV attached with a non-metric camera can reliably replace traditional photogrammetry methods in particular cases.

1.2. Research identification

This research will focus on the use of low-altitude civil UAVs attached with different types of digital cameras and lenses to evaluate the effect of each parameter in every step of generating UAV-based photogrammetry products. The proposed parameters to be tested are related to the optical sensor properties, flight speeds, image acquisition modes, motion blur disturbances, flight altitudes, flight overlaps, image initial position accuracies, as well as cross-flight patterns and oblique image configurations. The study is not only a one-to-one comparison between parameters to determine which one is the most influential parameter on the product quality, but also examines how each parameter responds to the different setups.

1.2.1. Research objectives

The general purposes of this study are (1) to improve the understanding of the actual influence of different variables on UAV-based photogrammetry parameters in the chain process of generating final products, and (2) to identify the most significant one for given scenarios.

1.2.2. Research questions

To achieve the objectives, the following related questions are defined:

- a. How does the theoretical Ground Sampling Distance (GSD) compare to the actual Ground Resolved Distance (GRD)?
- b. How does the theoretical vertical accuracy compare to the actual achievable accuracy?
- c. What is the influence of the initial image position on the resulting accuracy?
- d. How can different Ground Control Point scenarios affect the overall accuracy?
- e. How do the different flight altitudes affect the resulting accuracy?
- f. What is the effect of motion blur on photogrammetric image processing?

- g. To what extent can the different blocks consisting of different flight altitudes and directions affect the overall accuracy of the self-calibration process?
- h. What is the significance of oblique image acquisition to the block deformation refinement?
- i. What is the impact of the number of overlapping images on the quality of image orientation?
- j. How efficient is the stop mode compared with the cruising mode, with regard to the resulting accuracy of and the time taken for the data acquisition?
- k. What parameters significantly influence the dense image matching process according to the pre-defined schemes?

1.2.3. Innovation

The novelty of this research is to provide an improved understanding of the actual influence of different variables, through a systematic analysis that takes into account the main influencing parameters in the chain process of deriving UAV-based photogrammetry products.

1.3. Thesis structure

Chapter 1 contains an introduction to the study, in the form of motivation and problem statements, research identification, and research structure. Research identification will be divided into three subsections, i.e., research objectives, research questions, and innovation.

Chapter 2 presents a broad literature review that was very useful for this study. A brief history of UAV-based photogrammetry, UAV classification, recent studies on the influencing parameters of UAV derived product quality and the concept of Structure from Motion will be discussed further in this chapter.

Chapter 3 consists of a detailed description of the methods used in this research. Generally, the research is arranged into four segments: general research preparation, data acquisition, data preparation, and data processing and analysis. A comprehensive process flow for each segment and the approaches used to complete the objectives are specifically described in this chapter.

Chapter 4 contains an overview of the study area chosen for the research, as well as general information regarding the process that has been conducted in the field during data acquisition. The data acquisition itself consists of three different phases: UAV flight planning, GNSS survey, and UAV image data acquisition.

Chapter 5 comprises detailed results of each step in the research. From the quality of the data obtained from the field works, data preparation, up to data processing and analysis of results including the results of all tests conducted during the research to check the impact of selected parameters on the achievable accuracy of the UAV-based photogrammetry product. Technical discussion regarding related experiment results is also contained in this chapter.

Chapter 6 consists of general discussion regarding the results and how to address each parameter tested, based on the findings of this research. Finally, a summary of the results and recommendations for further research are given in Chapter 7.

2. LITERATURE REVIEW

A review of the literature relevant to this thesis is given in this chapter. The first section will introduce the broader context of the history of UAV-based photogrammetry and civil UAV classification, followed by an examination of the influencing parameters on the final UAV-derived products. An overview of Structure from Motion will also be given later.

2.1. Brief history of UAV-based photogrammetry

Although nowadays most photogrammetry uses digital images for measurement, the concepts go back to earlier history, as far as 1480 when Leonardo da Vinci established the concept of perspective and projective geometry. The use of “photogrammetry” was advocated by the French geodesist Dominique François Jean Arago circa 1840, using Daguerreotype – the first “practical” photography – in front of the French Arts and Science Academy (The Center for Photogrammetric Training, 2008). In 1858, French photographer and balloonist Gaspard-Félix Tournachon captured the first known aerial photograph of the village of Petit Bicêtre near Paris, France from a hot-air balloon, 80 metres above the ground (Newhall, 1969). Since then, aerial pictures have been taken from various platforms including balloons, pigeons, kites, airplanes, and recently UAVs (Aerometrex, 2012; Colomina & Molina, 2014; Eisenbeiß, 2009).

In 1893, the German Engineer, Dr. Albert Meydenbauer was the first person to use the term “photogrammetry”. He designed his first camera in 1867 after discovering conventional cameras were not sufficient for photogrammetric purposes. This camera was used for the topographic mapping of Freiburg, Germany. Meydenbauer’s camera has the characteristics that are found in a metric camera, i.e., a permanently mounted lens, spirit levels for levelling up the camera, and fiducial marks for defining the image’s coordinate axes (The Center for Photogrammetric Training, 2008).

With the airplane invented by the Wright brothers in 1903, aerial photogrammetry seemingly found its perfect platform, and eventually to be the main platform for aerial photogrammetry for decades. Only five years after the invention of the airplane, the first aerial photogrammetry for mapping purposes was taken from a plane in 1908 by Italian Captain Cesare Tardivo (Aerometrex, 2012).

UAVs were first developed for military purposes, which today still accounts for a significant portion of current UAV research and development. In the early stages of UAV development, the first pilotless aircraft was built using A.M Low’s radio control in 1916 with its primary purpose as a target for gunnery practice. Soon after, the Hewitt-Sperry Automatic Airplane or “flying bomb” made its first flight, manifesting the concept of an unmanned aerial vehicle. The integrated evolution of circuitry and radio-controlled systems in the twentieth century has become the key development in UAV technology.

However, the potential of UAV for mapping industries was not revealed until the late twentieth century, when a research group performed a test with a three-metre length fixed-wing UAV equipped with a 6×6 medium format camera (Przybilla & Wester-Ebbinghaus, 1979). The second test was conducted in 1980 using a radio-controlled helicopter carrying a medium format Rolleiflex SLX camera (Wester-Ebbinghaus, 1980). Since then, the use of UAVs for civilian purposes as image and video recording tools in general or even remote sensing platforms offers extraordinary opportunities.

2.2. UAV classification

Although some literature refers generally to UAV as both powered and unpowered remotely controlled aerial systems (Eisenbeiß, 2009), the UAV in the context of this research is most similar to the definition of UAV by the American Institute of Aeronautics and Astronautics:

“An aircraft which is designed or modified not to carry a human pilot and is operated through electronic input initiated by the flight controller or by an onboard autonomous flight management control system that does not require flight controller intervention” (American Institute of Aeronautics and Astronautics, 2004).

UAVs are classified into two main categories: fixed-wing and rotary blade (Figure 1). Each class has its advantages and disadvantages. A fixed-wing UAV has better area coverage compared with the rotary blade UAV but has limitations regarding take-off/landing requirements; a fixed-wing UAV needs a sufficient runway strip for take-off/landing, unlike the rotary blade UAV which can perform vertical take-off/landing. A rotary blade UAV or propeller-based system can fly in every direction, horizontally and vertically, as well as hover in a fixed position. This flying feature makes rotary blade UAVs perfect for detailed survey and inspections works (Bailey, 2012). However, a major limitation of the rotary blade UAV is a shorter battery life due to the need to supply more machines than a fixed-wing UAV. Additionally, a hybrid UAV combining the advantages of both types of UAVs has begun to emerge on the market. This type of UAV is basically a fixed-wing with a vertical take-off/landing capability and has a longer battery life than a rotary blade UAV, by employing a tiltrotor as the main driver.

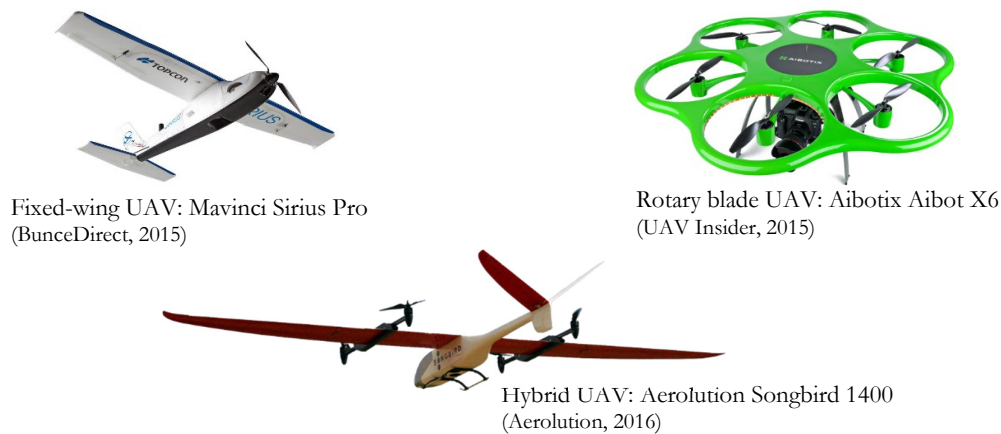


Figure 1. Examples of UAV types

2.3. The influencing parameters in the derived UAV-based photogrammetry product quality

2.3.1. The use of non-metric camera

Numerous studies using images acquired by UAVs have led to a continuous development of this technique for photogrammetric projects. A low-altitude UAV attached with a consumer digital camera can even produce a higher GSD than traditional photogrammetric techniques. Cost effectiveness compared with traditional photogrammetry has made it more attractive. However, due to the use of non-metric digital cameras, this technique raises significant problems concerning the resulting quality.

At the data acquisition stage, several problems can occur. Although the self-calibration process can conveniently optimise the internal camera parameters such as focal length and lens distortion, the camera exposure parameters such as shutter speed, lens aperture, and ISO also have a considerable impact on the image quality. Weather conditions can also worsen the situation. Ultra lightweight platform usage is prone to wind and vibration problems. Mild wind during data acquisition can cause imprecise image recording direction, and eventually insufficient image overlap. Vibration from the UAV's rotor-engine can be easily slithered to the camera, eventually increasing the blurriness. Light conditions during image acquisition can also exacerbate the complexity. Low light conditions demand a lower shutter speed or higher ISO to produce a normal exposure image. Both have their issues: by lowering the shutter speed, motion blur will emerge; by

increasing the ISO, image noises will come up. However, image noise does not merely come from a higher ISO; image noise could also come from sensor read noise and thermal noise (Martinec, 2008).

All rays of light from a single object point in the world would ideally converge to the same point in the image plane, creating a sharp image. In camera optics, however, the light rays could converge to different points due to lens geometry, called an optical aberration. The optical aberration is commonly found in standard photography lenses. Optical aberration impact varies with the wavelengths. This means that with an RGB sensor, a number of distortions from the specific lens are different in blue, green, and red wavelengths (Edmund Optics, 2014). Without taking into account the wavelengths of the illuminations, the resulting images of the distorted area are likely to have blur because the same blue, green, and red wavelengths do not correctly depict a single point in an RGB image as it should be in the real world.

Apart from an optical aberration, the optic geometry also creates another distortion. Ideally, a straight-line object should remain straight in the photo. However, due to the geometry of the lenses, the straight-line object looks bent in the picture. Although the lens distortion could be in irregular patterns, market camera lenses typically have symmetrical distortions. According to Mansurov (2013), three types of symmetrical distortions are commonly found in camera lenses: barrel/radial distortion, pincushion distortion, and moustache/wavy/complex distortion.

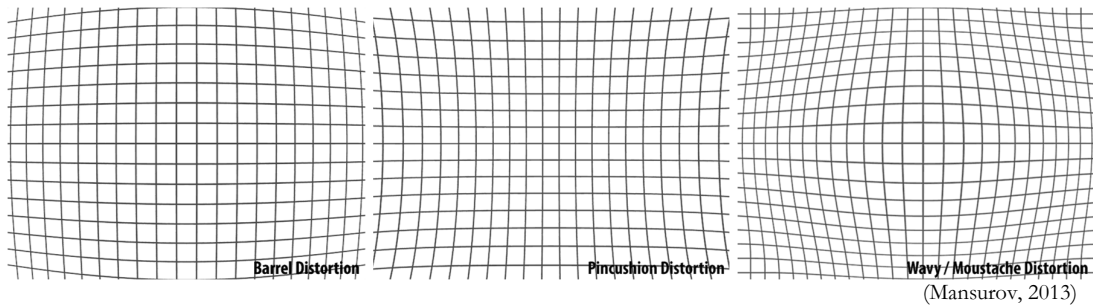


Figure 2. Types of symmetrical distortions

The barrel/radial distortion is mostly present in wide-angle lenses both prime and zoom lenses. Although it is impossible to eliminate this distortion, an optical element compensation can be used to decrease the effect of this distortion. Another method to shrink the influence of lens distortion is performing lens aberration correction using computer software in the post-acquisition step.

A camera has two mechanisms to control the amount of light to be captured by the sensor and forming exposure: the timing of the shutter curtain to open and close, and the lens diaphragm consists of multiple blades to control the amount of light allowed through the lens. The consequences of the shutter speed on the resulting image will be described later in the section of Motion blur. Meanwhile, the lens diaphragm has an inevitable feature: depth of fields. According to Leofoo (2000), depth of field is “the amount of distance between the nearest and the farthest objects that appear in acceptably sharp focus in a photograph”. The depth of field has a direct relationship with the use of two factors: the opening lens diaphragm and the focal length. Larger lens opening (apertures) such as $f/2.8$ or $f/3.5$ will create a narrow depth of field and thus the zone of sharpness is very limited. Further, an optical aberration will also occur in the large lens aperture (Mansurov, 2011). However, a shorter focal length will deepen the depth of field, creating more zone of sharpness.

Regarding the camera calibration process, there are several camera modelling approaches to introduce additional parameters for modelling the disparity between the ideal mathematical model of central perspective and the actual physical camera (Luhmann, Fraser, & Maas, 2015). In most cases, a standard model involving three radial distortions and two tangential distortions is sufficient in serving metric

purposes for rectilinear lens systems (Luhmann et al., 2015; Neale, Hessel, & Terpstra, 2011). However, this model is less accurate than a fisheye lens. Apart from standard models, a generic camera model (Rueß, Luber, Manthey, & Reulke, 2012) has been developed to calibrate without requiring a physical camera model, by applying polynomial and affine projection models. This approach is capable of calibrating various types of lenses such as wide-angle lenses and perspective lenses with an accuracy around one pixel.

Vallet, Panissod, Strecha, and Tracol (2011) conducted an investigation analysing the performance of an ultra-light weight UAV “Swinglet” attached with a Canon Ixus 120IS to produce DTM/DSM and Orthomosaic. The images were processed using two different workflows; the first one using traditional photogrammetry tools, and the other using a dense image matching process. The resulting data was compared with reference data from ALS using the Helimap System. The results show that the quality of the derived Digital Elevation Model accuracy tends to depend on the processing tools used, and it was limited by the weakness of the lens distortion modelling.

2.3.2. Motion blur

A captured image does not represent a single instant of time. The image represents an accumulation of light received by the camera sensor in a certain period. Most often, the exposure time is fast enough to capture a picture that appears as an instantaneous moment. However, this is not always the case, especially when the sensor is capturing a fast moving object, or when the sensor is attached to a fast moving platform such as an airplane or UAV; it may result in a motion-blurred image as shown in the figure below.



Figure 3. Sharp image (left) and motion-blurred image (right)

Sieberth, Wackrow, and Chandler (2014) conducted research on the impact of motion-blurred images on automatic image processing. A shaker table was used to produce a known amplitude and frequency. A Nikon D80 was mounted on the table, and the camera exposure was synchronised with the table’s movement to generate images with accurately known motion blur. The outcomes indicate that the level of motion blur is inversely proportional to the accuracy of measurement. Small quantities of blur did not significantly affect the accuracy as long as the target is detected and successfully measured. The detection algorithm will easily find edges that are parallel to the blur direction. However, the algorithm hardly finds the edge perpendicular to the blur direction due to a transitional effect that makes the detection of the edge difficult and subsequently provides an imprecise estimation. Fully automatic edge detection of the target only works well in the images containing small blurs. However, manual operator inputs had been carried out and produced an acceptable accuracy on highly blurred images. As a consideration, the experiment was conducted by using only signalled targets. Thus, using natural features as a target in a highly blurred image would probably detect fewer features or even become impractical.

As well as linear motion blur, angular motion blur has also affected image quality in the photogrammetry field. Although, the three rotation angles (roll, pitch, and yaw) have been well corrected by gyro-stabilised

mounts controlled by integrated GPS/IMU systems, leaving linear motion blur uncorrected (Pacey & Fricker, 2005).

The linear motion blur can be quantified by calculating the displacement vector of the shifted object within a certain period of time. The motion blur in the photogrammetry field needs to be solved because it affects the automatic image processing result (Sieberth et al., 2014). To address the linear motion blur issue, several methods can be applied to limit the effect of motion in digital imaging, such as mechanically moving the focal plane, using shorter time exposure that equal or less than the pixel size, and assigning time delay and integration (TDI). All methods require exact flight speed, flight altitude and camera shutter speed information (Pacey & Fricker, 2005).

2.3.3. Acquisition mode

Eisenbeiss and Sauerbier (2011) have investigated the flight modes of UAV for photogrammetric applications. They compared the impact of the flight trajectory with the accuracy of derived photogrammetric products. There were three distinct flight modes being used: manual flight mode, semi-automated flight mode, and fully autonomous flight mode. In manual flight mode, the UAV movement is fully controlled by a human pilot. In semi-automated flight mode, the UAV is stabilised by the system while the operator only needs to take care of the position of the UAV based on the GNSS. While in fully autonomous flight mode, the pilot hands over all control of the UAV for it to be entirely automatically processed by the on-board unit. The latter mentioned mode is the most practically useful mode for UAV-based photogrammetric flights since it allows the onboard unit to accurately navigate the UAV. There were also three image acquisition modes defined: manual image acquisition mode, stop mode for image acquisition, and cruising mode. These modes were applied in five different case study fields with different types of UAVs and cameras. The results show that manually controlled mode is not as stable as semi-automated or autonomously controlled modes, with a non-negligible influence on the accuracy of the final derived products. The results also reveal that stop mode image acquisition produced instability in maintaining flight direction and defined image overlap.

Bailey (2012) has studied an algorithm optimising the flight path on lightweight fixed-wing UAV data acquisition. The algorithm was performed under three optimisation modes: area geometry only, wind direction only, and an average of both. The simulations were carried out on a region of rectangular shape using a built-in simulator in the Paparazzi's Microjet software. The results of the simulations show that optimisation based on the area geometry tended to produce persistent optimal flight paths, as opposed to following the wind direction. The combination of the suggested vectors from both geometry and wind demonstrates no additional value in most cases. Bailey also suggested expanding the acquisition area to all sides, in such a way that the UAV assembles on the desired path before it enters the actual study area, ensuring the necessary images overlap. The simulation results show the UAV to be habitually off-path when it turns around at the border of the region, potentially ruining the overlap.

2.3.4. Flight altitude

Flight altitude has become an integral part of photogrammetry. Primarily in close-range photogrammetry utilising UAV, flight altitude turns into a more sensitive issue. Despite its impact on the expected GSD size, lower flight altitude demands a longer acquisition time to complete the entire area. As the most significant limitation for a UAV is its battery life, in most scenarios, a larger area of interest will probably end in multiple flight acquisition. If the image acquisition takes too long, another problem related to the presence of shadow arises. The shadow changes its shape due to the movement of the sun, and negatively influences the results (Rock, Ries, & Udelhoven, 2011).

Concerning the flight altitude impact on the resulting accuracy, Tahar (2015) examined the influence of UAV flight altitude on the resulting accuracy in various slope attributes; from a gentle slope to very steep slope. A consumer-grade camera Sony NEX-5n attached to a multirotor UAV was used to capture images

at five different altitudes, from 40 m to 80 m with an increase of 10 m. The camera calibration process has been carried out separately prior to data acquisition process. By comparing the resulting RMSE from each flight height, the study found that the accuracy of the slope increased when the altitude was increased, which mainly affected the Z accuracy. Moreover, different conditions of slopes also had an impact on the resulting accuracy. The study also revealed that the variation in the resulting slope aspect from different flight altitudes was higher in 'gentle slope' class. Moreover, compared with the results from total station measurements, 'gentle' and 'moderate' slope classes had small differences in the results compared to 'steep' class.

Udin and Ahmad (2014) also undertook research regarding the impact of flying altitude variation of a UAV on its mapping accuracy. The study utilised a rotary blade UAV for stream mapping at different flight altitudes with 60% forward overlap and 30% lateral overlap. The variation in flight altitude was 40 m, 60 m, 80 m, and 100m. In contrast with Tahar's findings, their study concluded that the RMSE of vertical accuracy tends to decrease as the flying height increases although the difference is relatively small, only around four centimetres in every 20 metres flight altitude addition.

2.3.5. RTK GNSS-based Direct Georeferencing

Direct georeferencing is a newly method, which was developed in the digital photogrammetry era. Theoretically, this method will eliminate the need for control points in the aerial photogrammetry workflow. The method will bring huge advantages especially in terms of production budget savings, faster overall time processing, and simpler workflow (Rizaldy & Firdaus, 2012). Direct georeferencing uses two pieces of equipment to directly calculate onboard six parameters in exterior orientation: a GPS/GNSS unit to measure the image position (x, y, z) and IMU to compute image rotation (ω, ϕ, κ) .

Rather than using a code-phase measurement in the GNSS unit, direct georeferencing by using the phase of the signal carrier wave and two incorporated stations (base and rover) provides an enhancement of the position calculation up to a centimetre-level of accuracy (Figure 4). The base station broadcasts its well-known position, along with the code and carrier measurements at the L1 and L2 frequencies for all captured satellites. Based on this information, the rover can correct the phase ambiguity and determine their relative position to the base station in a high precision (Navipedia, 2014b).

The RTK method is very convenient for low-altitude UAVs. Since most ultralight UAVs should fly below 150 metres by law, this distance range would be an advantage for RTK to work properly; as the greater the distance between the base station and the rover will also raise the ambiguity. However, some issues remain such as the need to track the rover continuously, making the RTK not so suitable for urban applications especially if the local base station must be placed in the urban area (Navipedia, 2014b).

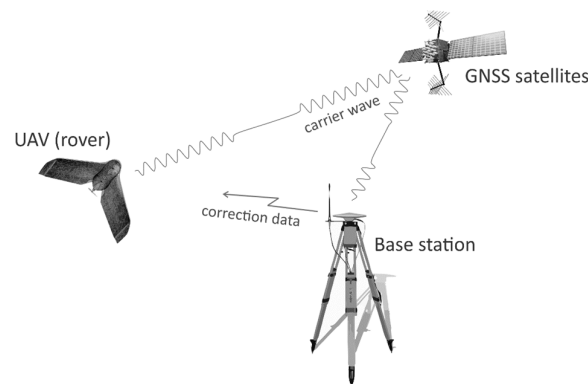


Figure 4. RTK GNSS-based direct georeferencing

However, due to limited carriage capabilities of the ultralight UAV, the development of precise direct georeferencing for the UAV platform is very challenging. Although nowadays an RTK system with a weight

below 300 grams is already available (NovAtel, 2016), this system is nevertheless heavier than a code-phase GNSS due to the need to add more parts in order that the system can work. Regardless, recent developments show that ultralight UAVs with RTK systems are already available on the market (MAVinci, 2015; Sensefly, 2015).

Eling, Klingbeil, and Kuhlmann (2015) conducted research regarding the reliability of RTK-based direct georeferencing systems in a rotary blade UAV. The UAV was used to map buildings by employing a 5MP camera and agricultural mapping by employing a low-cost portable laser scanner. They conclude that the system was capable of providing high accuracy positions below 5 cm of Sigma and possible to integrate with different sensors.

2.3.6. Image overlap

In a celluloid-based photogrammetric era, the number of overlapping images used to be a predominant factor in defining a project. A higher image overlap could force a higher budget to be expended. The more image overlap being employed in a project, the higher cost to provide the celluloid film, film development, and printing or scanning. A convention of roughly 60% forward overlap and 30% lateral overlap had been used for a long time in aerial photogrammetry in order to provide a stereo image compilation to generate a 3D product such as DSM (Burns, 2011; Kraus, 1993; Lembicz, 2006) before a paradigm shift occurred with the digital photogrammetry era.

One of the main benefits of the digital photogrammetry era is an ability to greatly increase the forward overlaps without any added production cost. However, a higher number of forward overlaps will lead to another additional issue; it creates more images for the same sized area (Figure 5). In a large-scale close-range photogrammetric project, 10% overlap increments can lead to an increase of thousands of images. Ultimately, this huge number of images will lead to other extra costs: processing time and processing tools.



Figure 5. Sample of flight line with 60%, 75%, and 90% forward overlap

Despite that, the higher overlap offers numerous opportunities including providing a higher level of tie points. The use of high forward overlaps, even up to 90% forward overlap, will provide a better opportunity for aerial triangulation to reduce mismatches due to more observations available. By increasing the image overlap, the benefit is manifold; a single position on the ground will be mapped in more images than with a lower overlap, helping to reduce 3D positional ambiguity and eventually providing a more robust bundle block (Gruber, Perko, & Ponticelli, 2004).

2.3.7. Flight pattern

Additional flying cross strips were initially used to reduce the number of GCPs in a bundle block, by adding two cross strips on each edge of the photogrammetric block. This addition not only reduces the number of GCPs but also strengthens the mathematical model within the BBA computations (Abdullah, 2014; Lembicz, 2006). Even though, cross flight additions could not actually replace the presence of control points (Lembicz, 2006). The reduction of more than 30% of control points could cause an intolerable deformation of the bundle block.

The use of cross-strip additions actually leads into new problems in a matching process. Although the cross-strip direction is positional adjacent to the main strip, a time delay in acquisition between those strips causes illumination differences and moving shadow phenomenon occurs (Ok et al., 2011). As a result, the output from image matching process is negatively affected (Haala, 2009).

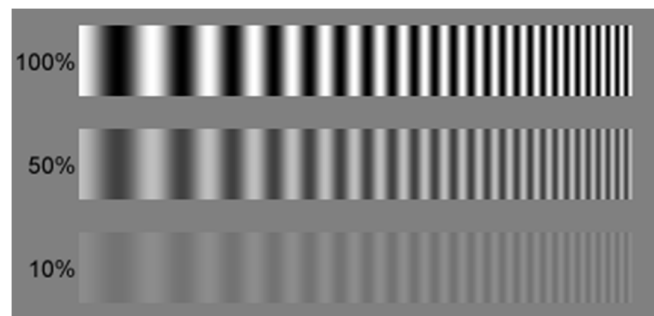
2.3.8. Distribution of GCPs

Nocerino, Menna, Remondino, and Lunazzi (2013) have discussed the accuracy and deformation analysis on the integration of UAV and terrestrial photogrammetric surveys. They took a survey area in an archaeological site of the Roman Theatre in Ventimiglia, Italy. The UAV was engaged in acquiring both vertical and oblique images while the terrestrial image acquisition was performed to generate separate point clouds of some vertical structures. With a combination of vertical and oblique images added with 5-GCPs, a vertical error of 3 mm was achieved with a horizontal error of 5 mm. Signalised points were used as GCPs and checkpoints, placed on both vertical and horizontal sides of targets. The report informed that the accuracy of the products required careful acquisition planning and processing steps. Evenly distributed ground control points guaranteed the reliability of the point cloud. With more than a thousand images collected, highly automated SfM procedures demonstrated great potential concerning spatial resolution and processing time.

2.4. Modulation Transfer Function

Back when film cameras were widely used, the resolving power used to be measured in line pairs per millimetre (lp/mm). The value is obtained by photographing a chart such as the USAF 1951 lens test chart and looking at the highest resolution pattern where the detail is still visible. However, this test is easy to perform but poorly standardised due to the human perception involved (Koren, 2013a). Two measurements of exactly the same camera and film systems will have different results when performed by two different observers. This measurement also needs a well-established contrast level to be comparable, which typically requires expensive lighting instrumentation.

A precise measurement called Modulation Transfer Function (MTF) was invented to solve the problem of perceived contrast by utilising frequency domain. This calculation measures the transfer of modulation or contrast of the object to the image (Atkins, 2007). A bar pattern consisting of black and white lines (1 line pair) with increasing spatial frequency will give a response of sinusoidal wave (Figure 6). In the beginning, the lines will easily be separated from each other with a full contrast. As the spatial frequency increases, the lines will appear to start merging and reaching zero contrast. Thus, the contrast of the spatial frequency is a dependent variable of the measurement (Koren, 2013a; Kurtsev, 2008). In a full 100% contrast, the pattern is un-attenuated. Meanwhile, at the frequency of MTF 50% the contrast is moderately attenuated, and severely attenuated at MTF 10%. However, perceived image sharpness is closely associated with MTF 50%, when the contrast has dropped by half (Koren, 2013a).



(Koren, 2013a)

Figure 6. MTF patterns at several attenuation

According to Koren (2015a), the MTF was calculated based on the following equation:

$$MTF(f) = 100\% \times \frac{C(f)}{C(0)} \quad (1)$$

where:

$$C(f) = \frac{V_W - V_B}{V_W + V_B} \quad \rightarrow \text{The low frequency (black-white) contrast}$$

$$C(0) = \frac{V_{max} - V_{min}}{V_{max} + V_{min}} \quad \rightarrow \text{The contrast at spatial frequency}$$

V_B = Minimum luminance/pixel value for black area at low spatial frequency

V_W = Maximum luminance for white area at low spatial frequency

V_{min} = Minimum luminance for a pattern near spatial frequency f

V_{max} = Maximum luminance for a pattern near spatial frequency f

The MTF is suitable for digital cameras, where the sensor sizes are widely varied. However, MTF is different with the film's grain. While the grain increases proportionally with the ISO speed, MTF is less responsive to the ISO speed (Koren, 2013a). However, MTF will tend to have poorer results if a large lens aperture is used, when the Rayleigh diffraction as an unavoidable consequence of lens physics starts to dominate. At large apertures, the image resolutions are constrained by aberrations, which eventually lowers the actual resolve power (Koren, 2013c).

2.5. Structure from Motion

Image matching is an establishment of correspondence from a point recorded in two or more images and estimates its corresponding 3D position using collinearity or projection model. This method typically has two steps: (1) in image space, depth maps are produced from the stereo or multi-view stereo pair calculation by considering the disparity between image pair, (2) then these depth maps will be merged to create a 3D point cloud in object space (Li, Li, Chen, Xu, & Zhang, 2010; Remondino et al., 2013).

Image matching is mostly done only in salient points, resulting a sparse point cloud from image pairs. However, this sparse point cloud is insufficient for many applications, especially in an application that requires a high level of detail. By only relying on a sparse point cloud, many details are lost, which ultimately affect the final result.

Multi-view Stereo Vision (MVS) is capable of producing a dense and accurate representation of a complex surface object from a number of calibrated images recording the same object or scene, even just using low-resolution images (Furukawa & Ponce, 2009; Seitz, Curless, Diebel, Scharstein, & Szeliski, 2006). Combined with high-resolution cameras, this technology offers exceptional geometric accuracy for image-based modelling works.

In a traditional photogrammetry workflow employing a metric large frame camera, a camera calibration process means determining the internal camera parameters. The calibration process is supposed to be done in a laboratory and the camera parameters are assumed to be stable within a certain period. A well-planned and executed airborne image acquisition supported by better GPS/IMU observations makes the image output ready to be further processed in BBA, either by direct georeferencing when it is possible, or, at least, it gives a better positional approximation to ensure the tiepoint matching process is a bit "easier" (Gerke, 2015).

In a computer vision, a calibration process means a whole process from a determination of the internal parameters of the camera to an estimation of the pose and scene of the camera in the real world at the moment of image acquisition. The use of uncalibrated cameras demands a robust estimation of a fundamental matrix using corresponding points and RANSAC to model relative orientation of both cameras. By using this estimation as starting image pairs, the model will add the next consecutive image that

shares common observation points throughout resection. Eventually, this process will construct a block of images that are relatively interconnected before a bundle adjustment is done to the entire block. This entire workflow is termed Structure from Motion (SfM).

However, the problem arises when the calibrated images input cannot exactly represent the true scene as the same ideal camera (pinhole) viewpoints. An input of images with an error in camera's internal geometry will tend to generate a deformed image matching result. Despite this deformation can be suppressed by an addition of sufficient control points (Nocerino et al., 2013). The problem with finding correspondence between images is detecting reliably good computed features to be applied as matching points. Many methods in edge feature detection have been published (Bay, Ess, Tuytelaars, & Van Gool, 2008; Lowe, 2004; Shin, Goldgof, Bowyer, & Nikiforou, 2001). Each method has its advantages as well as disadvantages in handling specific conditions of the image such as blurred images, the degree of image rotation, viewpoint, and illumination change. These conditions will ultimately give a different result in the accuracy of the derived product.

3. METHODOLOGY

3.1. Overview

In this chapter, a general overview of the methods used in this research to achieve the objectives is explained. The general methodology of this research is divided into four processes as shown in Figure 7. The first section is research preparation, followed by data acquisition, data preparation, and the last section is data processing and analysis. Each section on this workflow will be described in detail in the following subchapters.

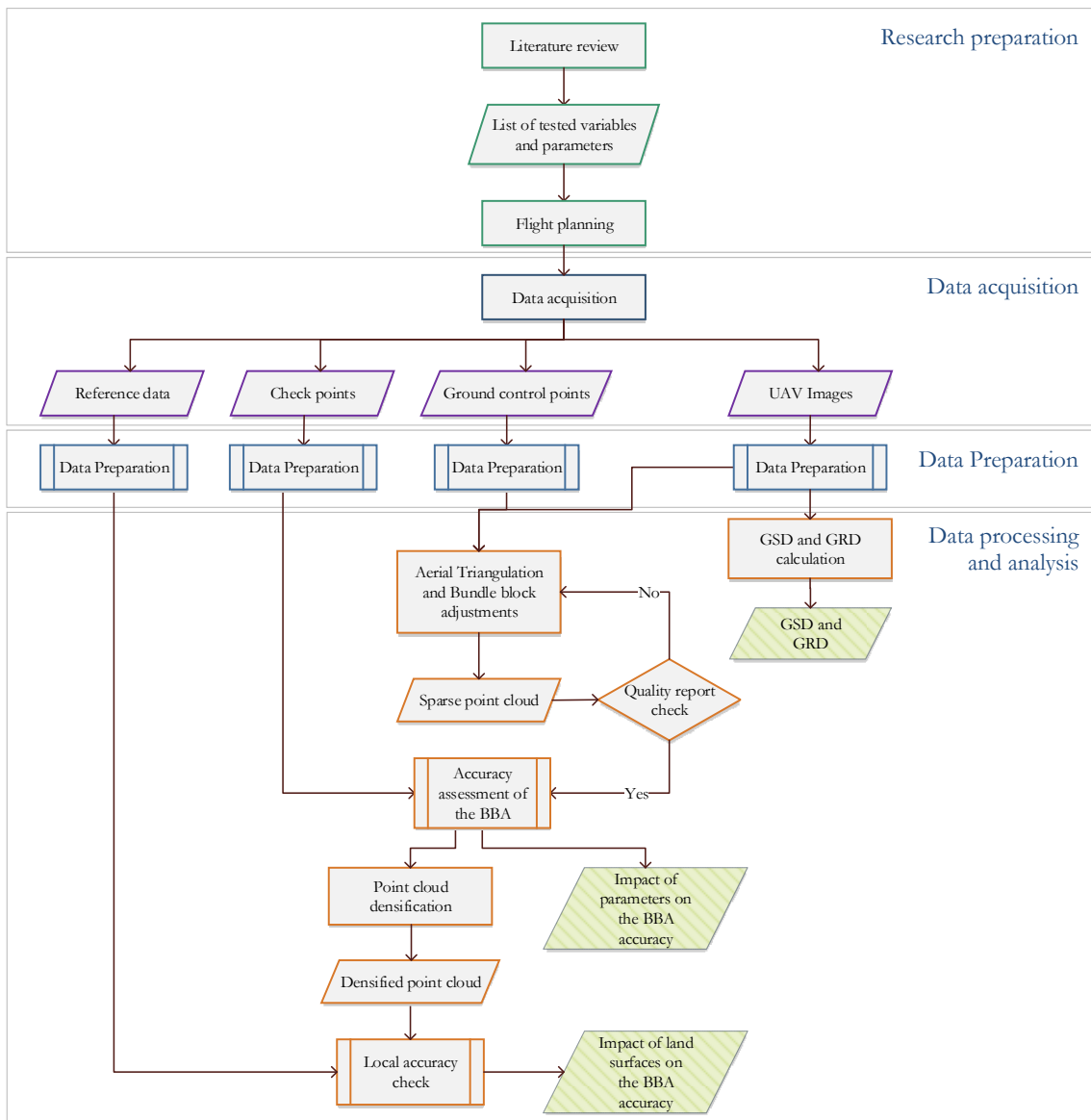


Figure 7. Flow diagram of the research

3.2. Research preparation

Based on the literature review, several assumptions are made including the fact that most of the research conducted only takes into account one parameter as a point of interest in their study, and neglects other parameters that might have an unseparated influence on the tested parameter. For this reason, a study that takes into account the main parameters that influence the accuracy of the derived product of the UAV-based photogrammetry should be conducted. A list of parameters and variables that need to be tested in this research can be summed up as follows.

Table 1. The tested parameters

<i>Optical Sensor</i>	<i>Motion Blur</i>	<i>Flight Overlap</i>	<i>Flight Config.</i>	<i>Flight Altitude</i>	<i>Acquisition Mode</i>	<i>Number and Distribution of GCPs</i>	<i>Image Initial Position</i>
• DJI Phantom 2 with a built-in camera	• Blurred	• 90/50	• Single strip	• 50 m	• Stop mode	• 0 GCP	• RTK-GNSS
	• Sharp	• 80/50	• Cross strips	• 60 m	• Cruising mode	• 4 GCPs	• Code-phase GNSS
• Aibotix X6 with Canon 600D & 20 mm lens		• 70/50	• Oblique	• 70 m		• 5 GCPs	
• Ebee RTK				• 80 m		• 10 GCPs	
						• Distributed	
						• Undistributed	

To objectify every parameter and variable that need to be measured in this research, careful flight planning as a part of the research preparation needs to be conducted. However, it is impossible to test all combinations of parameters and variables one by one, since several variables such as stop mode and RTK GNSS-based georeferencing could not be obtained from all UAVs employed. A detailed flight planning will be described in next chapters.

Several parameters and variables such as acquisition mode and flight altitude could be determined directly in a flight mission planning software. Some other parameters such as expected motion blur needs to be calculated in advance, before establishing the best configurations for UAVs to acquire the images. Due to limitations in the software to process the number of waypoints as the position of the UAV to acquire image, the 90% forward overlap in Aibot X6 cannot be determined via flight mission software, but by automatically triggering the camera to take picture in every one second. However, this method will not give an exact 90% forward overlap on all Aibot X6 flight configurations. Calculation of the expected forward overlaps was performed at this stage, prior to data acquisition. Calculation of theoretical vertical accuracy was also done at this step to estimate the achievable vertical accuracy of each flight configuration.

3.2.1. Overlapped area estimation

The expected overlapped area of two consecutive images is highly correlated with the extent of the image footprint and the distance difference between two consecutive images (Δd). Determining the image footprint involves specifying the desired GSD and the image resolution in pixels. The image footprint is an area of single image resolution ($R_H \times R_W$) multiplied by its GSD size. After determining the image footprint, the other variables to calculate were the expected forward overlap (FO) and lateral overlap (LO) percentage. The forward overlap percentage is calculated as:

$$FO = \frac{(R_H \times GSD) - \Delta d}{R_H \times GSD} \times 100\% \quad (2)$$

The lateral overlap basically has the same equation as the forward overlap, except replacing the image resolution's height (R_H) with the image resolution's width (R_W). The image resolution in width was chosen

to calculate the forward overlap because the camera was attached to the UAV with the flight direction towards the width side of the image.

3.2.2. Expected motion blur

The degree of blurring of the image is estimated using the theoretical image motion formula (Kraus, 2007), where u_{th} is theoretical image motion, c is focal length, v is ground speed of aircraft, H is the flight height of the plane, and t is exposure time (Figure 8). During the time of exposure t , the object or camera moves with the ground speed v , a point object O in the real world will be shifted as far as $v \cdot t$. This shifting will be recorded on the image as a “line” called image motion. The degree of image motion on the image is calculated as follows:

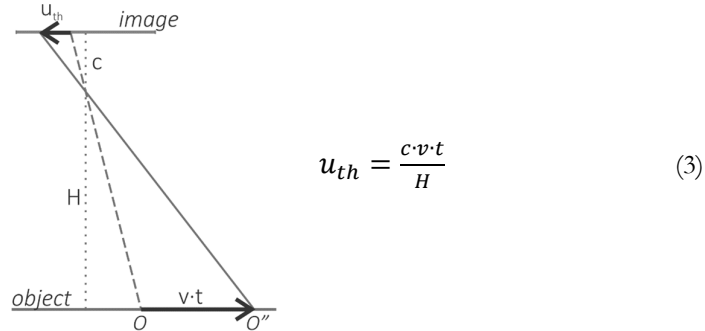


Figure 8. Theoretical image motion

Undoubtedly, the actual blur recorded on the image is higher than the theoretical value. The calculation is solely to approximate the effect of the motion blur received by an image, by neglecting other factors that magnify the blur effect such as lens displacements and vibrations from the moving parts of the platform. These total blur impacts would be measured later by utilising the Norman Koren Test Chart (Koren, 2013b) to determine the GRD as an actual number of the image ability to resolve the two smallest separated objects. Detailed information regarding GRD will be explained in a later section.

3.2.3. Theoretical vertical accuracy

Vertical accuracy of stereo-pair images was computed based on the simplified relationship between stereo cameras and the corresponding object in an aerial triangulation scheme. Vertical accuracy indicates the expected error from a derived 3D product that should be anticipated. Although in most cases the actual achievable accuracy of a product is higher than the theoretical vertical accuracy due to some refinements, this simplified theoretical accuracy is typically used to predict whether a configuration set-up can possibly meet the requirements of the expected product or not.

According to Kraus (2007), the aerial triangulation relationship between the flight height (H) and the focal length (c) are equal to the baseline (b) within two cameras (O_1 and O_2) and the parallax (p_x) of the corresponding object within two images as shown in Figure 9.

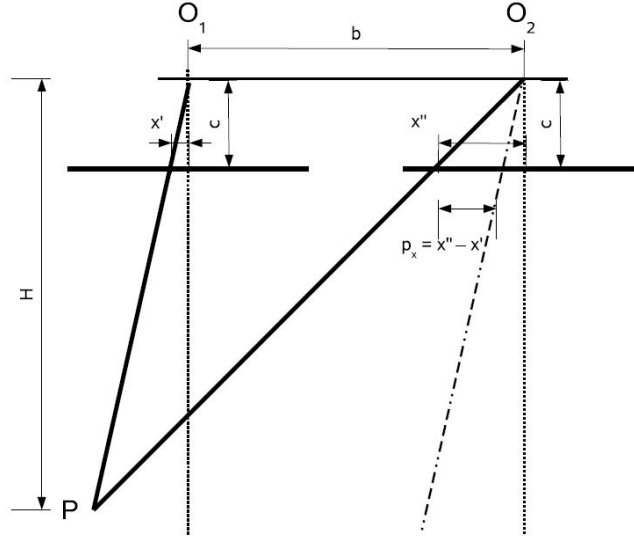


Figure 9. Aerial triangulation relationships

The relationship between flight height (H), focal length (c), baseline (b), and parallax (p_x) is:

$$\frac{H}{c} = \frac{b}{p_x} \rightarrow H = \frac{b \cdot c}{p_x} \quad (4)$$

The image scale in photogrammetry (m) is interpreted as a ratio between flight height and focal length (c), while its scale number can be determined as follows:

$$m = \frac{H}{c} \quad (5)$$

According to Kraus (2007), the rule of thumb to calculate theoretical error in height (σ_H) of a stereo pair is:

$$\sigma_H = \frac{H}{b} \cdot m \cdot \sigma_{px} \quad (6)$$

or

$$\sigma_H = \frac{H^2}{b \cdot c} \cdot \sigma_{px}$$

where σ_{px} is the Sigma of parallax, as an accumulation of error from σ_x and $\sigma_{x''}$.

However, in a case involving multiple overlapping images, this rule of thumb will give a coarse estimation of error. Förstner (1998) presented a refinement of the theoretical accuracy calculation for multiple images. In the case of a point observed from K number of images/cameras that have the same focal length c and baseline b along the track in x direction, the theoretical vertical accuracy (σ_H) is calculated based on the equation:

$$\sigma_H = \frac{H^2}{b \cdot c} \cdot \frac{\sigma_x \cdot \sqrt{12}}{\sqrt{K(K-1)}} \quad (7)$$

3.2.4. Empirical Error Measurements of the Residual in Checkpoints

According to the Federal Geographic Data Committee (1998), the accepted measure of positional accuracy is the mean square root of squared differences between the reference points and the measured points. In statistics, this term is called root-mean-square deviation (RMSD) or root-mean-square error (RMSE). Although the RMSE is widely used to measure the accuracy, some other measurements can also be used

such as mean error, percentile, and standard deviation (Congalton & Green, 2008; Navipedia, 2014a). The RMSE for a given direction in X, Y, or Z is defined as follows.

$$RMSE = \sqrt{\frac{\sum e_i^2}{N}} \quad (8)$$

where:

e = the error of each point
N = the number of GCPs

Besides RMSE, the standard deviation/sigma (σ) has also been used in this research to measure the precision of the resulting block adjustment process. In statistics, the value of one standard deviation of the mean in a normal distribution is 68.27% of the data. The Sigma indicates the expected error of the point by excluding the systematic error. The systematic errors can be recognised by employing the mean value of the error when the mean error value is not almost equal to zero.

$$\sigma = \sqrt{\frac{\sum (e_i - \mu)^2}{N}} \quad (9)$$

where:

e = the error of each point
 μ = the mean value of errors
N = the number of GCPs

The standard deviation has been chosen because this value was used in the calculation of the theoretical vertical accuracy. To ensure a comparability between the theoretical accuracy and its actual accuracy, the standard deviation was used to quantify the accuracy. Furthermore, comparing with the RMSE value, Sigma can be used to justify the degree of residual variation in checkpoints without taking into account the average systematic error that still exists on the respective bundle block.

However, to give a clear comparison of error with respect to its flight altitudes or sensor variances, the amount of error should be normalised somehow. Without normalisation, the error from larger GSD will tend to be larger. Yet, a positional error involving the limitation of GSD area size cannot be avoided when performing GCP/checkpoint marking. For this reason, the Sigma value will be divided by its GSD size in a comparison involving different flight altitudes or types of sensors. The GSD size used here is the average GSD output size computed in one bundle block, obtained from the AAT quality report output.

3.3. Data acquisition

Precise positioning is an essential requirement in this study. The expected achievable accuracy of the 3D reference points must be higher than the GSD of the UAV images; which is 1 cm for the lowest flight altitude. A Real Time Kinematic (RTK) method was selected as an enhanced method to collect the 3D reference points. RTK is a differential GPS (DGPS) technique that delivers a high positional accuracy in the surrounding of base stations. The technique is based on the use of the carrier phase of GPS signals and the communication link of the correction from the base station, which has a well-known location (Figure 10). By comparing the position generated from simultaneous data retrieval and assuming that most of the errors that occur in the absolute position of the base station and rover will be the same, the base station transmitted the positional correction data to the mobile rover, cancelled out most errors that usually happen in a stand-alone positioning measurement. However, some uncorrelated errors such as multipath cannot be corrected by this method.

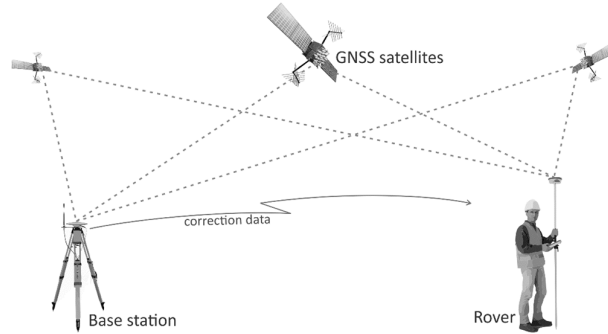


Figure 10. Real-Time Kinematic (RTK) methods

The Leica Viva GS14 GNSS System was used as a rover in the 3D reference point's data collection, by employing the RDNAPTrans2008 as the coordinate system and Bessel as an ellipsoid. According to Kadaster (2015), the RDNAPTrans2008 is the latest official transformation of the Dutch national triangulation system (Rijksdriehoekstelsel/RD). This method gives an accurate transformation from RD and Amsterdam mean sea level (NAP) to other systems. The base station used in the 3D reference point's measurement was a base station located on the top of the ITC building.

The RTK method was also used in Ebee RTK data acquisition. With the Ebee RTK, the UAV acts as a rover and receives broadcasts from a base station. Instead of using correction broadcasts from a base station in the ITC building, the Ebee RTK used a local base station with a known position in the field as a correction broadcaster.

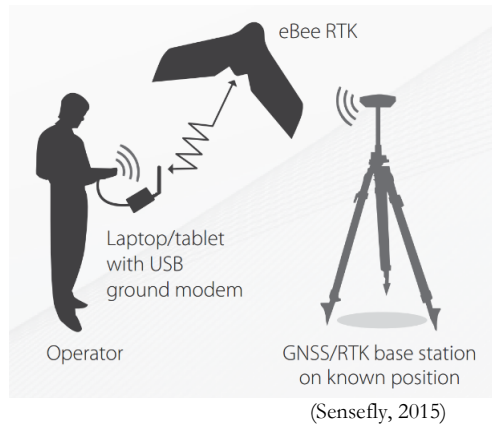


Figure 11. Ebee RTK configurations

The UAVs flew based on the flight configurations that were already planned during the research preparation phase. Three different UAVs were used to collect all the image data. Due to a high camera shutter speed being used in most of the configurations; adequacy of sunlight is one of the main factors in dictating the time for image data acquisition. Although there is no dedicated calculation to measure the required amount of sunlight to meet the needs of the flight configurations, a day with sunny weather typically can provide sufficient sunlight to do image acquisition with a high shutter speed.

Each UAV is unique. In the rotary blade UAVs, battery limitation contributes to determining the area to be covered in a single flight. Contrary to the manufacturer's claim that the flight duration of the Aibot X6 and the DJI Phantom 2 Vision+ could be up to half an hour, the actual flight durations were never more than 15 minutes. Due to this limitation, each flight configuration was split into two flights, and each flight contained 4-5 times back-and-forth/strip flights (Figure 12). However, the battery limitation has never been

an issue with the Ebee RTK. Despite having a longer battery life, a fixed-wing UAV requires a shorter time to cover the entire area due to the need to fly at a higher speed than a rotary blade UAV, making it capable of covering a larger area in a single flight.

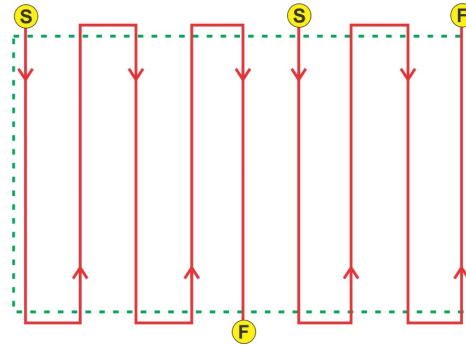


Figure 12. Two back-and-forth flights in one flight configuration

3.4. Data preparation

Before all the collected data can be further processed, it is necessary to organise a data preparation after the fieldwork. It is necessary to check all the collected data for consistency with what was planned. The data preparation workflows of the UAV images and the 3D points are shown in the figure below.

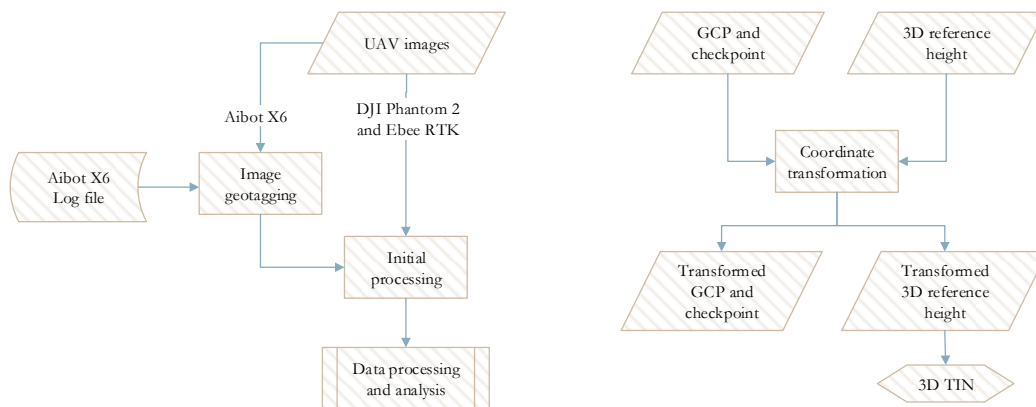


Figure 13. Data preparation workflow

Unlike with the DJI Phantom 2 and the Ebee RTK, the image acquired by the Aibot X6 had not been automatically georeferenced, before it was imported to flight mission software and geotagged based on the Aibot's flight log file. After ensuring all images have been georeferenced, the images needed to be checked for coverage completeness by performing initial processing of the aerial triangulation.

However, the 3D points collected from GNSS surveys had different pre-processing steps. Since the survey output coordinate was in Dutch national coordinate system (RD) and the expected coordinate output was in Universal Transverse Mercator (UTM), a coordinate transformation had to be conducted. The transformation was done in ArcGIS for Desktop Version 10.3.1 (Esri, 2015) using ArcToolbox "Project". The output coordinate system was "WGS 1984 UTM Zone 32N" and the geographic transformation method was "Amersfoort_to_WGS_1984_2008_MB" as a form of RDNAPTrans2008 in ArcMap 10.3.1.

To check the consistency of the resulting 3D reference height in representing the surface heights, a Triangulated Irregular Network (TIN) of the 3D points was created. The advantage of the TIN over the

rasterised DEM is that the distribution of its triangles varies according to the position and density of 3D points. Although the resulting TIN was not to be used further, this process is crucial to determine whether the collected 3D points were sufficient to represent the selected land surface's terrain or additional fieldwork needed to be done.

3.5. Data processing and analysis

The data processing and analysis were done after all the data had been prepared. GSD and GRD calculations are actually independent to the preparation step, in the sense that no data preparation process is required to be done before the calculation. While, the GRD calculation can be directly conducted after the image is collected. Meanwhile, to analyse the impact of parameters on the block adjustment accuracy, the GCPs and checkpoints need to be marked on the images. The workflow of the data processing and analysis can be examined in Figure 14.

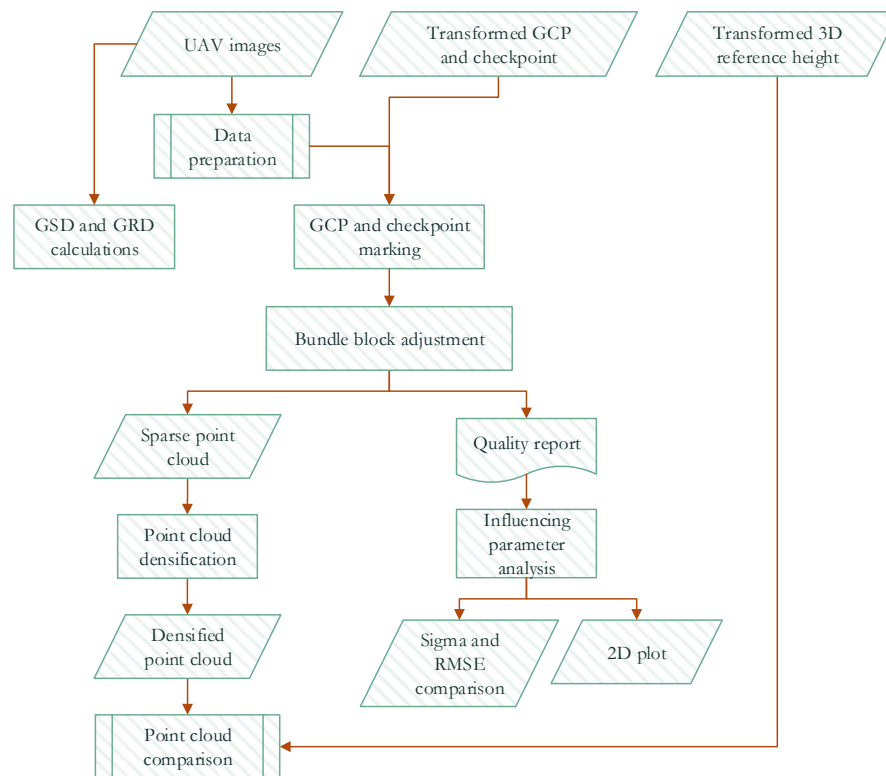


Figure 14. Data processing and analysis workflow

3.5.1. Ground Sampling Distance and Ground Resolved Distance calculations

The GSD and GRD comparisons were conducted to see the correlation between the two in response to the change in the parameters or flight setups. Although there are various definitions of the sampling distance, the GSD is defined as the degree of detail, the finest level of measurement, or the sampling unit (Warner, Nellis, & Foody, 2009). GSD is calculated from the distance between the midpoint of two adjacent pixels on the ground; or simply can be interpreted as the size of 1 pixel multiplied by the scale (m). Meanwhile, image scale is defined as a proportional distance between a linear distance on a vertical photograph and the corresponding distance on the ground (Avery & Berlin, 1992). The GSD is important because it is highly correlated with the expected level of detail, despite the fact that the actual recorded distance on the image

could be different due to the influence of the optical system and environmental conditions. The GSD is calculated as follows:

$$GSD = \text{pixel size} \times m \quad (10)$$

Ground Resolved Distance (GRD) in remote sensing fields is defined as the dimensions of the smallest object that can be detected on the image (Campbell, 2002). Seemingly, both GSD and GRD have the same meaning, which is identifying the smallest distance/dimension of an object that can be detected on the image. However, these two definitions have different calculation methods. The GRD is calculated based on the numbers of the smallest cycles (line pairs) per pixel (c/p) that can be resolved in an image, by using Modulation Transfer Function (Campbell, 2002; Imatest, 2015b). In this research, the unit selected in the MTF calculation was line widths per picture height (LW/PH) due to the need to compare the result of a specific setup with its GSD, as the picture height unit is also in pixel size. The MTF calculation was done in Imatest Master Version 4.2.9 (Imatest, 2015a).

MTF 50% (MTF50) and its peak value (MTF50P) were chosen to justify the sharpness of the resulting UAV images. According to Imatest (2015), there are two reasons that the MTF50 and MTF50P are good justification parameters for comparing the sharpness from different cameras and lenses: (1) the image contrast is half of its low frequency, hence the detail is still fully visible. (2) The frequency response of most cameras rapidly drops off at around MTF50 and MTF50P. However, there is a difference between MTF50 and MTF50P in their calculation method. MTF50 is the spatial frequency in which the contrast drops to half of its low frequency value. Usually used to illustrate the perceived sharpness in a normal image. Meanwhile, the spatial frequency in MTF50P is calculated when the contrast drops to half of its peak frequency value. The value of MTF50P will be the same as MTF50 in an original unsharpened image, but smaller in an over-sharpened image. According to Imatest (2016), MTF50P value is important due to it is less exaggerated by an extreme image sharpening that has “halos” near edges as happened in the image collected from DJI Phantom 2. However, the image sharpening process with the DJI Phantom 2 is an inevitable process because it was done automatically in the camera. Figure 15 shows the differences between a normal image captured from the Aibot X6 and a strongly sharpened image captured from the DJI Phantom 2.



Figure 15. Normal images from Aibot X6 (left) and strongly sharpened image from DJI Phantom 2 (right)

During UAV image data acquisition, an A0-size Koren Chart and Siemens Star were placed in the middle of the study area, in the area that is projected to be passed over by the UAV. The Koren chart is the main chart used in MTF calculation while the other is a subsidiary in case the Koren chart failed to deliver results.

3.5.2. Automatic aerial triangulation and bundle block adjustment

The AAT and BBA were done using Pix4Dmapper Pro Version 2.1.100 (Pix4D, 2015b). The full feature keypoints scale with original image size was chosen to give an accurate result of tie points. The calibration process was set to standard (all) option, to ensure the camera external and internal parameters are also optimised during the AAT and BBA processes. The output of these processes was a Quality Report, which includes information about the number of overlapping images, the number of keypoints generated, and positional residuals.

3.5.3. Influencing parameters analysis

To describe the impact of each parameter in contributing to the deformation of the bundle block, a residuals analysis was carried out to estimate the differences in the value of the reference point from its representation in the bundle block. The residual analysis was done by analysing the statistical value of errors on checkpoints obtained from the BBA's quality report. The analysis was conducted in two ways: (1) comparing the Sigma and RMSE results from checkpoints of each BBA process and (2) presenting the XYZ position error on each checkpoint on a 2D plot to see the residual directions in the form of deformation patterns. The amount of horizontal and vertical error of each checkpoint is visualised in a 2D plot using open source software Gnuplot Version 5.0.1, with the direction of horizontal (XY) error is drawn in a vector and the direction of vertical error is drawn in another vector.

3.5.4. Cross flight and oblique images comparison

To refine the resulting accuracy of block adjustment, several methods including the addition of images collected from different flight heights with different flight direction (cross flights) or a different angle of view (oblique) are occasionally chosen to increase the rigidity of the block. To calculate the improvement of the accuracy from both configurations, the resulting Sigma and RMSE from these bundle blocks is then compared with the resulting accuracy from the bundle block of a single flight height.

Instead of only adding cross strips in the corner of the bundle block, two bundle blocks from different flight heights were merged to get a single “full” cross flights bundle block (Figure 16). Each strip will mutually correct the deformation that occurs in the other strip and is eventually expected to produce a more rigid bundle block. The process was done in Pix4Dmapper Pro, by combining two bundle blocks from different flight heights that have been processed separately in advance. Although eventually all the AAT and BBA need to be reprocessed to ensure the two blocks seamlessly merge into one block, this method has been proven to be efficient in saving time to re-mark the 3D reference points on the images.

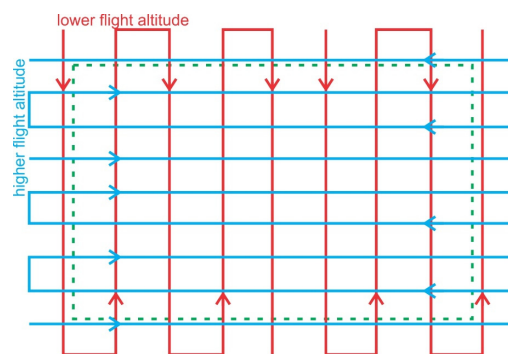


Figure 16. Cross flight pattern

In the oblique image configuration, the camera in the UAV was tilted 40° from nadir position and took images from four different sides-of-view of the study area. All images that were collected were then combined into a single bundle block. Furthermore, to check the impact of the nadir image's addition in

refining the accuracy of oblique images, the oblique images bundle block was then combined with the nadir images bundle block from the same flight height. The process was also done in Pix4Dmapper Pro with the same method in combining two bundle blocks of cross strips as mentioned above. To ensure all the images from two merged bundle blocks are tied together, the aerial triangulation and BBA processes have to be reprocessed.

3.5.5. Point cloud comparison

As the most of the 3D derived products are generated from a dense point cloud, a test involving the densified point cloud was conducted in this research. A point cloud comparison was carried out to give a clear view of how the surface type can affect the accuracy of the derived point cloud. Several sparse point clouds were chosen to be further processed in the densification process. All sparse point clouds were densified using the same method; the minimum number of matched images was three and the matching window size was 7×7 pixels. The image scales used to compute the additional 3D point cloud were multiple scales from half, quarter, and eighth image size. The detailed process of the point cloud comparison can be observed in Figure 17.

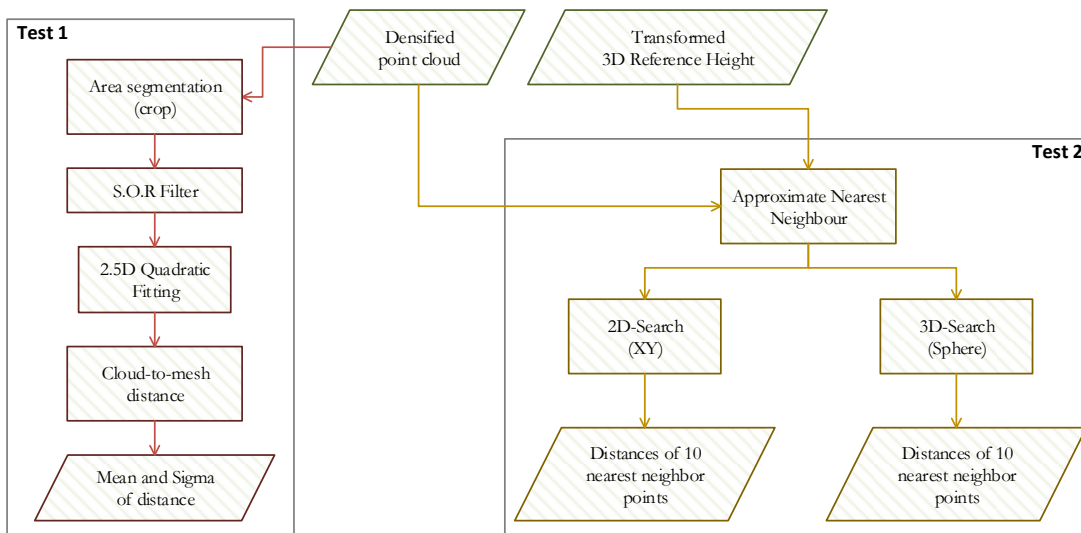


Figure 17. Workflow of point cloud comparison

Before measuring the deformation of densified point clouds, a test involving different densified point clouds was conducted by taking a sample area with the exact size from each dense point cloud (Test 1). This test was carried out to determine the impact of different image acquisition scenarios and surface types on the derived dense point cloud. The derived densified point cloud from selected bundle blocks were compared with its surface meshes using CloudCompare (CloudCompare Version 2.6.2 64-bit, 2015). To get an equal area of measurement, all the densified point clouds were cut simultaneously with an area of approximately 100 square metres on three different surfaces: paving setts, bare soils, and grasses. Then, a Statistical Outlier Removal (S.O.R) filter was implemented to eliminate outliers in a point cloud, prior to the surface fitting process. The filter computes the average distance from each point to its predetermined number of nearest neighbourhoods then rejects the points that are farther than the mean distance plus its predefined standard deviation (CloudCompare, 2015)

To measure the distance of the dense point cloud to the surface, a local model needs to be created to generate an implicit surface of the point cloud, to be used as a reference surface. A 2.5D Quadratic model with a 1-metre search radius of nearest neighbourhood points was selected as a method to model the reference mesh. According to CloudCompare (2015), this method is the recommended fitting method as it

is more versatile in representing curvy/smooth surfaces. A measurement was then carried out to measure the distance between the cropped dense point cloud and its reference mesh. Later on, the impact of different flight configurations and surface types on the densified point cloud was measured statistically using Mean and Sigma values of its distance.

The second test was examining the deformation of the dense point cloud, in terms of the point spread variation, by comparing the dense point cloud with the 3D reference data. Instead of comparing the 3D reference point with the surface representation of the point cloud, a calculation of the distance of the dense point cloud to the reference point has been conducted by utilising Approximate Nearest Neighbour (ANN) Searching library (Mount & Arya, 2010). The library implements a data structure based on k -d trees. k -d trees is a useful data structure for searches involving a multidimensional search direction.

To compute the distance between two point clouds using nearest neighbourhood distance, the distance will be measured from one point in the reference cloud to the compared cloud (Figure 18). This step will give an acceptable approximation of distance if the reference point is dense enough, as in densified point clouds.

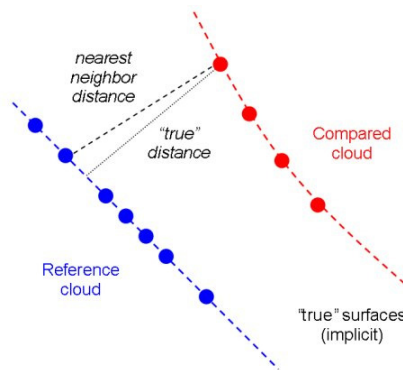


Figure 18. Nearest neighbourhood distance calculation

The method used in this calculation was that each point in 3D reference heights searched for the 10 nearest points on the dense point cloud. There were two approaches used, 2D and 3D searches. The 2D-search method restricts the software to search points within radius one metre in a planar (XY) direction while freeing up the search distance in the Z direction. Whereas the 3D-search method restricts the searching direction within radius one metre in all XYZ directions (sphere). By freeing up the search in the vertical direction, this method will take into account all vertical errors from a matching point in the surrounding of the reference points, even if the error is large. While, the 3D-search method will eliminate the large error as an assumption that a large error point is usually an outlier.

Nevertheless, neither method is the method used to generate a surface representation from a dense point cloud. To create a surface representation, an algorithm will not take into account the reference point; instead, it will seek some nearest points on a segment of the dense point cloud to represent a surface. The nearest point search method, however, is selected to give an estimation of the possible error in the matching points as a response of the land surface, and is not merely calculates the final error of the surface representation product. The output of the 2D-search and the 3D-search methods were data of distance measurements from one point in 3D reference height to each point of the 10 nearest points.

4. STUDY AREA AND DATA ACQUISITION

4.1. Study area

In 2003, a cross-border regional garden show was held in Gronau, North Rhine-Westphalia, Germany. As part of the show, an amusement park was built near Gronau train station. The park was named *Landesgartenschau*, German for the regional garden show, abbreviated as Laga. The park has a variety of landscapes and land surfaces: a pyramid covered by grass with a peak height of around 14 metres from the ground, paving setts, water ditch, gravel, sand playground, trees, and buildings. All of these types of surface can be gathered from an area of around 6.3 hectares (Figure 19). All different types of landscapes and surfaces will bring a good surface parameter to analyse the impact of land surface on the image matching process. The Laga Park stood within 10 km of the ITC building; the nearest point of the RTK base station network system (cf. section 3.3). This network was used to collect the coordinate position of the 3D reference points throughout the park.

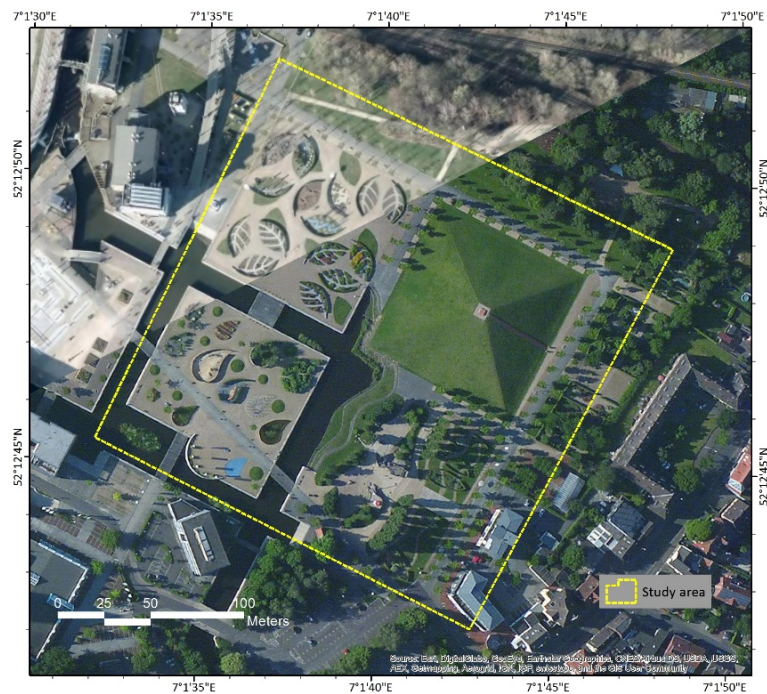


Figure 19. The study area

4.2. Flight planning

To achieve a good quality of the image data, careful flight planning needs to be conducted. Adequate flight planning is required to guarantee all the research questions can be answered accurately. Two rotary blade UAVs and one fixed-wing UAV were used in this research: hexacopter Aibot X6 attached with Canon EOS 600D and Voigtländer Color-Skopar 20 mm F/3.5 SL-II-N Aspherical Lens, quadcopter DJI Phantom 2 Vision+ with a built-in camera, and a fixed-wing Sensefly Ebee RTK attached with Sony Cyber-shot WX. The Aibot X6 is an industrial grade UAV with 3.4 kg of dead weight, ensuring excellent stabilisation compared with the DJI Phantom 2 Vision+, which is mainly used for recreational aerial photography and videography. Meanwhile, the Ebee RTK is a survey-grade mapping fixed-wing drone equipped with the RTK system, ensuring a precise positional accuracy even without Ground Control Points. Despite their prices, the UAVs have different specifications as shown in Table 2.

Table 2. Aibot X6, DJI Phantom 2 Vision+ and Ebee RTK specification comparison

Specification	Aibot X6 with Canon EOS 600D and Voigtlander 20 mm lens	DJI Phantom 2 Vision+	Ebee RTK
Length/ Width / Height	105 × 105 × 45 cm	35 × 35 × 19 cm	Wingspan: 96 cm
Dead weight	3.4 kg	1.0 kg	0.73 kg
Max. payload	2.0 kg	350 g	-
Max. speed	13.8 m/s	15 m/s (not recommended)	25 m/s
Communication distance	Up to 1,000 m	Up to 1,000 m	Up to 3 km
Flight time	30 mins	25 mins	40 mins
Sensor	Canon EOS 600D & 20 mm lens Sensor size : 22.3 × 14.9 mm Resolution : 5184 × 3456 pixel Pixel size : 4.3 μm Focal length : 20 mm	Built-in Camera Sensor size : 6.17 × 4.55 mm Resolution : 4384 × 3288 pixel Pixel size : 1.4 μm Focal length : 5 mm	Sony Cyber-shot WX RGB Sensor size : 6.169 × 4.627 mm Resolution : 4896 × 3672 pixel Pixel size : 1.26 μm Focal length : 4.57 mm
Estimated Price	€ 40,000	€ 1,000	€ 35,000

According to the influencing parameters that need to be tested in this research, 19 different flight configurations were arranged for all UAVs: 12 flight configurations for Aibot X6, four flight configurations for DJI Phantom 2 Vision+, and 3 flight configurations for Ebee RTK (Table 3). The Aibotix AiProFlight Version 2.7.0.18942 (Aibotix, 2015) was utilised to configure the Aibot X6. The software was used to set some of the Aibot X6’s flight parameters such as the flight altitude, flight speed, and expected image overlaps, with respect to its attached camera’s parameters. Figure 20 shows an Aibot X6 flight configuration in AiProFlight software. The configuration was 50 metres flight altitude, 4 m/s groundspeed, in a strip flight pattern. The yellow areas indicate the image footprint while the white bullets illustrate the nadir position of the image (waypoint), the point where the UAV should take a picture. With 90% forward overlap and 50% lateral overlap, the image footprints are highly overlapped.

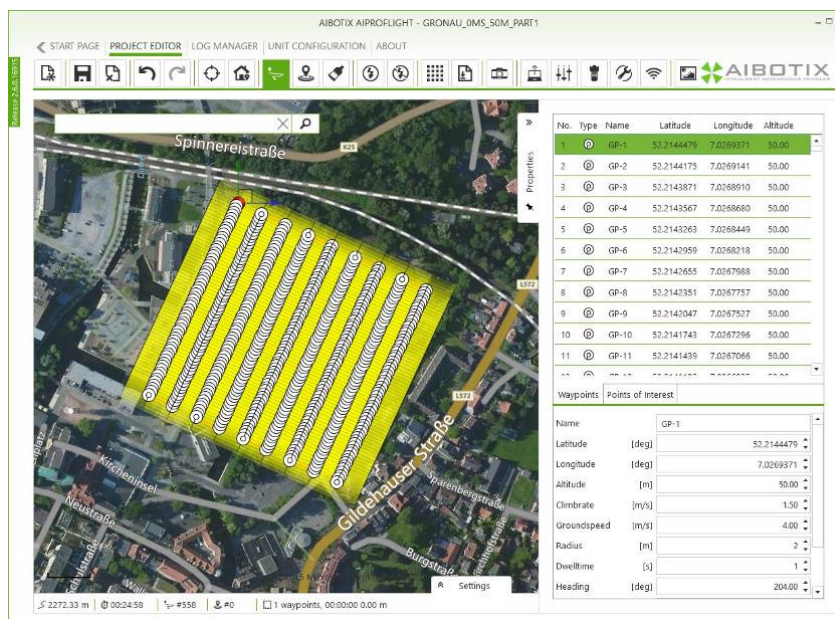


Figure 20. Aibot X6 flight configurations in Aibotix AiProFlight software

However, the mission planning software was only able to create maximum 500 waypoints, which insufficient to cover all the study area with a high forward overlap configuration. Moreover, considering the distance between two waypoints in the 90% forward overlap was only 3.7 metres, a waypoint could be easily skipped especially in a higher flying speed configuration such as Flight-5. To overcome with this issue, a camera firmware add-on Magic Lantern Version 2.3 (Magic Lantern, 2014) was installed on the camera to make the Canon EOS 600D camera on the Aibot X6 can automatically take a picture with a 1-second interval.

To manage the flight of the DJI Phantom 2 Vision+, an Apple iOS application Pix4Dmapper Capture Version 0.4.0 (Pix4D, 2015a) was used. The Pix4Dmapper Capture was adopted to control the DJI Phantom 2 instead of the native DJI application ‘DJI Vision’ because of its ability to create a grid mission, although not many camera configurations can be set on this flight manager. Moreover, the Pix4Dmapper Capture provides more accurate image geolocation estimation. The image geolocation in the native software is not accurate enough for measurements because the GPS milliseconds are not taken into account. The detailed flight configurations for both UAVs are shown in the table below.

Table 3. UAV flight configuration

<i>UAV</i>	<i>Flight Num.</i>	<i>Flight Speed (metre/ sec)</i>	<i>Shutter Speed</i>	<i>ISO</i>	<i>Altitude (metre)</i>	<i>Overlap (forward/ lateral)</i>	<i>Flight Pattern</i>	<i>Description</i>
Aibot X6 with Canon EOS 600D and 20 mm lens	1	0	1/250	800	50	90/50	South/North	Main flight
	2		1/1000					
	3	4	1/250					
	4	1/1000						
	5	10	1/250					
	6	4	1/1000					
	7		1/1000					
	8	1/1000	80	93/50	West/East	Main flight/ Cross flight		
	9	4	1/1000	800	50	80/50	South/North	Oblique 40° (4 view directions)
	10						North/South	
	11						West/East	
	12						East West	
DJI Phantom 2 Vision+	13	3	Auto	Auto	50	90/60	South/North	Main flight
	14				60			
	15				70		West/East	Main flight/ Cross flight
	16				80			
Ebee RTK	17	12	Auto	Auto	70	80/75	South/North West/East	Main flight
	18				70	70/50	West/East	No RTK enabled
	19				80	70/50	South/North	No RTK enabled

Due to the inability of the Pix4Dmapper Capture to acquire image data for the DJI Phantom 2 with a fixed shutter speed and ISO, the shutter speed and ISO were set to automatic, making the measurement of the impact of different camera settings impossible with the DJI Phantom 2. The overlap was set to “high”, which according to the Pix4Dmapper Capture supports is equal to 90% forward overlap with 60% lateral overlap.

Due to the limitation of the UAV or mission planning software, not all the tested parameters can be fully implemented in every UAV. Nevertheless, almost all parameters can be analysed in Aibot X6 except the use of RTK-based direct georeferencing. The list of utilisation of every flight configuration to analyse the influencing parameters can be seen in Table 4.

Table 4. List of flight configurations used to analyse the tested parameters

<i>Parameter</i>	<i>Flight Number</i>		
	<i>Aibot X6</i>	<i>DJI Phantom 2 Vision+</i>	<i>Ebee RTK</i>
“Reference” image	1, 2	-	-
Motion blur	2, 3, 4, 5	-	-
Flight overlap	4, 7	13, 15	17, 19
Cross flight	4, 6, 7, 8	13, 14, 15, 16	17, 19
Oblique view	9, 10, 11, 12	-	-
Flight altitude	4, 6, 7, 8	13, 14, 15, 16	17
Acquisition mode	2, 4, 5	-	-
Number and distribution of GCP	All	All	All
Image initial position	2, 3, 4, 5, 6, 7, 8	13, 14, 15, 16	17, 18, 19

Flight-1 and Flight-2 were set as a reference for Aibot X6 image data. Both configurations had no linear motion blur. The difference between the two was only the depth of field gathered from the camera. Slower shutter speed means more incident light entering the camera. To get a photograph with a normal exposure, the camera diaphragm is adjusted to compensate for a lower shutter speed, resulting in a deeper field that appears in acceptably sharp focus in a photograph. However, this type of configuration was impossible to be applied on DJI Phantom 2, due to the inability of the UAV to collect the data in stop mode by using the respective software.

Flight numbers 2, 3, 4, and 5 for Aibot X6 were applied to analyse the impact of linear motion blur on the block adjustment accuracy. Using theoretical image motion formula (Equation 3) the expected motion blur due to the combination of flight speed and shutter speed could be measured as shown in Table 5. The GSD size was used as a comparison because an image can be considered sharp when the linear motion blur distance is less than the sampling distance. However, the shutter speed of Flight numbers 13, 14, 15, and 16 of DJI Phantom 2 was calculated based on an average shutter speed of the acquired images.

Table 5. The expected motion blur on the image

<i>Flight Number</i>	1 & 2	3	4	5	6	7	8	13	14	15	16	17	18	19
<i>Flight speed</i> (m/s)	0	4	4	10	4	4	4	3	3	3	3	12	12	12
<i>Shutter speed</i> ($1/\times$)	1000	250	1000	250	1000	1000	1000	200	200	200	200	125	125	125
<i>Flight altitude</i> (m)	50	50	50	50	60	70	80	50	60	70	80	70	70	80
<i>Expected blur on sensor</i> (μm)	0	6.4	1.6	16	1.3	1.1	1	1.5	1.2	1	0.9	6.3	6.3	5.5
<i>Equal to GSD size</i>	0	1.48	0.37	3.72	0.31	0.26	0.23	1.07	0.89	0.76	0.67	4.98	7.98	4.35

In particular, Flight numbers 2, 4, and 5 were also useful to justify the significance of data acquisitions in a stop mode. The Flight-4 and Flight-5 which were taken in cruising mode, whereas Flight-2 which was taken in the stop mode. The resulting accuracy from both flying modes then compared to justify how necessary a stop mode in refining the achievable accuracy.

To analyse the impact of the flight altitude to the block adjustment accuracy, Flight numbers 4, 6, 7, and 8 for Aibot X6 and Flight numbers 13, 14, 15, and 16 for DJI Phantom 2 were used. By a combination of Flight number 4 with 7, 6 with 8, 13 with 15, 14 with 16, and 17 with 19, the influence of cross flight addition to the main flight can be evaluated with respect to the improvement of its accuracy. Furthermore, Flight numbers 9, 10, 11, and 12 were adopted to check the significance of oblique image addition to the block adjustment accuracy of the Aibot X6 images. The camera angle was set to 40° from the nadir.

The Aibotix AiProFlight software calculated the expected forward overlap of the Aibot X6 in a stop mode. Further, the forward overlap in a cruising mode was computed from the footprint assumption of the image on the flat area. With a 1-second interval between two consecutive images, the calculated forward overlap for each configuration is shown in Table 6.

Table 6. The expected forward overlap of the Aibot X6 in cruising mode

Flight Num.	GSD (cm)	Image Footprint (m)	Forward Overlap	
			Metre	Percent
3	1.07	55.75 × 37.16	33.16	89
4	1.07	55.75 × 37.16	33.16	89
5	1.07	55.75 × 37.16	27.16	73
6	1.29	66.9 × 44.6	40.6	91
7	1.5	78.05 × 52.03	48.03	92
8	1.72	89.2 × 59.46	55.46	93

A higher percentage of forward overlaps (around 90%) was chosen due to the need to determine the significance of image overlap to the derived products quality. By only removing the intermediate image among the three sequence images, another image dataset with around 80% forward overlap is obtained. Furthermore, by removing two middle images among four sequence images, the dataset with around 70% forward overlap is obtained. The list of “derived” image datasets used to analyse the impact of forward overlap reductions to the achievable accuracy is shown in the table below.

Table 7. Forward overlap percentage of the derived image-sets

Flight Number	Original forward overlap (%)	1 image deduction (%)	2 images deduction (%)
4	89	78	67
7	92	84	76
13	90	80	70
15	90	80	70
17	85	70	55

4.3. GNSS survey

There were two types of 3D reference points: natural targets and signalised targets (Figure 21). The natural target is a target point that is permanently available in the study area, and will not easily change during the period of data acquisition. The natural target is not always a natural feature; it can be an artificial or manmade feature as long as it has a fixed position. This natural target can be measured independently from the UAV image acquisition. Whereas, the signalised target is a temporary feature placed in an area where a natural

target is not available. Due to its temporary nature, the measurement of the position of the signalled target is highly dependent on the UAV image acquisition, to ascertain the position of the signalled feature on the image has not changed from the measured position.



Figure 21. Example of targets: signalled target (left) and natural targets: corner of concretes (middle), manhole (right)

There were various shapes of natural targets used as GCP or checkpoints in this research. Each of these shapes should have a good contrast with its background, guaranteeing a high visibility on the UAV images. Circular manholes and hydrant holes were preferred as natural targets. The reason for this is that defining the centre of a feature in the image is easier than the corner of a feature. Unlike the corner of a feature, the spatial ambiguity due to the pixel size in the centre of a feature can be suppressed. Thus, it may be possible to obtain a point with greater precision. However, establishing the centre of an object in the field such as a manhole has never been easy. A measuring tape was used to measure the diameter of the manhole, and the centre of the manhole was established by knowing its radius. However, some features such as a sharp corner of concrete, paving setts and rock boulders were also used as natural targets. These features were easily determined in the field, although they were difficult to be precisely defined in the image.

For time efficiency in taking 3D profile points, the DTM created was not a DTM that showed every detail of the landscape profile of the whole study area. The DTM had detailed height information only for selected land surfaces throughout the study area, which were used as reference planes in the block deformation analysis later.

4.4. UAV image data acquisition

UAV data acquisition was conducted over three days, from morning to afternoon. Three different types of UAV were used to collect the data: Aibot X6, DJI Phantom 2 Vision+, and Ebee RTK (Figure 22). Weather conditions during image acquisition on the first day were cloudy and partly sunny on the second day with a calm to light wind on both days. In contrast, the weather was sunny yet windy on Day-3. Ideally, the image acquisition should be done when the sun is directly above the site being photographed, eliminating shadows in the images. However, since the acquisition dates were in the autumn season when the sun is always at a low angle on the southern horizon during the day, there would almost always be some shadows in the images collected.

Due to a lower light availability caused by cloudy weather, the Aibot X6's camera ISO was set at 800. However, the cloudy weather has some benefit to the resulting images; all the images collected on Day-1 have a flat illumination with no shadows in the images. On Day-2, the weather conditions were cloudy with no direct sunlight in the morning but sunny with a direct light in the afternoon, resulting in different illuminations with strong shadows in the images.

Concerning the sunlight, sun-flares that fade out parts of the captured images was not an issue for nadir image acquisition when the camera was fixed and pointing downward. The sun angle had to be properly addressed when taking oblique images. For this reason, the oblique image acquisitions were done during the noon, when the sun angle reaches its peak.

Although the wind speed had not really been calculated in the flight planning, wind can interfere with data collection. On a windy day, estimated at 4 on the Beaufort scale based on weather prediction software, the DJI Phantom 2 Vision+ had trouble finding a fixed starting location in the grid to start the mission. These conditions forced the DJI Phantom 2 Vision+ to abort the mission, making it impossible to perform the image acquisition. Meanwhile, the Aibot X6 managed to start the mission, but the windy conditions forced the UAV to consume more energy than usual, especially when flying against the wind. These conditions forced the UAV to abort several later missions due to running out of battery.



Figure 22. UAV employed on the research: Aibot X6 (left), DJI Phantom 2 Vision + (middle), and Ebee RTK (right)

For time efficiency, all the UAVs were flown about the same time, with different flight altitudes to avoid collisions in the air. Due to the battery power limitations, each configuration of the Aibot X6 and DJI Phantom 2 Vision+ had to be split into two parts to cover the whole area. However, not all of the flight configurations could be completely performed. Because of battery limitations, Flight-1 and Flight-2 failed to cover the entire study area. These flight configurations only finished about half of the study area. Anyhow, they recorded the area where the Siemens Star and Koren Chart were placed. As well as Ebee RTK Flight-18 and Flight-19, the images were collected without RTK solutions due to communication connection failures between the Ebee RTK and its base station, giving roughly the same image initial position accuracy as the other UAV.

The A0-size Siemens Star and Koren Chart had been placed on a flat terrain during data acquisition (Figure 23). The charts ideally should be located in the middle of the images, where the influence of the lens distortion is minor. However, this condition was tough to obtain, since each flight configuration has its own flight pattern and the wind can randomly force the UAV to veer off its path.



Figure 23. The Siemens Star and Koren Chart

5. RESULTS

5.1. Data Preparation

5.1.1. GNSS Survey

There were 20 natural targets and 35 signalised targets collected and used as GCPs or checkpoints. Also, 206 3D points were measured to create 3D reference height/DTM. The 35 signalised targets were divided into three acquisition dates: 11 signalised targets for UAV data acquisition on 21 October 2015, 12 signalised targets for UAV data acquisition on 23 October 2015, and 12 signalised targets for UAV data acquisition on 27 November 2015. In total, 31 points were used as GCPs and checkpoints for image datasets from 21 October 2015, 32 points for image datasets from 23 October 2015, and 32 points for image datasets from 27 November 2015. The distribution of the 3D points of GCPs and checkpoints can be seen in Figure 24. The natural targets are depicted with a purple-coloured dot while the signalised targets are presented with a red-coloured dot.

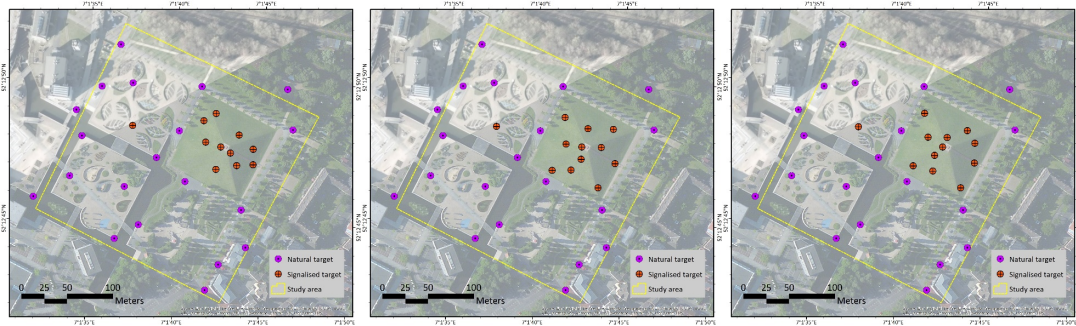


Figure 24. Distribution of the 3D control points for image acquisitions on 21 October 2015 (left), 23 October 2015 (middle), and 27 November 2015 (right)

The obtained 2D accuracy of each point measurement lay within 6-15 mm with the 3D accuracy around 10-20 mm. Lower accuracies were observed in the northern area of the pyramid, where an area of fairly dense trees existed. To improve the accuracy, each point that would be used as a control point and checkpoint was measured twice, and the average value from both measurements was taken as the fixed coordinate numbers.

Based on the calculation of GNSS measurement difference, the 2D position sigma from the first and second measurements were 1.3 cm for X and 2 cm for Y, which were around double the smallest GSD size (1 cm). Nevertheless, the standard deviation of Z measurement was 1.8 cm; around the same of the average theoretical vertical accuracy. Ideally, the reference error should be lower (higher accuracy) than the measured one. However, the resulting GRD of the images are practically more than the size of the GSD because of the positional error from the GSD was propagated by the errors from motion blur and lens aberrations. Hence, the GNSS measurement result is still acceptable in the sense that the overall 3D positional error is not more than double the GSD size.

ArcGIS for Desktop Version 10.3.1 (Esri, 2015) was used to check the distribution of the 3D profile points and to create a Triangulated Irregular Network (TIN). The resulting TIN was useful to justify whether the collected 3D points were sufficient to represent some features in the study area or not, especially in the pyramid. Although the pyramid seems to have a simple shape, it takes many 3D profile points to ensure the pyramid surface can be presented correctly. The distribution of 3D profile points and the resulting TIN are shown in Figure 25. The colour scale of the pyramid and the other surfaces is different. In the pyramid, the 1-metre interval was used while the colour interval in other surfaces was 1 centimetre.

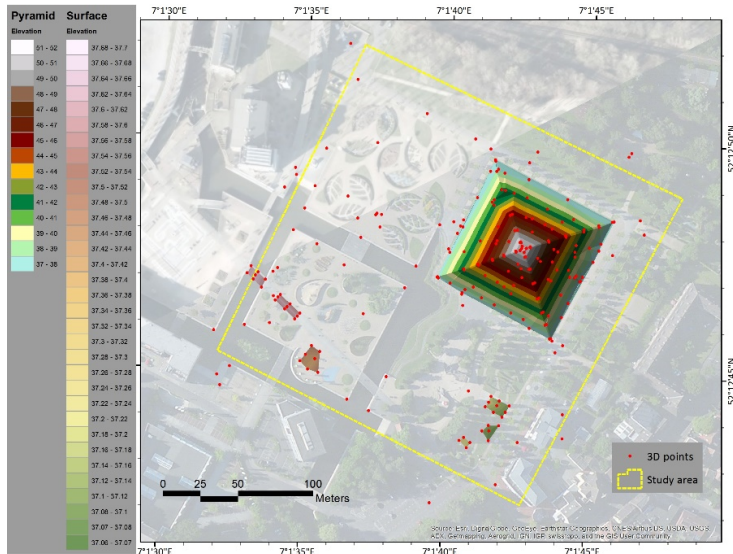


Figure 25. Distribution of 3D profile points and its resulting TIN

The obtained TIN demonstrated the sufficiency of the 3D points in representing the selected surface area. Although there were several bizarre sightings in the pyramid-ridge due to incorrect interpolation, this was not a problem since the resulting TIN was only to be used for evaluation.

5.1.2. The resulting UAV images

Although the image area coverage of every flight configuration had been carefully planned, not all the resulting coverages were in a perfect condition as intended. All image coverages with the Aibot X6 in the nadir image configuration show perfect results as planned. The DJI Phantom 2 records a smaller area than what had been planned due to wireless communication limitations between the remote and its UAV. Although the entire study area can eventually be covered by taking advantage of the ultra-wide angle lens in DJI Phantom 2, exploiting the image area on the outer side of an ultra-wide angle lens means increasing the expected error due to accepting larger displacement of the lens applied. However, the resulting images from the Ebee RTK were in an uneven distribution even though the Ebee RTK was flown in a strip pattern. However, it still had good area coverage throughout the study area.

Due to a combination of faster flight speed and lower shutter speed, the resulting images from the Ebee RTK were moderately blurred; around five times its GSD size. This problem arises due to the inability of the Ebee RTK, and most fixed wing UAVs, to fly at a lower speed like a rotor blade UAV. A lower camera shutter speed could not be avoided as a compromise on a low availability of incident light. As a result, none of the signalled targets could be used in the Ebee RTK accuracy assessment process. Only natural targets could be used in the bundle block of the Ebee RTK.

A problem with the utilisation of the outer edge of the image from an ultra-wide angle lens began at the initial processing step. While the other UAVs had low overall RMSE in their GCPs (0 - 0.5 cm), the GCP accuracies of the DJI Phantom 2 products were broadened up to 1.5 times of the GSD. Imprecise GCP marking was not the cause of this problem. For the GCP points situated on the edge of the image where the image distortion was high due to the ultra-wide lens used, the computed positions for some GCP marks were always inaccurate even though many marks had already been given in many other pictures (Figure 26). Apparently, the software could not seamlessly correct the lens distortion effect on the images. Consequently, it was difficult to compare definitively the resulting accuracies between the UAVs especially for the DJI Phantom 2 due to this low GCP accuracy. As shown in Figure 26, the yellow mark is the mark of the GCP position that was manually added to the image to define the actual position of the GCP on the image, while

the green mark is the computed point position of the GCP based on the average positions of the manual marks on the reprojected images.

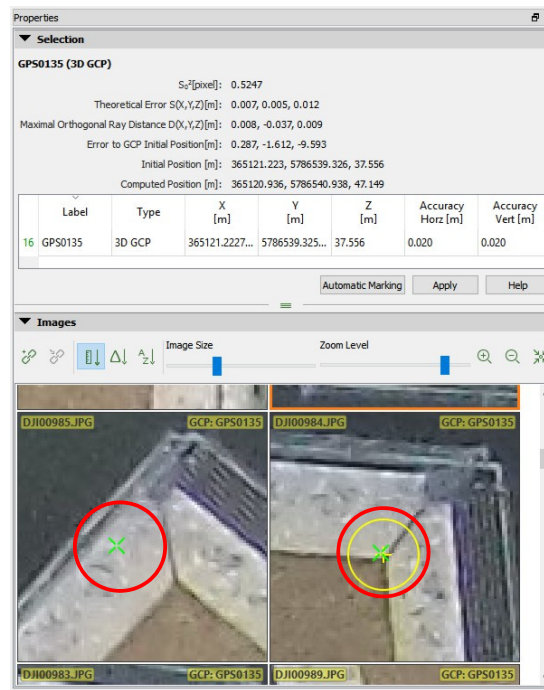


Figure 26. Inaccurate initial GCP marking due to the remaining error from lens distortion

Because the zero altitude of the UAV was calculated from the flat area of the study area, the critical issue of the overlapping images was in the pyramid area. Based on GNSS measurements, the height of the pyramid is around 14 metres from the average of the flat area. At the top of the pyramid, the distance between the pyramid and the UAV at a 50-metre flight altitude was only 36 metres, reduced around 30% from its initial flight altitude, which will eventually affect the percentage of the image overlap on the top of the pyramid for lower flight altitudes.

By running the initial process in Pix4Dmapper, the quality of overlapping images in the bundle block could be justified. From the Quality Report, the overlapping images of all flight configurations were as good as expected with more than five overlapping images covering the study area. The number of overlapping images and the resulting DEM before densification can be seen in Appendix 1.

5.2. Ground Sampling Distance and Ground Resolved Distance

Since the GSD is obtained from the camera pixel size and multiplied by the scale, the GSD value of several configurations with the same UAV will remain constant even if it has different expected motion blur. On the other hand, the GRD value is highly dependent on the lens quality, f-stop being used during data acquisition, and the motion blur gathered. The GRD value in this research had been calculated by using Imatest Master Version 4.2.9 (Imatest, 2015a) by utilising the Koren Chart that was already captured in the image in every configuration. MTF50 was used as the value for the MTF result.

The comparison between the resulting GSD and GRD for each flight configuration is shown in Table 8. However, due to computation limitations in accepting a minimum number of pixels in the area of calculation, it failed to measure the MTF for all UAVs in flight altitude above 60 m. The MTF calculation results for all images from UAV configurations above 60 metres were zero.

Table 8. GSD and GRD comparison

Flight Number	Pixel size (μm)	Focal length (mm)	Altitude (m)	GSD (cm)	MTF (LW/PH)	GRD (cm)	GRD vs. GSD (\times GSD)
1	4.3	20	50	1.075	3037	1.223	1.14
2	4.3	20	50	1.075	2696	1.378	1.28
3	4.3	20	50	1.075	2538	1.464	1.36
4	4.3	20	50	1.075	2446	1.519	1.41
5	4.3	20	50	1.075	1692	2.196	2.04
6	4.3	20	60	1.290	3142	1.419	1.10
7	4.3	20	70	1.505	-	-	-
8	4.3	20	80	1.720	-	-	-
13	1.4	5	50	1.400	3289	1.400	1.00
14	1.4	5	60	1.680	3221	1.715	1.02
15	1.4	5	70	1.960	-	-	-
16	1.4	5	80	2.240	-	-	-
17	1.26	4.57	70	1.929	-	-	-

The resulting GRD from Flight-1 and Flight-2 show that without any motion blur the GRD value still exaggerates because of a different f-stop being used when taking the image. In Flight-1, the lens diaphragm is f/11 while in Flight-2 the lens diaphragm is f/3.5. A lower number of lens diaphragm (large aperture) will increase the lens diffraction; it will eventually reduce the sharpness of the resulting image.

The motion blur proved to have a significant impact on the GRD. For both f-stops, the motion blur increment tends to correlate linearly with the increase in the GRD size as shown in Figure 27. The unit used in this figure is the respective value of the parameter in its GSD size. The effect of motion blur on the GRD size is larger than the impact of the f-stop. The aperture of f/11 is just two stops under the maximum stop (f/22), and if it was added with the motion blur as much as one and a half times GSD size, the resulting GRD is already bigger than the GRD from f/3.5 with no blur. From the chart, it can also be inferred that using a small aperture opening while maintaining the motion blur below one GSD is the best option to overcome the lens diffraction issue.

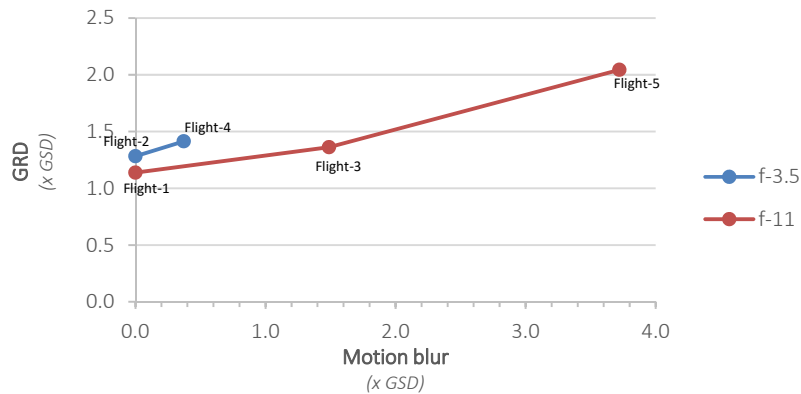


Figure 27. Correlation of the motion blurs with the GRD

Flight altitude was also demonstrated to have significance to the GRD size as shown in Flight-4 and 6. The amount of the motion blur was diminished by the higher the UAV flew. This relation will eventually abate the GRD ratio to its GSD, although the actual size of GRD also enlarges due to flight altitude increments. However, in the DJI Phantom 2 cases, because the resulting images have experienced strong image sharpening directly on the camera, the impact of the motion blur on the images was eradicated, resulting in a GRD size almost equal to the GSD size.

5.3. Theoretical vertical accuracy

The theoretical vertical accuracy of each flight altitude was calculated based on Equation 7, as displayed in Table 9. As an assumption, five images were overlapped in the 90% forward overlap scenarios. Particularly in Flight-5 assumed only three images overlapped due to this configuration only having 73% forward overlap. The expected x positional accuracy (σ_x) was a third of pixel size.

Table 9. Theoretical vertical accuracy

UAV	Flight Number	Altitude (m)	Baseline (m)	Focal length (mm)	Precision of x (σ_x) (μm)	Vertical error (cm)
Aibot X6	1, 2	50	3.71	20	1.43	1.53
	3, 4	50	4	20	1.43	1.42
	5	50	10	20	1.43	1.27
	6	60	4	20	1.43	2.04
	7	70	4	20	1.43	2.78
	8	80	4	20	1.43	3.63
DJI Phantom 2 Vision+	13	50	4.63	5	0.47	1.59
	14	60	5.55	5	0.47	1.91
	15	70	6.48	5	0.47	2.23
	16	80	7.40	5	0.47	2.55
Ebee RTK	17	70	10.62	4.6	0.42	1.34
	18	70	21.25	4.6	0.42	0.67
	19	80	24.29	4.6	0.42	0.77

From the vertical accuracy calculation, the configuration parameters that can be easily changed are flight altitude and baseline. Although the UAVs fly at an identical altitude, it is likely they have different vertical errors due to different focal lengths and pixel sizes that eventually govern the expected parallax error. However, it is clear that the main influence on the theoretical vertical accuracy is flight altitude. The accuracy will become twice as bad if the flight altitude is doubled compared with a half-reduced baseline. Certainly, Flight-5 that has the lowest flight altitude and longest baseline in the Aibot X6, has a better theoretical vertical accuracy than the other configurations.

5.4. Impact of GPS initial position on the resulting accuracy of BBA

5.4.1. Experiment results

While the theoretical vertical accuracy is measured based on the predefined values in an ideal scenario, the actual vertical accuracy is calculated based on the resulting accuracy of the bundle block adjustment of the images. Pix4Dmapper Pro Version 2.0.100 (Pix4D, 2015b) was used to compute Aerial Triangulation and Bundle Block Adjustment (BBA) for each configuration.

To see the influence of direct georeferencing on the resulting accuracy of BBA, all BBAs were processed without GCPs. Direct georeferencing is used to determine the initial position of the image. As the three UAVs use a different quality of GPS/IMU in the direct georeferencing, this experiment is important to assess its significance to the resulting BBA accuracy improvements. While the Ebee RTK is obvious; the direct georeferencing process for the Aibot X6 and DJI Phantom 2 relies on the code-phase GPS attached to the UAV, which supposedly has different quality of the positional approximation.

In this experiment, all control points were used as checkpoints. The resulting accuracies of the BBA without control points are shown in Table 10.

Table 10. Residuals on the checkpoints of the BBA without ground control point

		Flight Number	X (cm)	Y (cm)	Z (cm)
Aibot X6	2	Sigma	13.8	13	14.5
		RMSE	39.5	97.7	129.4
	3	Sigma	10.8	13.2	21.4
		RMSE	48.3	61.2	136
	4	Sigma	31.1	32.6	45.5
		RMSE	79.2	89.9	72.4
	5	Sigma	39.9	37.8	14.2
		RMSE	51.8	105.7	98
	6	Sigma	27.3	28.3	32.4
		RMSE	105.7	37.7	32.5
	7	Sigma	31.1	39.7	8.9
		RMSE	51.4	63.5	30.5
	8	Sigma	33.5	37.4	31
		RMSE	115.9	39.9	205.8

		Flight Number	X (cm)	Y (cm)	Z (cm)
DJI Phantom 2 Vision+	13	Sigma	22.4	20.9	61.3
		RMSE	42.3	172.5	1260.4
	14	Sigma	27.3	20	92.1
		RMSE	27.3	159.1	842.6
	15	Sigma	46.8	34.8	166.8
		RMSE	53.5	236	735.1
16	Sigma	25.8	26.4	38.1	
	RMSE	96.3	65.2	657.8	

Ebee RTK	17	Sigma	2.3	1.8	2.3
		RMSE	12.8	1.8	10

From the Sigma and RMSE results, it is clear that all of the resulting accuracies have a systematic positional error, both in the horizontal and vertical position. All the results have a larger RMSE compared with its Sigma; this means that the Average of the residuals is significantly greater than zero, and eventually results in a systematically shifted point cloud.

Based on the RMSE results, systematic error apparently occurs with all UAVs. Although the Ebee RTK undoubtedly has a better initial position accuracy compared to the other UAVs, the resulting accuracy without any control points still has a systematic error in the vertical position of around 10 centimetres. Systematic error with the Aibot X6 is around 70 cm for XY-error and 85 cm for Z-error. While the DJI Phantom 2 has larger errors in all positions, around 1 metre in XY error and 8.7 metres in Z. This error is caused by the low initial positional accuracy that has been tagged into the images by the GPS. Certainly, the DJI Phantom 2 has lower initial positional accuracy due to its lower GPS quality compared with the Aibot X6.

The Sigma of most bundle blocks is large; this means that the BBA still has significant deformation. Without control points, neither flight altitude nor motion blur has a detectable influence on the resulting accuracy. The dominant factor influencing the accuracy in a bundle block without GCP is the initial position of the images, which affected randomly depending on the time of acquisition. Furthermore, the vertical position is prone to be deformed by altitude changes than the horizontal position as shown in Figure 28. However, the Z-error of a bundle block from the Aibot X6 at 70 metres flight altitude was not an outlier; this can only be unintentionally good positional accuracy as a result of incidentally receiving better GPS satellite signals. Moreover, the 70-metre flight configuration was performed on a different day than the other bundle blocks. The figure also shows that RTK features in the Ebee RTK undoubtedly give unbeatable positional accuracy to the BBA compared to the other UAVs in conditions without control points.

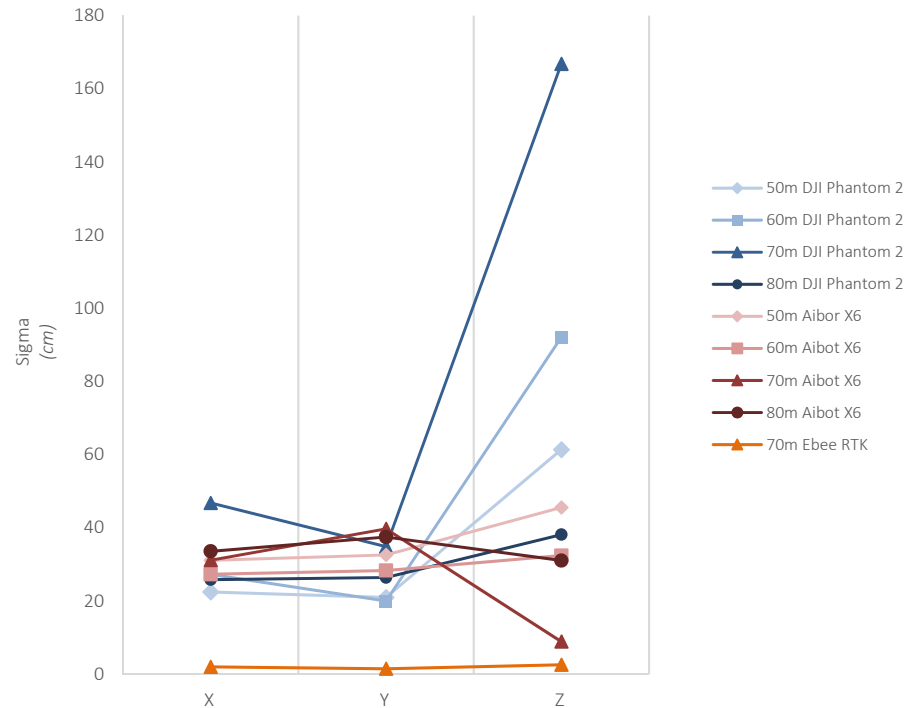


Figure 28. Residuals of XYZ at checkpoints on a block adjustment without GCPs

However, to check the impact of RTK features in refining the initial position, an experiment with the Ebee RTK dataset was conducted by deactivating the initial position from RTK and changing the initial position to “standard” initial positions: 5 metres in XY and 10 metres in Z. These initial position changes will provide a larger tolerance for an image to adjust its position during aerial triangulation and bundle block adjustment.

Still, this method was actually not adequate to compare and justify the impact of the RTK features on the resulting accuracy. Although the range of the initial positional accuracy had been changed to the same as the initial position accuracy of the Aibot X6 and DJI Phantom 2; these numbers were in any case only a tolerance range. The actual geotagged position of the image was not changed.

To obtain a fair comparison, a random number was added to the actual geotagged XYZ position of the image in the Ebee RTK. The random numbers were selected from -3 to 3 in the XY position and -5 to 5 in the Z position. These values were chosen because the accuracy of code-phase GPS commonly lies within these ranges. By changing its tolerance and initial image position, the resulting accuracy of the BBA decreased significantly. Without an accurate initial image position, the Sigma in the 0-GCP configuration of Ebee RTK decreases almost 500% with RMSE decreases of almost 100%.

5.4.2. Main findings

- The resulting accuracies have a systematic positional error, both in the horizontal and vertical position. The vertical position prone to a larger error compared with the horizontal position.
- The Sigma and RMSE of most bundle blocks are large; these mean that the BBA still has significant deformation.
- The Ebee RTK undoubtedly has a better initial position accuracy compared to the other UAVs. The error of the DJI Phantom 2 is larger than the Aibot X6.
- Without an accurate initial position, the resulting accuracy of the BBA with the Ebee RTK decreased almost six times.

5.5. Impact of distribution and number of GCPs on the resulting accuracy of BBA

5.5.1. Experiment results

Undoubtedly, without any ground control point, the positional accuracy only relies on the initial position given by the UAV's GPS, which was not sufficiently accurate; and meant that the impact of each parameter on the accuracy could not really be measured. All the BBA accuracies were then calculated with a different number of GCPs and distributions. The number of GCPs used to calculate the accuracy was 4, 5, and 10.

In the 4-GCP configuration, four GCPs were placed in every corner of the bundle block to get a horizontal distribution of GCP evenly. In the 5-GCP configuration, one control point was added at the top of the pyramid instead in the middle of the study area to also get a vertical distribution. Meanwhile, in the 10-GCP configuration, several more points were added in between the previous control points to get an even distribution of the control points.

However, the 5-GCP configuration was chosen to be tested in different distributions: evenly distributed throughout the study area and distributed narrowly in the west of the study area (undistributed). The distribution of each GCP configuration can be seen in Figure 29. Although there are slight variances in the position of the signalled targets due to the different acquisition date, all the points generally have the same distribution.

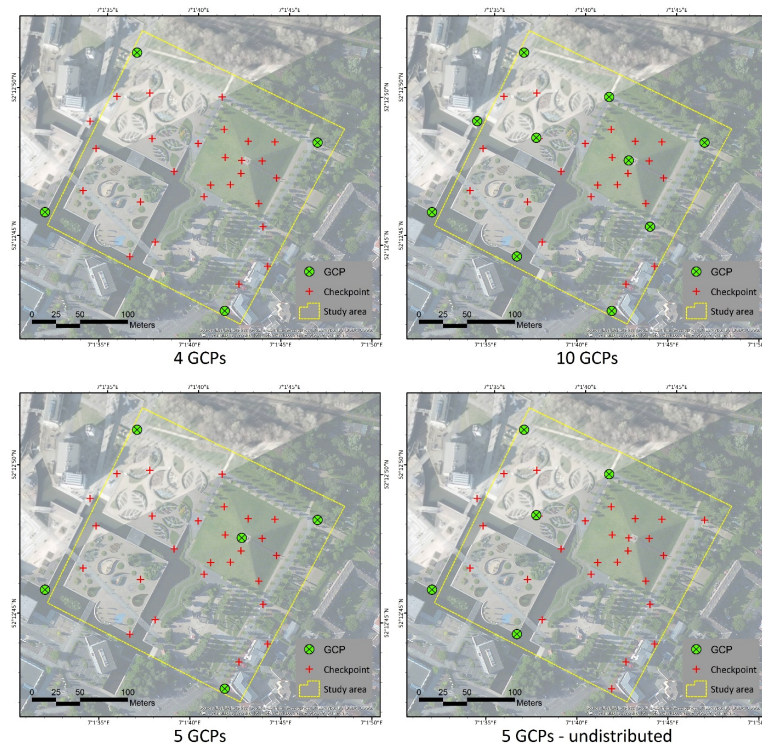


Figure 29. GCPs and checkpoints distributions

Figure 30 shows the vertical accuracy from the BBA process in every GCP scenario. Each bundle block was processed several times using a different number of GCPs: 4, 5, and 10 GCPs. Meanwhile, the impact of GCP distribution was tested in the 5-GCP configuration. The 5-GCP configuration was selected because the resulting accuracy revealed that generally the impact of systematic error from initial position error and lens aberrations was already diminished; indicated by the Sigma that is almost the same as its RMSE. Due to a failure in data acquisition in Flight-1 and Flight-2, the 10-GCP configuration could not be performed in Flight-1 whereas in Flight-2 the number of GCPs was lowered to eight CGPs. Further, on Ebee RTK Flight-17, due to highly blurred images combined with a higher flight altitude in data acquisition, no

signalised targets could be detected on the images. Only natural targets could be used in the bundle block of Ebee RTK. The 10-GCP configuration was also dropped to nine GCPs in this flight configuration. The Sigma value is presented in the lighter colour while the RMSE value is presented in the darker colour.

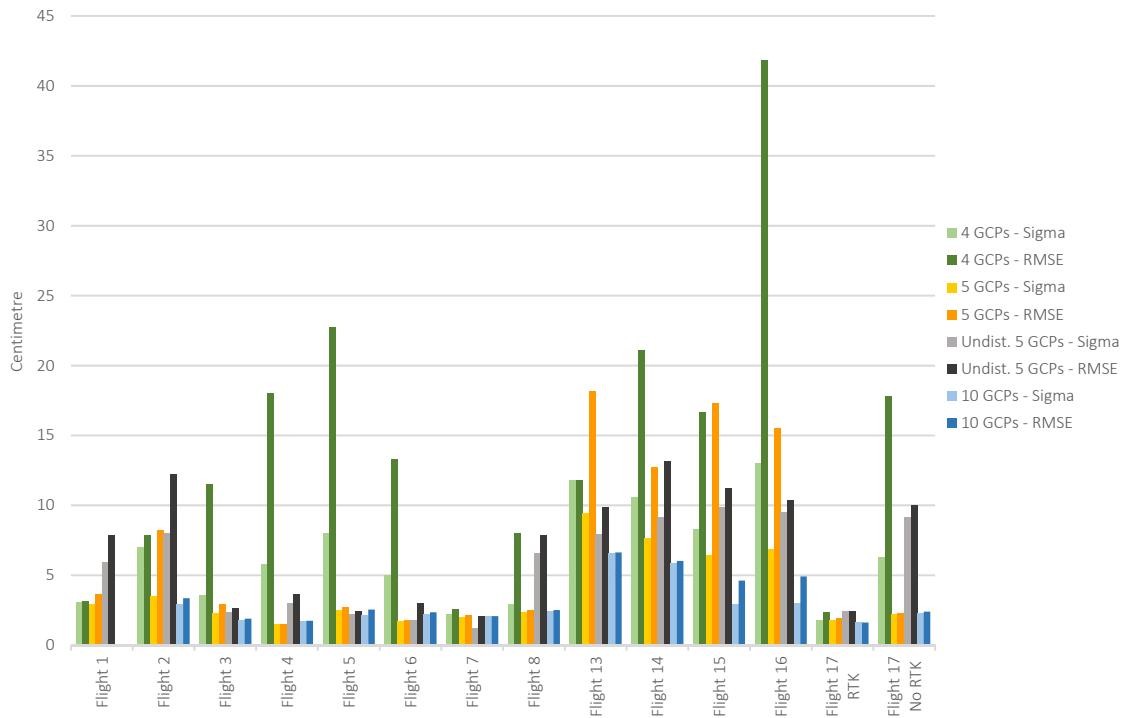


Figure 30. The resulting accuracy from different GCP scenarios

Based on the resulting BBA accuracy from several control point configuration scenarios as demonstrated in Figure 30, it is clear that the resulting accuracy is highly dependent on the amount of GCP used while the distribution of GCP also affects the suppression of systematic error in XY position (see Appendix 2 for the complete table). Indeed, the vertical accuracy is also affected by GCPs that are not evenly distributed, decreasing the vertical accuracy around 40% for both the Aibot X6 and DJI Phantom 2 compared with the evenly distributed GCPs. However, the GCP distribution mainly affects the XY position accuracy, decreasing the accuracy around 70% compared with the distributed one. The comparison of Aibot X6 Flight 7 and Ebee RTK Flight 17 reveals that the RTK installation in a UAV does not significantly improve the resulting accuracy unless taking a benefit of obtaining good positional accuracies in a bundle block without GCP. Despite the fact that Flight-17 of the Ebee RTK has a higher motion blur than Flight-7 of the Aibot X6 should also be taken into consideration.

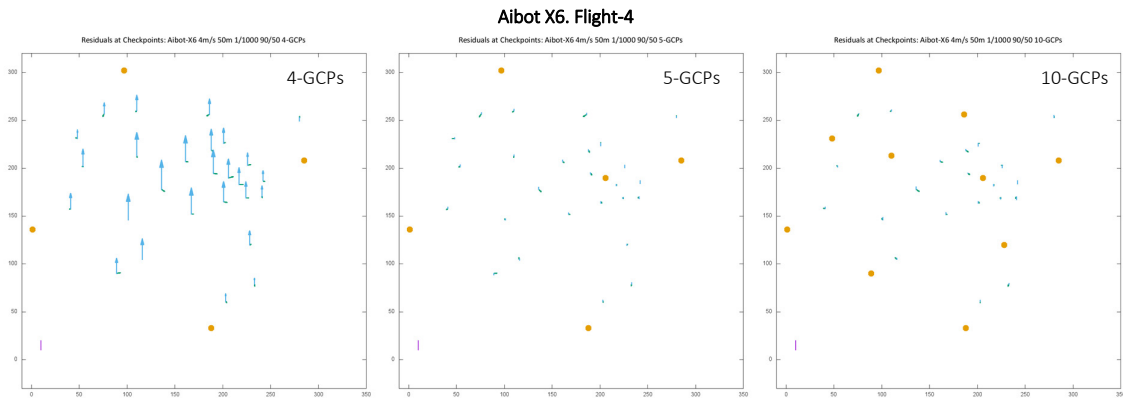
Even though, accurate image initial positions also have an impact on the accuracy refinement. As a result, the BBA of the Ebee RTK generally has the best accuracy, whereas the BBA of the DJI Phantom 2 has the worst accuracy compared with the other UAVs. In the 4-GCP configuration of Flight-17 Non-RTK, the resulting accuracy drops to 250% compared to the accuracy of Flight-17 with RTK solution. A lower initial position tolerance also increases the systematic error in the 4-GCP configuration; the RMSE decreases six times lower than the RMSE of the enabled RTK solution. Moreover, applying nine GCPs to the bundle block did not evidently generate an accuracy as good as the enabled RTK solution. Nevertheless, the accurate image initial position has an influence on the accuracy enhancements. Based on the result, the impact of the initial position on reducing the deformation of the BBA without control point is better than the influence of the GCP addition.

The comparison of the Sigma value in the well-distributed and undistributed GCPs did not demonstrate a clear pattern regarding its impact. Otherwise, from 2D plots in Appendix 3 it is clear that the undistributed GCPs cause a systematic deformation of the resulting point cloud for all UAVs, mainly with the DJI Phantom 2 and Aibot X6. However, the deformation from these two rotor-blade UAVs has a distinct pattern; with the Aibot X6, the horizontal position of the point cloud in the area without GCP is likely to be radially deformed while with the DJI Phantom 2 the deformation of its point cloud is likely to be unidirectional away from the GCPs.

The residual of XY escalates linearly with the distance increment to the GCP. The farther the point is from its GCP, the greater the residual produced. The pattern of the Sigma values cannot be clearly understood. In 5 well-distributed GCPs, the distance between each control point is far, distributing the residuals almost evenly in the checkpoints between them. Whereas, in the undistributed GCP, higher residuals in the area that does not have control points are compensated by lower residuals in the area that has control points; wherein this area now has denser GCPs than in the well-distributed 5-GCPs.

Regarding the influence of the number of GCPs on the resulting BBA accuracy, the addition of four evenly distributed GCPs would increase the vertical accuracy around 75% - 90% from its BBA accuracy without any control points with the Aibot X6. The vertical accuracy increments of the DJI Phantom 2 with the addition of four GCPs are around 65% - 95% compared with the accuracy of BBA without GCPs. However, with the Ebee RTK, the addition of four GCPs just increases its accuracy by 14% from the BBA accuracy without control points. By adding one more GCP, the vertical accuracy will increase around 45% from the 4-GCPs vertical accuracy for the Aibot X6, and 25% for the DJI Phantom 2. Adding 10 GCPs to the BBA for Aibot X6 does not have a significant impact compared to the evenly distributed 5-GCP configuration. The improvement from this addition is only about 15% in vertical accuracy. Nevertheless, the addition of 10 GCPs to the DJI Phantom 2 certainly improves its vertical and horizontal accuracy up to 40% in vertical and 30% in horizontal.

Figure 31 shows how the number of GCPs reduces the residuals in the checkpoints of the bundle block. It is also shown that since all the images already have high initial positions in the Ebee RTK, the addition of GCPs does not actually improve the block deformation. Despite this, the addition of GCPs to the Ebee RTK will eliminate the systematic error generated in the block adjustment process without GCPs. As a comparison of how the accurate initial position can suppress the residuals, the residuals from the BBA of the Ebee RTK without RTK solution is also given in this figure.



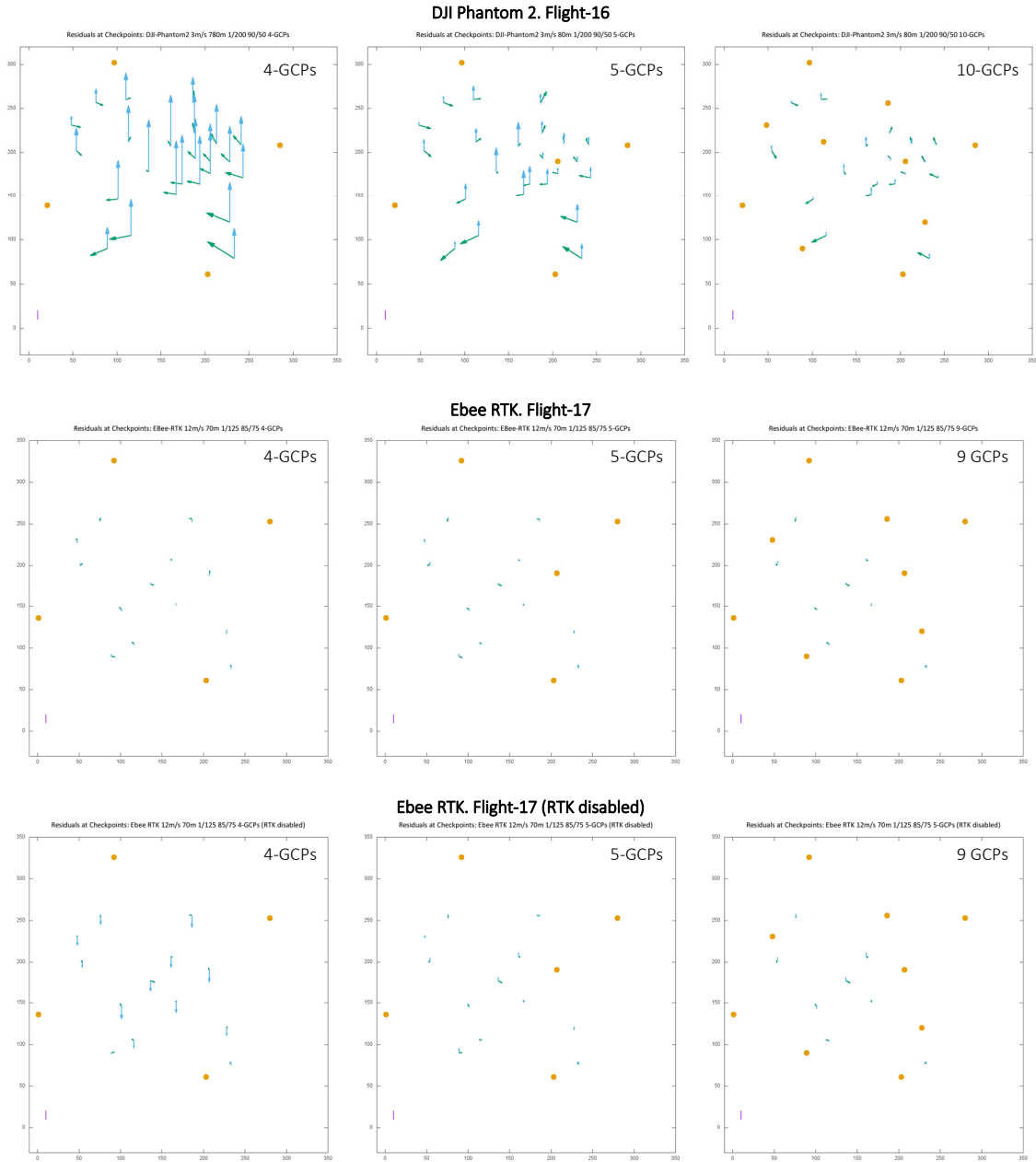


Figure 31. Deformation of point cloud in different number of GCPs

By performing side experiments, it is revealed that the distribution of GCPs in correlation with the flight altitude is a bit tricky. Placing one control point in the top pyramid could lead to different results in the BBA accuracy. In the 4-GCP configuration, instead of placing one of the points in the corner of the area, the point is moved to the top of the pyramid. At flight altitudes of 50 metres and 60 metres, the accuracies increase up to 70% compared with the “normal” 4-GCP distribution. Meanwhile, this distribution gives lower accuracies compared with the “normal” distribution at flight altitudes of 70 metres and 80 metres; the accuracy decreases by up to 30% at 80 m flight altitude. This behaviour also occurs in the 5-GCP configuration although the difference in the accuracy is only around 20%. By placing one GCP at the top of the pyramid, the resulting accuracy of the BBA at lower flying altitudes improves. Meanwhile, at higher flying altitudes, changing the position of one GCP at the top of the pyramid and moving it to the flat area

in the middle of the study area results in a higher accuracy. Figure 32 shows the differences in the resulting accuracy in the 4-GCP and 5-GCP configurations of the Aibot X6 at all flight altitudes tested.

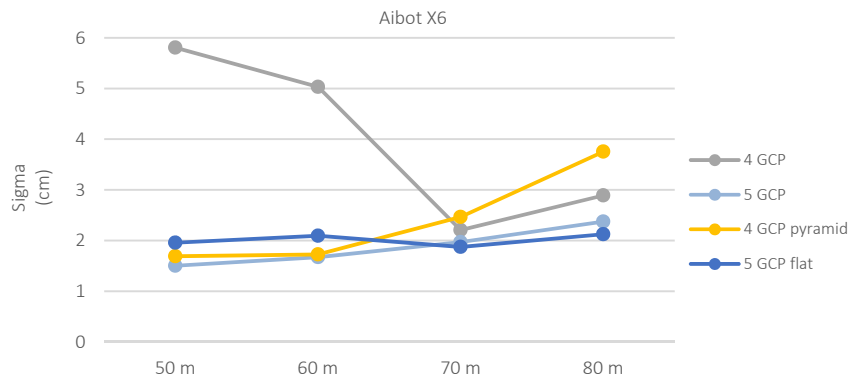


Figure 32. Differences in residuals at checkpoints in the 4-GCP configuration of Aibot X6

Referring to the graph of Aibot X6 in Appendix 4, the BBA accuracy in 4-GCPs tends to have the same pattern as its BBA accuracy without GCP, indicating that systematic error persists in both configurations. The higher RMSE value compared with its Sigma (Appendix 2) in this GCP configuration also demonstrates an identical evidence. However, the impact of the remaining systematic error in a 4-GCP configuration was already diminished at a flight altitude of 70 m. For the Aibot X6 with well-distributed 5-GCP and 10-GCP configurations, the depreciation of the BBA accuracy is linear with the increment of flight altitude. This means that the remaining systematic errors such as from the GPS's initial position and lens distortion are already repressed, leaving flight altitude as the dominant factor in determining the resulting BBA accuracy.

5.5.2. Main findings

- From the comparison between the BBA of Flight-17 with the RTK solution and without RTK solution, the impact of the initial position on the resulting accuracy of the BBA is stronger than the impact of the number of GCPs.
- Based on the comparison of the BBA with the Aibot X6 and the Ebee RTK in evenly distributed GCP configurations, the resulting accuracy of the BBA with an accurate image initial position can be rivalled by the BBA with a “standard” image initial position. Although, the difference in the degree of motion blur on both BBA is also worth considering.
- The BBA with an accurate image initial position has an advantage in maintaining small deformation in an undistributed GCP condition.
- The term “well-distributed” in 4-GCP and 5-GCP configurations depends on the flying altitude. At lower flight altitudes, where the ratio of the pyramid’s height to the flight altitude is significant, instead of placing all control points in the flat area of the corner/middle of the bundle block, the accuracy will significantly improve when one of the points is placed on the top of the pyramid. However, this scenario will be counterproductive at higher flight altitudes. From the results, the critical significance point of the ratio of the landscape height difference is 20% from the flying altitude.

5.6. Impact of flight altitude on the BBA accuracy

5.6.1. Experiment results

The impact of the flight altitude parameter on the BBA accuracy of Aibot X6 is clearly visible with 5 and 10 GCPs as shown in Figure 33. In these GCP configurations, the BBA accuracy decreases when the altitude

risers. Based on 5-GCP and 10-GCP configurations of the Aibot X6, the decrease in the resulting accuracy with the Aibot X6 is around 15% for every 10 metres of additional flight altitude.

The DJI Phantom 2, however, has a reverse pattern to the Aibot X6. At up to 70 metres flight altitude, the BBA accuracy of the DJI Phantom 2 in all GCP configurations tends to grow when the altitude increases before the impact of altitude can be reckoned. On average, the increase in accuracy is around 24% per 10-metre altitude increment. Although the accuracy of the DJI Phantom 2 starts to decrease in all GCP configurations from a flight altitude of 70 m to 80 m, the Average values of vertical residuals are still high – around 4 millimetres in 10-GCPs and 40 centimetres in 4-GCPs – indicating the systematic error still occurs.

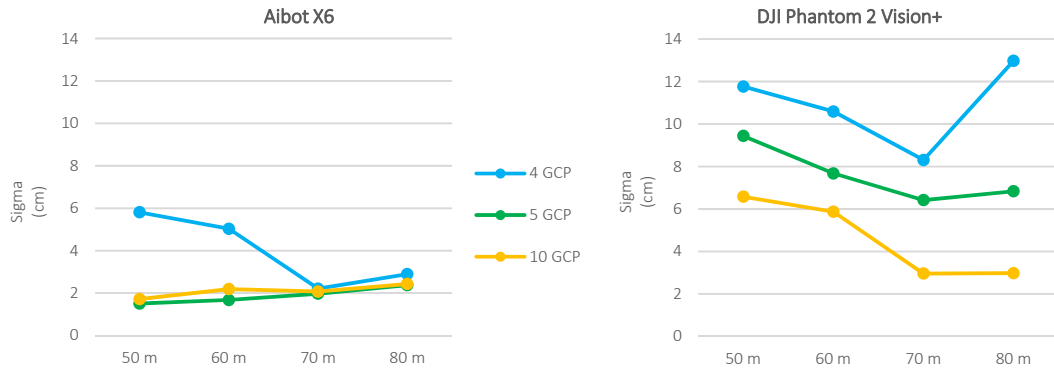


Figure 33. Impact of altitude on BBA accuracy

Although the flight altitude changes are likely to alter the Sigma of residuals in Aibot X6, these alterations are actually an adjustment over its GSD size at the respective flight heights. As shown in Figure 34, the accuracy error in 5-GCPs and 10-GCPs of the Aibot X6 are almost constant at every flight altitude if the resulting Sigma is normalised by its GSD size. This figure also confirms that with the Aibot X6, the addition of more than five GCPs will not evidently increase the resulting accuracy of the BBA.

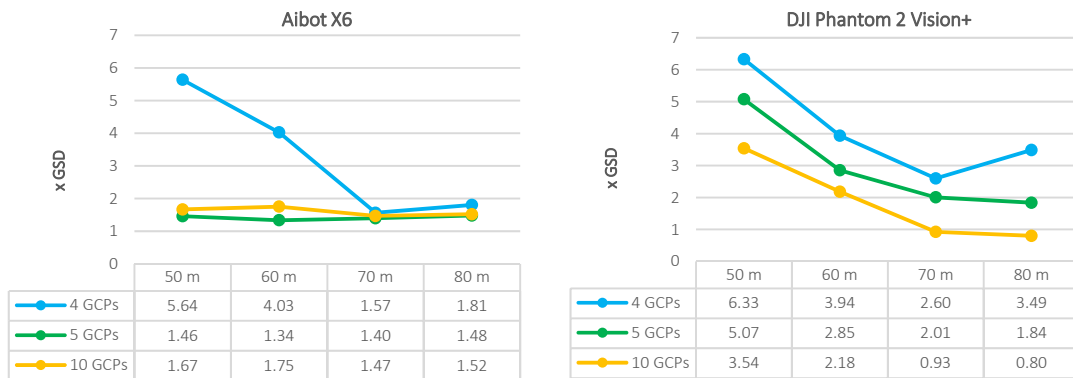


Figure 34. The resulting BBA accuracy from different flight altitudes with respect to GSD size

Whereas with DJI Phantom 2, the resulting accuracy normalised by the GSD size rises significantly with every altitude increment. The increase in the BBA accuracy is not only an adjustment for the size of GSD when the flight altitude is changed, but also reduces the deformation of the bundle block. With every 10-metre increment in flight altitude, the vertical accuracy on average increases 27% in the 5-GCP configuration and 40% in the 10-GCP configuration.

Apparently, the type of lens used during data collection could lead to different responses to the changes in flight altitude. In the case of a rectilinear lens, the resulting accuracy tends to stagnate against the altitude changes, as long as the systematic error has already been suppressed. In contrast, the barrel distortion from a curvilinear lens like in the DJI Phantom 2's camera seemingly remains at a lower flight altitude, even though the lens correction has already been applied. Based on the observation of the reprojection error of the checkpoints, the residuals of lens correction gradually decrease in parallel with the increasing flight altitude. Regardless, the camera of the DJI Phantom 2 is designed only for recreational purposes. Its lens is not as high quality with a strict manufacturing error tolerance as the Voigtländer lens used in the Aibot X6. The optimised camera parameter values in the DJI Phantom 2 are also never at a relatively stable value, even at the same flight altitude. The residual lens error from camera parameter optimisation also reveals that the camera in the DJI Phantom 2 has a larger average reprojection error (more than 1 pixel) than the Aibot X6 as shown in Figure 35. This large error margin will cause an imprecise result in the lens correction process.

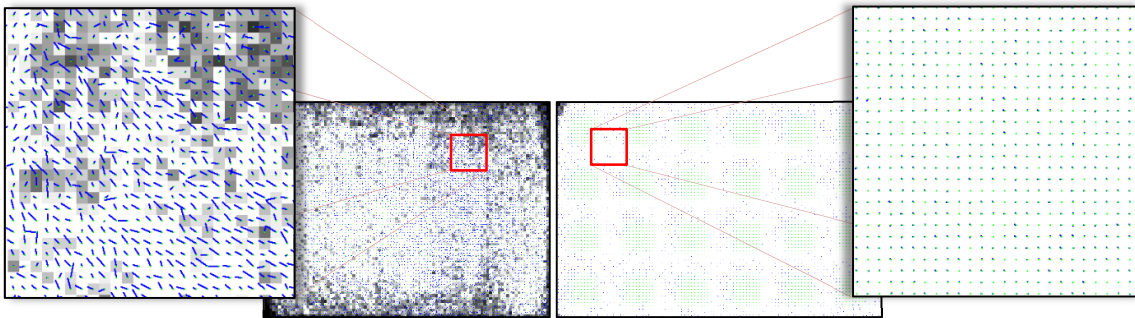


Figure 35. Average direction and magnitude of the reprojection error in DJI Phantom 2 camera (left) and Aibot X6 (right)

5.6.2. Main findings

- In terms of the residuals value, the residual error of the Aibot X6 tends to increase in parallel with the increase in flight altitude. In contrast, the residuals in the DJI Phantom will decrease with an increase in flying height.
- Concerning the ratio of error with its GSD, the increase in residuals of the Aibot X6 is an adjustment to the inevitable random error of the GSD size. The residual of the Aibot X6 is actually stagnant with respect to the increase in flying altitude. In the DJI Phantom 2, however, the ratio of residuals to its GSD increases with the increase in flight altitude.

5.7. Impact of Motion blur on the BBA accuracy

5.7.1. Experiment results

As mentioned above, without any control point the resulting accuracy from various degrees of motion blur could not be clearly analysed. By adding control points to the bundle block, the impact of motion blur on the resulting accuracy became visible. An experiment was conducted to examine the impact of motion blur gathered from different flight speed configurations of the Aibot X6 at 50 metres of flight height. The comparison was done by comparing the vertical error from the BBA process with the expected motion blur. Both values were normalised by the size of GSD to obtain a uniform unit value. Only two GCP configurations have been used in this comparison: 5-GCPs and 10-GCPs. Only these two configurations were chosen because in both configurations the systematic error is considered to be absent.

Because the bundle block from Flight-2 did not completely cover the whole study area, its resulting accuracy could not be used as a reference in justifying the impact of motion blur on the obtained accuracy. As the distribution of GCPs and checkpoints were not the same with the other bundle blocks, the bundle block of

Flight-2 eventually resulted in different levels of accuracy from the others. The impact of motion blur in the reduction of the resulting accuracy can be seen in the figure below.

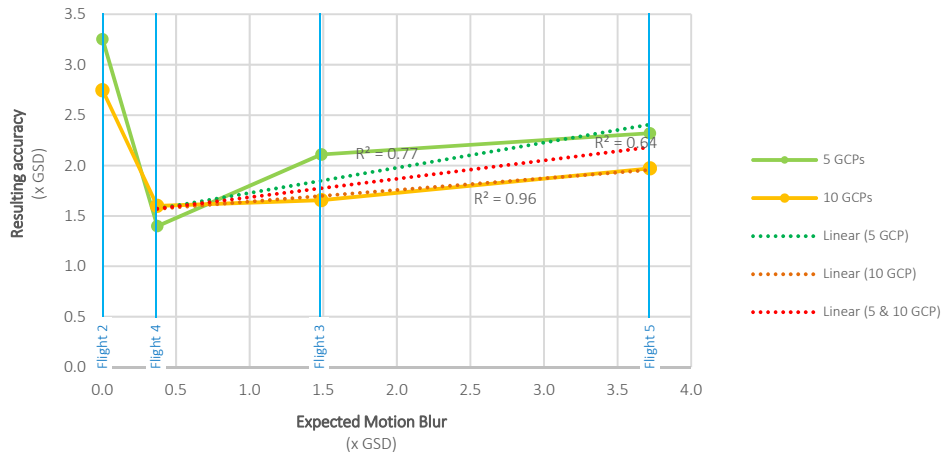


Figure 36. The effects of motion blur on the resulting accuracy

From the trend line of the resulting accuracy in 5-GCP and 10-GCP configurations, motion blur is evidently affecting the resulting accuracy. Both configurations have promising trend-lines with the fitted value up to 77% in the 5-GCP configuration (green dotted line) and even 96% in the 10-GCP configuration (orange dotted line). Moreover, by taking both configurations as individual values on the assumption that the systematic error already vanishes in the both configurations, the trend-line still has a fitted value of 64% (red dotted line). Furthermore, a higher number of GCPs proves to be beneficial in suppressing the impact of motion blur on the resulting accuracy, although the result will not be better than the bundle block with a lesser motion blur.

5.7.2. Main findings

- The increase in the degree of motion blur on the images can reduce the level of accuracy of a bundle block. The correlation between the two is linear.
- A higher number of GCPs can be used to suppress the impact of motion blur on resulting accuracy, although the result will not be better than the bundle block with a lesser motion blur.

5.8. Impact of cross flights and oblique images addition on the BBA accuracy

5.8.1. Experiment results

The resulting accuracy of bundle blocks with oblique view configurations and cross flight additions can be seen in Table 11. However, the oblique image configuration can only be applied to the Aibot X6 due to data availability, while the cross flight addition can be applied to all three UAVs. Figure 37 is intended to explain the resulting accuracy compared with GSD size. As a consequence of image addition from a different flight height, the GSD size will commonly abate due to compromising the GSD size from the higher altitude. The vertical error unit used in this figure is the Sigma divided by the GSD size to normalise the amount of vertical error.

The cross flight addition has a different influence on each UAV. Also, the cross flight addition does not have the same impact in all GCP scenarios. For the Aibot X6, the cross flight addition only increases the vertical accuracy in the 4-GCP and undistributed 5-GCP configurations; around 50% accuracy increases in both configurations. Furthermore, the addition of cross flight in the undistributed GCP also helps to

eliminate the systematic radial error that occurred in the single flight (Figure 37). Whilst in 5-GCP and 10-GCP configurations, the cross flight addition does not meaningfully increase the vertical accuracy; it even worsens the outcome in most scenarios.

Table 11. Residuals at checkpoints of cross flight and oblique image configurations

UAV	Flight Config.	Num. of GCP		σX (cm)	σY (cm)	σZ (cm)	
Aibot X6	Cross flight 50m & 70m	4	Sigma	1.30	1.68	2.80	
			RMSE	1.51	1.72	7.33	
		5	Sigma	1.12	1.16	2.13	
			RMSE	1.20	1.82	2.31	
		5 undist	Sigma	1.59	1.77	1.63	
			RMSE	1.59	1.79	1.66	
	10	Sigma	1.42	1.23	1.65		
		RMSE	1.42	1.39	1.73		
	Cross flight 60m & 80m	4	Sigma	1.18	1.10	2.25	
			RMSE	1.24	1.35	2.62	
		5	Sigma	1.21	1.12	2.31	
			RMSE	1.26	1.21	2.31	
5 undist		Sigma	2.03	1.95	2.07		
		RMSE	2.43	3.43	3.16		
10	Sigma	1.28	1.02	2.47			
	RMSE	1.29	1.50	2.47			
DJI Phantom 2 Vision+	Cross flight 50m & 70m	4	Sigma	5.69	4.19	15.78	
			RMSE	6.26	4.51	27.81	
		5	Sigma	5.71	4.30	14.61	
			RMSE	6.00	4.77	17.26	
		5 undist	Sigma	6.83	4.95	22.55	
			RMSE	7.87	6.18	30.92	
	10	Sigma	4.70	3.20	14.51		
		RMSE	5.17	4.10	15.71		
	DJI Phantom 2 Vision+	Cross flight 60m & 80m	4	Sigma	5.49	3.83	11.47
				RMSE	6.40	3.85	26.33
5			Sigma	5.33	3.74	8.54	
			RMSE	5.76	4.53	8.77	
5 undist			Sigma	5.43	3.56	18.03	
			RMSE	6.79	3.63	23.14	
10		Sigma	4.86	3.30	7.77		
		RMSE	4.91	3.50	7.92		
Ebee RTK		Cross flight 70m & 80m	4	Sigma	1.99	1.46	1.67
				RMSE	1.99	1.50	1.85
	5		Sigma	2.04	1.35	1.69	
			RMSE	2.04	1.46	1.80	
Aibot X6	Oblique images 50m 40° view	4	Sigma	1.40	1.36	2.46	
			RMSE	1.43	1.48	5.49	
		5	Sigma	1.30	1.41	1.62	
			RMSE	1.72	1.42	1.62	
		5 undist	Sigma	2.94	1.66	2.49	
			RMSE	3.60	2.70	2.79	
	10	Sigma	0.98	1.20	1.70		
		RMSE	1.10	1.33	1.83		
	Oblique + Nadir images 50m	4	Sigma	1.58	1.22	2.60	
			RMSE	1.59	1.45	6.23	
5		Sigma	1.53	1.30	1.57		
		RMSE	1.71	1.31	1.57		
5 undist		Sigma	2.84	2.21	2.44		
		RMSE	3.34	3.73	2.68		
10	Sigma	1.00	1.17	1.68			
	RMSE	1.05	1.34	1.85			

For the DJI Phantom 2, the addition of images from 70 metres to 50 metres flight altitude worsens the resulting accuracy in all GCP configurations, both in the absolute error of Sigma/RMSE value and in the ratio with the GSD size. Only the resulting accuracies of 4-GCP and 5-GCP configurations at 60 metres flight altitude of the DJI Phantom 2 increase; otherwise, accuracy decreases. However, it is only the resulting accuracy from the cross flight addition by the Ebee RTK that consistently increases in all GCP configurations. However, the increase was not significant due to the resulting accuracies in the single flight already being below one GSD.

The cross flights addition may improve the resulting accuracy of the single flight. However, the addition of cross strips apparently only succeeds in reducing the systematic error in block adjustments in 4-GCP and

undistributed 5-GCP configurations with the Aibot X6; only if the systematic error still occurs in the BBA. The cross flight addition also succeeds in suppressing the vertical distribution dependency on the 4-GCP configuration. However, it does not seem to be able to replace the GCP addition in reducing the deformation of the bundle block. In the case of a curvilinear lens, the cross flight addition will exaggerate the vertical error if the error from lens distortions is still present, as in the 50-metre flight height configuration of the DJI Phantom 2. Beyond these circumstances, the cross flight addition tends to aggravate the achievable accuracy from the single flight altitude because larger RMSE errors from the higher altitude were accumulated into the error at lower flight altitude.

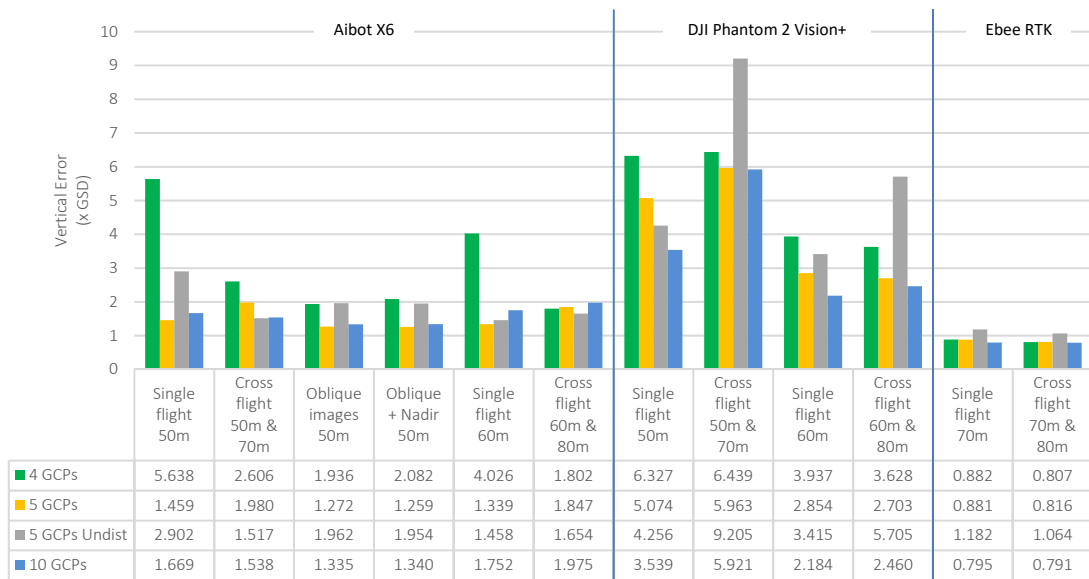


Figure 37. Impact of cross flights and oblique images addition to the resulting BBA accuracy

BBA from the oblique image has a more rigid bundle block than the bundle block from cross flight configuration. In all evenly distributed GCP configurations, the accuracy of the bundle block from the oblique image is greater than the accuracy of a single flight or cross flight configurations. Especially in a 4-GCP configuration, the accuracy of the oblique image configuration was 66% better than the single flight configuration and 26% better than the cross flight configuration. Although not as good as the cross flight configuration, the oblique image configuration also gives 32% better accuracy in the undistributed GCP configuration than the single flight. Unlike in the cross flight, the systematic radial error also occurs in the undistributed GCP configuration of oblique image. These improvements are easily understood because to create a single block of oblique image configuration requires four different directions of the angle of view – four times more images than the single flight configuration – providing more observations per tiepoint, and thus a more rigid bundle block. However, the addition of nadir images to the oblique image configuration did not have a proven impact on refining the resulting accuracy of the BBA.

The comparison of block deformation between the single flight, cross flight and oblique image configurations is depicted in Figure 38. The figure only illustrates the deformation in 4-GCP and undistributed 5-GCP configurations, because in these GCP configurations all three flight patterns have remarkable variations.

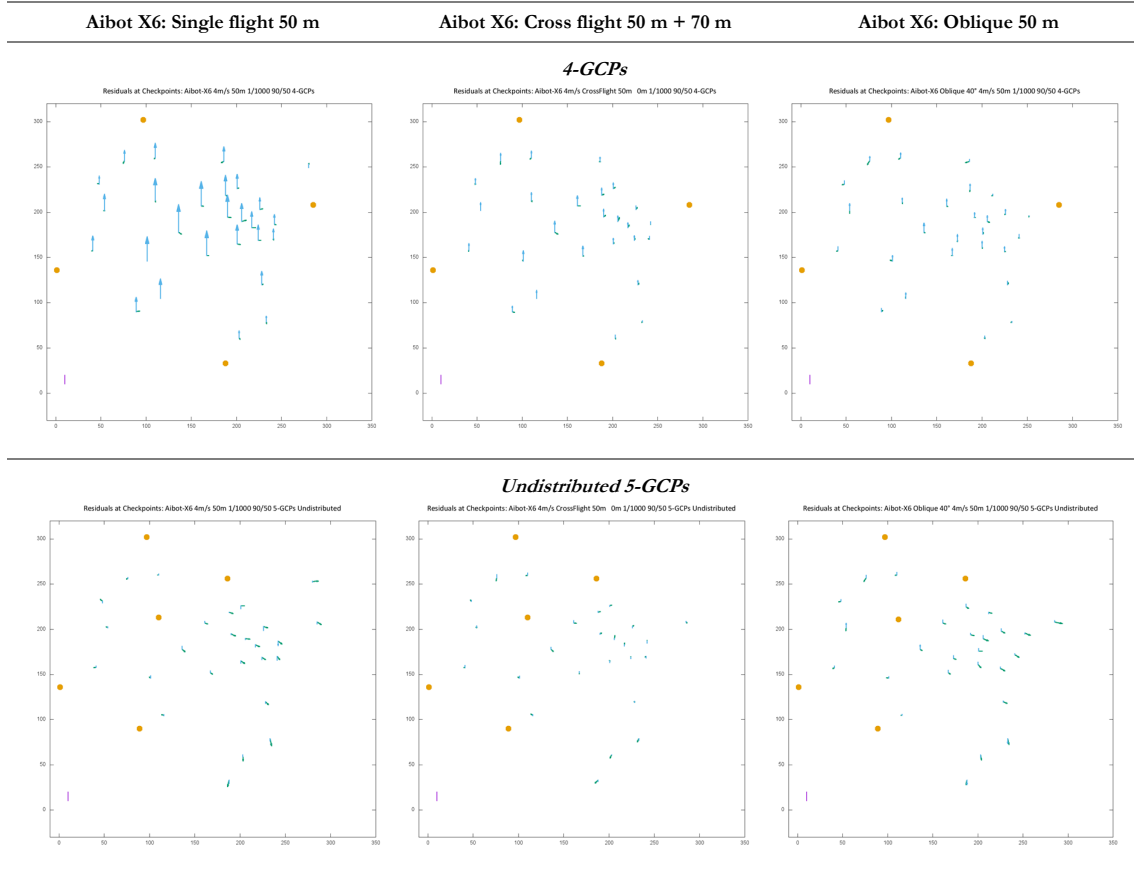


Figure 38. The comparison of block deformation of the single flight, cross flights addition and oblique image configuration in 4-GCPs and undistributed 5-GCPs

5.8.2. Main findings

- The addition of cross flights reduces the systematic error in bundle blocks that still have a systematic error in the block adjustment result as in the 4-GCP or the undistributed 5-GCP configurations. The cross flight addition also succeeds in suppressing the vertical distribution dependency on the 4-GCP configuration.
- The cross flights addition is not able to replace the GCP addition in reducing the deformation of the bundle block
- BBA from the oblique image has lower residuals at checkpoints than the bundle block from a cross flight configuration.
- The addition of nadir images to the oblique images configuration did not have a proven impact on refining the resulting accuracy of block adjustments.

5.9. Impact of flight overlaps on the BBA accuracy

5.9.1. Experiment results

At 50 metres flight altitude, the reduction of the forward overlap percentage of the Aibot X6 from 90% to 80% mainly affects the number of overlapping images in the pyramid part. The pyramid was covered with more than five overlapping images in 90% of forward overlap scenarios. While with the 80% forward overlap, some parts of the pyramid are covered only with two overlapping images. By reducing forward overlap further to 70%, these parts are only covered with one image, which becomes impractical for stereo

image analysis purposes. The number of overlapping images covering the study area in 80/50 percent overlap and 70/50 percent overlap of Aibot X6 can be seen in the figure below.

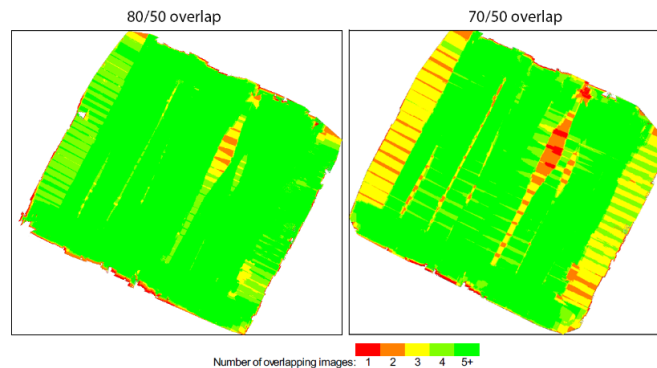


Figure 39. The number of overlapping images in 80/50 overlap and 70/50 overlap of Aibot X6

However, the low number of overlapping images in the pyramid area was not the case with the DJI Phantom 2. By taking advantage of an ultra-wide lens, the DJI Phantom 2 acquired good overlapping images with more than 5 images in the pyramid area in both 80/50 and 70/50 overlaps as shown in Figure 40. However, another problem arises in the 70/50 overlap; with the same GCP configuration as in 90/50 and 80/50 overlaps, the RMSE of the GCP in 70/50 more than doubles its GSD size due to the low number of images that can be marked.

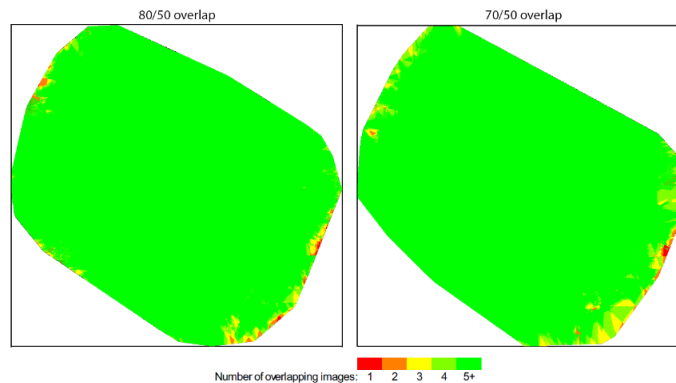


Figure 40. The number of overlapping images in 80/50 overlap and 70/50 overlap of DJI Phantom 2 Vision+

By eliminating the middle image between two consecutive images in the Ebee RTK image-set, another bundle block is obtained with the overlap percentage around 70/50. Although the Ebee RTK has a lower image overlap configuration compared with the other UAVs, an unordered pattern of the acquired images gives a distinct advantage in determining the number of overlapping images, as well as having a higher flight altitude comparing with the other UAVs tested above. However, its irregular pattern also shows its disadvantage, as the high number of overlapping images are only available in the middle of the study area. Unlike with the Aibot X6 and DJI Phantom 2, the available images to be overlapped are mostly two or three images with several areas covered with only one image in the near-border area. This feature will be a problem if the UAV records the study area without any buffer zone added from the boundary of the study area.

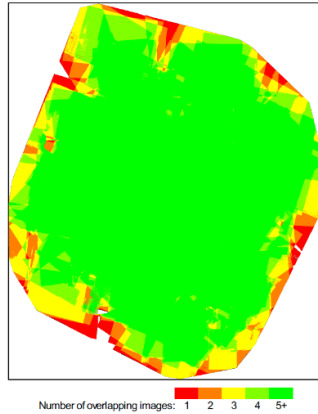


Figure 41. The number of overlapping images in 70/40 overlap configuration of Ebee RTK

By applying various GCP configurations to the bundle block, the number of overlapping images demonstrates an influence on the resulting accuracy. The 80/50 percent image overlap inevitably worsens the results compared with the 90/50 percent image overlap in all GCP configurations on both single flight and cross flight patterns of the Aibot X6. The Ebee RTK also showed a similar phenomenon. However, its influence on the DJI Phantom 2 varied. Compared with the 90/50 image overlap, the image overlap reduction surprisingly improves the resulting accuracy in the single flight 50-metre altitude and the cross flight of 50 and 70 metre altitudes. However, the resulting accuracy of 80/50 percent overlap is worse than the 90/50 percent overlap at 70 metres flight altitude. This behaviour is seemingly caused by the remaining image distortion with the DJI Phantom 2. At 50 metres flight altitude, the positional ambiguity due to remaining distortion actually decreased by reducing the number of overlapping images, contrarily resulting in a higher accuracy.

Figure 42 represents the comparison of the resulting accuracy between 90/50 and 80/50 image overlap with the Aibot X6 and DJI Phantom 2, and the accuracy of 70/50 overlap in selected scenarios. The 70/50 image overlap scenario could not be done in all configurations due to the image overlap issue in the pyramid area. The accuracy that is used in this figure is from the Sigma value normalised by the GSD size.

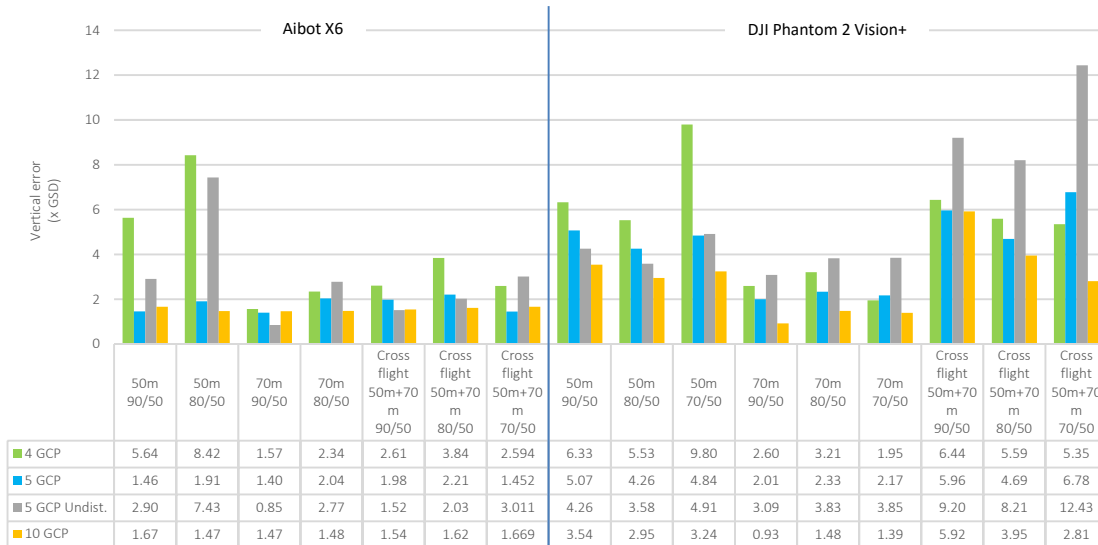


Figure 42. The comparison of resulting accuracies from 90/50, 80/50 and 70/50 percent image overlaps

In a single flight configuration of the Aibot X6, 10% forward overlap reductions mainly affected the unevenly distributed GCP configurations, with up to 200% accuracy decrements. In a well-distributed GCP configuration, the impact of overlap reductions is gradually reduced by the increase of GCP addition, with accuracy decrements of around 50% in 4-GCPs, 35% in 5-GCPs, while in 10-GCPs the overlap reduction does not significantly affect the resulting accuracy. However, this impact is highly reduced in cross flight configurations. The accuracy decrement in an unevenly distributed GCP becomes only 35% in the cross flight configuration. Although the accuracy decrement is still high in 4-GCPs of cross flight configuration, the decrement became only 10% in a 5-GCP configuration.

In the case of rectilinear lenses, the number of GCPs will apparently diminish the deformation created by overlap reduction. The cross flight addition also has the benefit of suppressing the accuracy decrement in a lower image overlap of a single altitude flight pattern, although its resulting accuracy will not be better than the resulting accuracy from a highly overlapped images bundle block.

The overlap reduction, however, is impacted differently with the DJI Phantom 2. Instead, the image overlap reduction will improve the resulting accuracy as long as the average of the reprojection errors is still high. The cross flights addition is also unable to suppress the decrease in accuracy caused by the overlap reduction; it even worsens the accuracy compared with single strip flights.

With the Ebee RTK, the overlap reduction from 85/75 to 70/50 percent will decrease the accuracy around 70% to 90% for all GCP configurations in both single-altitude and cross flights, with the lowest decrease in a 10-GCP configuration. As mentioned before, since the number of GCPs did not significantly affect the resulting accuracy of the Ebee RTK, the overlap reduction will tend to increase the deformation evenly in all GCP configurations. The cross flight addition with the Ebee RTK also does not demonstrate a significant impression in maintaining the achievable accuracy of the higher image overlaps.

The interesting point with the Ebee RTK is that the UAV has an RTK solution that can ensure each image collected has an accurate initial position. Even when image overlap in the Ebee RTK has been reduced, the resulting accuracy is still around 1.5 GSD size in all GCP configurations. This means the accuracy has already decreased by almost double the accuracy in 85/75 overlaps, experiencing the worst decrement in accuracy compared with the other UAVs. To further examine the influence of the initial position in comparison with the number overlap, the resulting accuracy from an RTK enabled bundle block is also compared with the resulting accuracy from the Ebee RTK without RTK solution from Flight-18 and the Aibot X6 in the same image overlap configuration as seen in Figure 43.

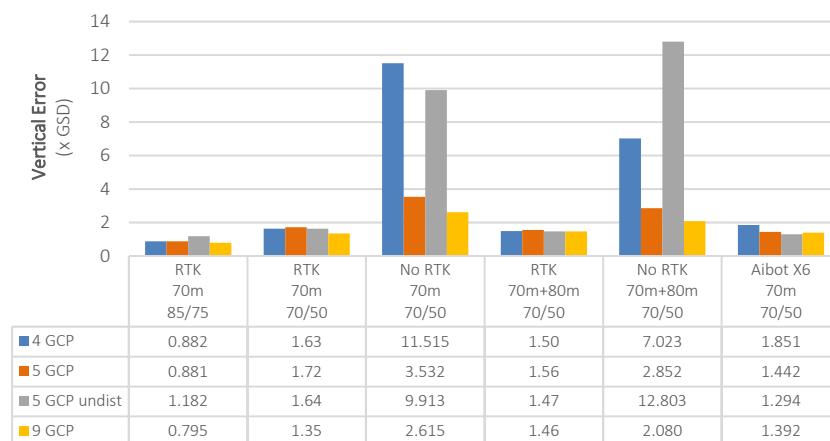


Figure 43. The resulting accuracy of Ebee RTK in 70/50 image overlaps

It is clear that initial position is the main parameter in suppressing the deformation of the bundle block. In the same image overlap configuration, the resulting accuracy of the Ebee with RTK solution is unmatched by the Ebee without RTK solution. Even compared with the Aibot X6, the resulting accuracy of the Ebee without RTK solution is still lower. However, a higher degree of motion blur also contributes to lowering the resulting accuracy of the Ebee RTK. As mentioned above, the degree of linear motion blur with the Ebee RTK is around 4.5 GSD size, while with the Aibot X6 it is only 0.5 GSD size.

5.9.2. Main findings

- Reducing the percentage of forward overlap in the Aibot X6 and Ebee RTK inevitably exacerbates the resulting achievable accuracy of the bundle block with a higher forward overlap. However, the addition of GCPs will apparently suppress the residuals increment produced by overlap reduction.
- In the case of the DJI Phantom 2, the reduction of forward overlap could improve the resulting accuracy as long as the average of the reprojection errors is still high. The cross flights addition could not suppress the decrease in accuracy caused by the overlap reduction; it even worsens the accuracy compared with single strip flights.
- A precise initial position accuracy is not the sole determinative factor in a good accuracy result. With a low image overlap and high motion blur, the accuracy achieved can be rivalled by the UAV with a common code-phase GPS in the same low percentage of image overlaps, as long as it does not have excessive motion blur.

5.10. The influence of land surfaces on the accuracy of the resulting DEM

5.10.1. Experiment results

After ensuring there is no significant systematic error remaining in the bundle block, several bundle blocks were selected for further processing. Two types of tests have been done to see the impact of land surfaces on the accuracy of the derived point cloud. First, the dense point clouds have been cut in the same sampling area to see the impact of UAV flight parameters and surface types on the resulting dense point cloud. Secondly, a test was conducted by comparing the dense point clouds with 261 points of 3D reference heights scattered throughout the study area.

The first test was conducted with two different steps; the first step involves comparing a dense point cloud of a rigid surface with its own 2.5D quadratic mesh. The sampling area selected is a paving setts surface. This kind of surface has been chosen because it has a stable form and pattern from day to day, making it an ideal object on which to perform a comparison analysis with the point clouds that were recorded on different days. Moreover, Flight-4 of Aibot X6 recorded underexposed images in this part, which can be used to justify the impact of underexposed images on its generated point cloud. Also, this paving setts area is also covered by Flight-2, which is useful as a “reference” point cloud as it has balanced illumination lights yet has no expected motion blur. However, the derived dense point clouds in this analysis were only selected from the Aibot X6 to ensure there are no different sensor quality parameters involved in this test.

The resulting Sigma of the measurement and the signed distance of point clouds can be seen in Figure 44. The cropped point clouds have been coloured with a gradation of red to white to blue. White colour indicates the best points fitted to its plane while red coloured means the distance is more than twice of its standard deviation in positive direction (above the average plane) and blue coloured in negative direction (below the average plane).

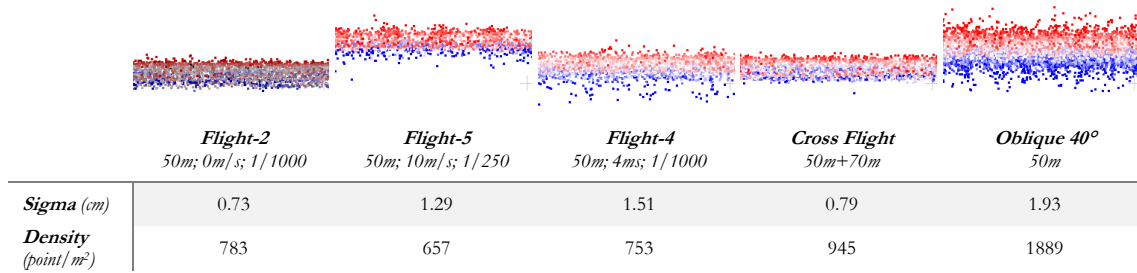


Figure 44. The resulting Sigma of dense point cloud compared with its fitting plane

From the calculation of generated dense point clouds of Flight-2, Flight-4, and Flight-5, it can be inferred that 1-stop underexposed images to some extent do not have a significant impact in reducing the number of point clouds generated, as the point density of Flight-4 is not significantly different to the point density of Flight-2. Meanwhile, the motion blur has the effect of reducing the density of point cloud as shown in Flight-5 and tends to increase the sigma as shown in Flight-4 and Flight-5. The impact of motion blur can also be justified from the number of matching points extracted. The number of matched points in Flight-5 is lower than Flight-2, even though Flight-2 only recorded two-thirds of the entire study area.

The second step is basically using the same approach as the first test, only now extending the test to different types of surface and involving dense point clouds from all UAVs. From the measurements involving point clouds from all UAVs of three different surfaces, the cross flights and oblique image configurations convincingly produce a denser point cloud compared with single strip configurations, as more images are available to be used in the similarity calculation between overlapping images (Table 12). However, the Sigma will be prone to increase especially in the bundle block that has large residuals lens correction in the images, as any similarity that is recorded in at least three images can be used to produce one point in the point cloud.

Table 12. The measurement result of densified point clouds compared with its 2.5D Quadratic plane

UAV	Configuration	<i>Paving Setts</i>		<i>Bare Soil</i>		<i>Grass</i>	
		Density (Points/m ²)	Sigma (cm)	Density (Points/m ²)	Sigma (cm)	Density (Points/m ²)	Sigma (cm)
Albot X6	Flight-2 50m; 1m/s; 1/1000	783	0.73	969	1.02	1,145	2.34
	Flight-4 50m; 4m/s; 1/1000	753	1.51	1,156	1.21	1,430	3.12
	Flight-5 50m; 10m/s; 1/250	657	1.29	719	1.06	924	2.30
	Cross Flights 50m + 70m; 4m/s; 1/1000	945	0.79	1,860	1.45	2,016	3.41
	Cross Flights 60m + 80m; 4m/s; 1/1000	951	1.36	1,371	1.62	1,547	3.04
	Oblique 40° 50m; 4m/s; 1/1000	1889	1.93	1,551	1.91	2,747	3.05
DJI Phantom 2	Flight-16 80m; 3m/s; 1/200	196	3.48	300	4.24	297	4.43
	Cross Flights 50m + 70m; 3m/s; 1/200	697	4.75	1,370	4.50	658	5.31
Ebee RTK	Flight-17 70m; 12m/s; 1/125	386	2.20	342	3.27	370	3.51
	Cross Flights 70m + 80m; 12m/s; 1/125	382	3.80	386	4.73	507	3.81

The surface type also has an influence on the resulting accuracy of the point cloud. A densification process is likely to generate a point cloud with a different level of accuracy, depending on the surface type. A solid surface with a clear pattern such as paving setts tend to have a lower sigma than a non-rigid surface like grasses, as the tie point that is detected in one image can easily be grouped with the tie point from another image, reducing vertical bias and eventually resulting in an accurate point. Figure 45 shows how different type of surfaces can lead to differences in the number of tie points that can be detected in 10 images or more. Although the number of tie points is not the reason for the difference in the quality of dense point clouds, this figure shows how finding the similarity of the corresponding point in grasses is more difficult than in paving setts.

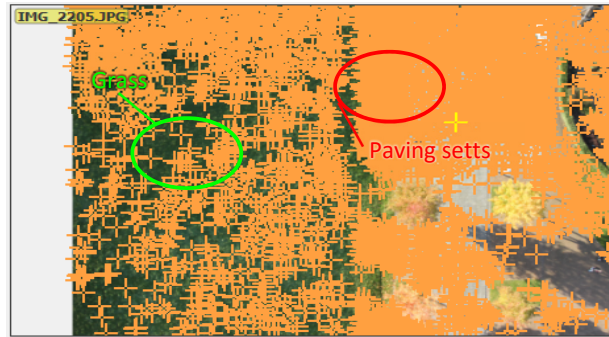


Figure 45. Number of automatic tie points produced on paving setts and grasses

However, the test above does not indicate the actual accuracy of the densified point cloud to the real world form. As shown in Figure 44, although the derived point clouds do not have much difference in Sigma from one to another, these point clouds are not located at the same height. To find out the actual accuracy of the densified point cloud, measurements involving derived dense point clouds from selected flight configurations and 3D reference heights were taken. This method calculates the distance from each point on the reference point to the 10 nearest points on the dense point cloud by employing an Approximate Nearest Neighbour (ANN) Searching library (Mount & Arya, 2010). There are two different methods used to find the nearest neighbour points: searching within radius one metre from a reference point in XY position (2D), and searching within radius one metre from a reference point in XYZ position (3D sphere). Both methods give a maximum of 10 points of dense point cloud within the respective search range. The result is shown in Table 13.

As a comparison, the results of the 3D-search method have been compared with the results from the distance measurement of 3D reference heights with the 2.D surface mesh of the point cloud. The method used to create the surface is the 2.5D Delaunay triangulation algorithm. The result of the comparison indicates that the accuracy result from the 3D-search method is only about 15% lower than the accuracy results from the surface representation measurement. Hence, the 3D-search results can be used as an estimation of the accuracy of the 2.5D surface representation product.

From Table 13, it is confirmed that a bundle block with blurred images will produce a less accurate dense point cloud. Using a 3D-search method, the Aibot X6 Flight-5 has a larger error compared with other Aibot X6 flight configurations, as well as the Ebee RTK. However, the error in both configurations of the Ebee RTK did not experience an increase as high as the other configurations when switched to a 2D-search method. The cross flights and oblique image configurations provided a lower error value than single flight configurations. The 3D-search results also demonstrate that within certain conditions, there are no significant differences in terms of absolute error on the dense point cloud derived from all UAVs. However, in term of accuracy error in relation to GSD size, dense point clouds from the DJI Phantom 2 have a smaller error compared with the others.

Table 13. The results of the nearest neighbour search

UAV	Flight Configuration	3D-search				2D-search				
		Mean (cm)	Sigma (cm)	RMSE cm	RMSE GSD normalised	Median (cm)	Mean (cm)	Sigma (cm)	RMSE cm	RMSE GSD normalised
Aibot X6	Flight-4 50m; 4m/s; 1/1000	2.32	3.31	4.04	3.93	2.60	1.57	13.50	13.59	13.19
	Flight-5 50m; 10m/s; 1/250	3.66	3.31	4.94	4.75	4.30	4.88	14.73	15.52	14.93
	Cross Flights 50m + 70m; 4m/s; 1/1000	1.62	3.14	3.54	3.29	2.90	3.12	14.68	15.00	13.96
	Cross Flights 60m + 80m; 4m/s; 1/1000	2.43	2.94	3.81	3.05	3.20	3.07	14.32	14.64	11.71
	Oblique 40° 50m; 4m/s; 1/1000	2.02	2.07	2.89	2.27	3.10	1.84	14.56	14.68	11.56
DJI Phantom 2	Flight-16 80m; 3m/s; 1/200	0.82	4.79	4.85	1.31	0.40	1.68	16.41	16.50	4.44
	Cross Flights 50m + 70m; 3m/s; 1/200	0.39	3.27	3.29	1.34	1.20	3.19	26.14	26.33	10.75
Ebee RTK	Flight-17 70m; 12m/s; 1/125	3.85	3.63	5.29	2.61	4.30	4.73	9.39	10.52	5.18
	Cross Flights 70m + 80m; 12m/s; 1/125	3.44	3.58	4.97	2.40	4.80	4.09	10.43	11.20	5.41

The 2D-search method tends to deliver an exaggerated value, as this method does not restrict the search point in the Z direction. To examine the tendency for error in each reference point, Figure 46 shows the residuals at 3D reference heights from all derived dense point clouds. A positive value means the average distance of dense point cloud is higher than the 3D reference points and the negative value is vice versa. The distribution shown in the figure is not based on the positions, but on the number of 3D reference heights.

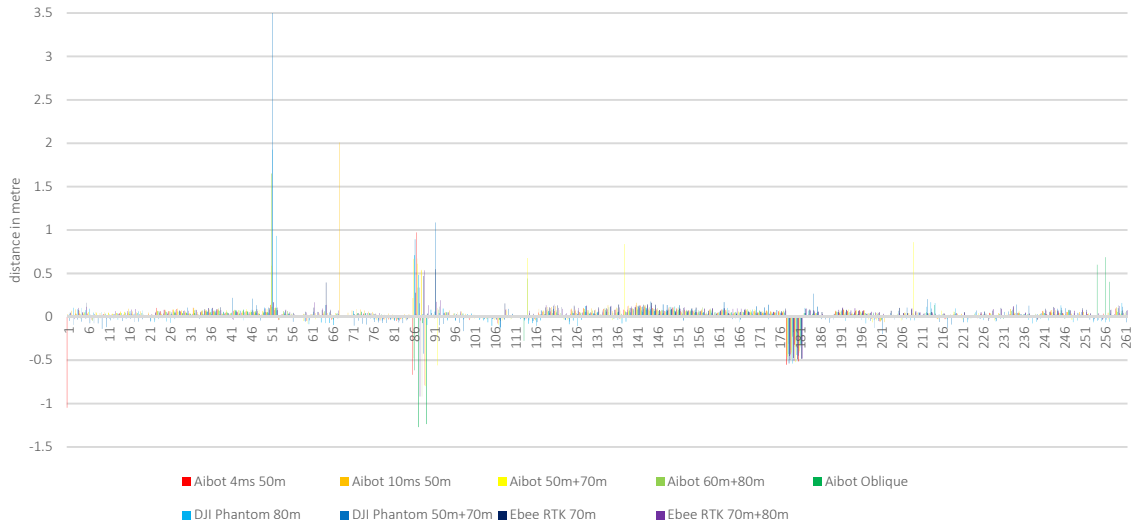


Figure 46. The residuals at checkpoints of dense point clouds obtained with 2D-search method

From Figure 46, it appears that the reference heights in the range 86-89 and the range 178-181 have the same trend of error on all dense point clouds. To emphasise the observation for both ranges, they are presented on a separate chart as shown in Figure 47. This figure shows that both ranges have distinct

differences; each dense point cloud responds differently in the range 86-89 whereas in the range 178-181 all the dense point clouds respond in the same direction.

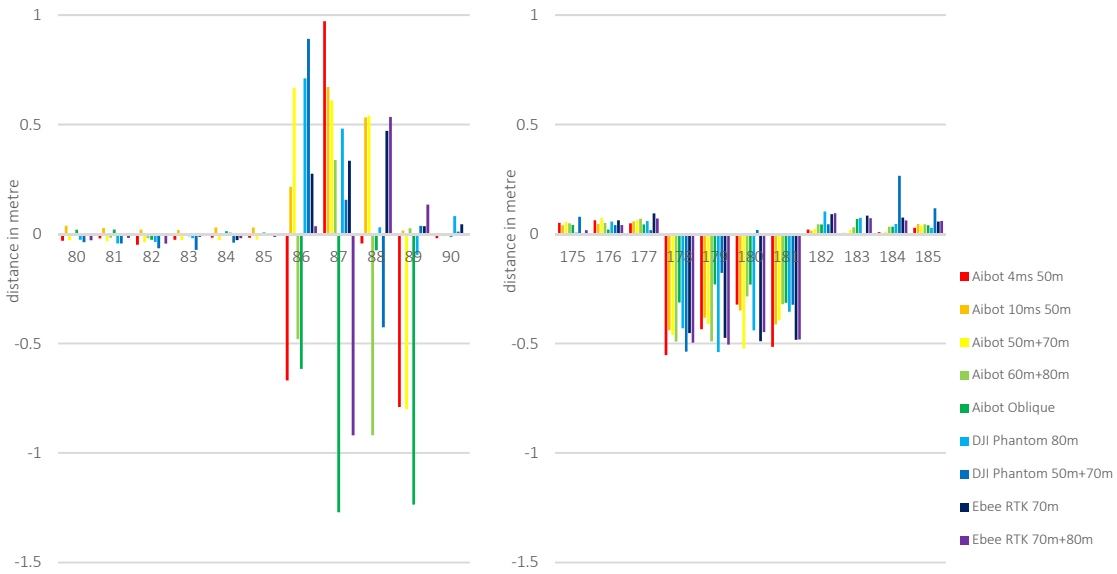


Figure 47. Residuals at checkpoints in the range of 80 to 90 and 175 to 185 of the 3D reference heights

By taking the checkpoint residuals from the DJI Phantom 2 Flight-16 as an example, Figure 48 shows the location of the residuals in both ranges. The figure shows that the position of checkpoints in the range 86-90 is on the bridge while the range 178-181 is on the top edge of the steel box on the top of the pyramid. Apart from these ranges, particularly in Flight-16 of DJI Phantom 2 as shown in Figure 46, there are other large residuals in the range 51-53 (shown by the blue bar in Figure 46). Large errors in these points are caused by strong shadow; which is a unique occurrence, resulting in a sparser point cloud in the concerned segment.

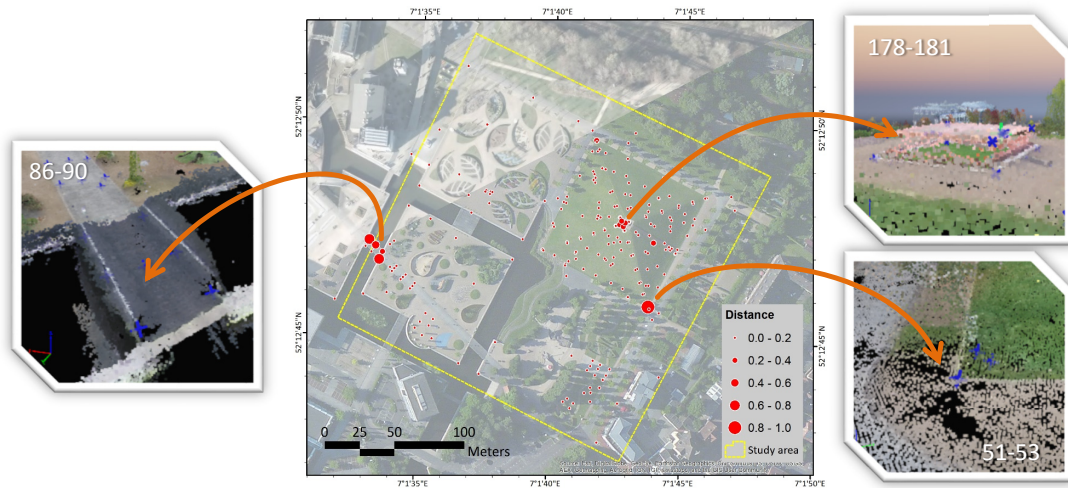


Figure 48. The distance measurement error in 2D search method

On a flat surface, wherein most of the 3D reference heights are located, the 2D-search method delivers relatively the same distance as the 3D-search method, as shown by the Median of the 2D-search which does

not differ very much from the Mean in the 3D-search. The large error in the edge of the steel box on the top of the pyramid is caused by a sudden feature change with a lack of texture differences between the top and the side of the box because the object is recorded as overexposed compared with the surroundings. All configurations tend to have a larger error in this spot; only the Aibot X6 with an oblique view configuration has smaller residuals. The large residuals in the 3D reference heights located on the bridge are likely caused by the shadow of the bridge that is reflected on the water, which also creates erroneous point clouds around the bridge. Moreover, large time differences for image acquisition from one viewpoint to another causes different shadow lengths that will eventually create matched points with wrong positions. Further, in the area with strong shadows, the densification process failed to find corresponding points in the shadow area due to lack of texture and eventually generated an area with a less dense point cloud.

5.10.2. Main findings

- 1-stop of underexposed images did not significantly affect the reduction in the density of point clouds generated. In contrast, the motion blur has an impact in reducing the density of a point cloud and tends to increase the sigma.
- The surface type has an influence on the resulting accuracy of the point cloud. A solid surface with a clear pattern such as paving sett tends to have a lower sigma than non-rigid surfaces like grasses.
- Sudden feature changes, a reflection of shadows on the water, and high contrast shadows are prone to creating erroneous points in the dense image matching process.
- Nevertheless, there are no big differences in the resulting accuracy of the dense point cloud derived from all UAVs. However, in terms of the resulting error compared with pixel size, the dense point clouds derived from the DJI Phantom 2 have better accuracy results than the others.

6. DISCUSSION

From the research results, it is clear that the GRD size depends on the configuration of the UAV during data acquisition. However, only the GRD value from the DJI Phantom 2 can achieve the same value as its GSD, as an on-board image sharpening process on the DJI Phantom 2 camera has eliminated most of the motion blur effects on the image. None of the GRD sizes with all predefined conditions with the Aibot X6 were equal to the theoretical GSD size, even in the stop-mode configuration in which no expected motion blur was added. This is understandable as the GSD value used in the calculation is based on ideal conditions for the photogrammetric process, as it assumes no external interference with the process, while the GRD size is calculated based on the actual response of the sensor to the object. Every matter that lies between the sensor and the object could be a variable that affects the outcome. GRD value is affected by the lens aperture, motion blur and distance between the sensors and their target. A large opening aperture will tend to decrease the GRD, as lens diffraction starts to be considered. A higher degree of motion blur also will reduce the ability of the sensor to resolve the smaller object. Meanwhile, the distance between the sensors and the object will act as a counterweight to the motion blur impact; the farther the distance, the more the impact of motion blur will be reduced. However, there is one other thing that must be considered regarding distance increments: it needs a larger Koren Chart or Siemens Star to be placed in the study area. Otherwise, the calculation will fail to be implemented because even the largest line pairs in the chart could not be resolved, delivering a zero pulse of the spatial frequency.

The theoretical vertical accuracy is computed based on the ideal condition of multi-view stereo images, which means the result will be highly affected by the distance between the object and the images (flight altitude) and also the distance between two stereo images (baseline). In this case, the vertical error will increase with the increase of the flight altitude, while in the case of baseline, the farther the baseline, the lower the vertical error. In spite of the fact that the actual accuracy also involves multi-view stereo images, the resulting actual achievable accuracy was affected by more parameters than the geometrical relation parameters. As a result, the influencing parameters will produce a fluctuating achievable accuracy. In most scenarios, the actual achievable accuracy is worse than the theoretical vertical accuracy.

In the block adjustment process, initial image positions and the number and distribution of ground control points are the most influential parameters in determining the accuracy of the UAV photogrammetry-derived product, albeit the two are not solely independent. An accurate initial position can significantly improve the accuracy of the output of a block adjustment without control points. The resulting accuracy of a bundle block with RTK-based georeferenced images is up to six times more accurate than a bundle block that utilises georeferenced images from code-phase GPS. An accurate initial position gives a better approximation of exterior orientation parameters in the bundle block adjustment.

The adequacy of the number of GCPs depends on the remaining errors of the lens calibration process. UAV-based photogrammetry mostly employs a non-metric camera that is not precisely designed for measurement purposes. As the result, the camera calibration process during aerial triangulation does not necessarily ensure an accurate correction. Meanwhile, any remaining residuals from the lens correction process could increase the error of bundle block adjustments. In the images collected from the DJI Phantom 2, the reprojection error at some checkpoints is still above one pixel. This reprojection error declines with the increase in flying altitude of the UAV. Accordingly, the resulting accuracy of the DJI Phantom 2 increases with increasing flight altitude.

Based on the experiments, in a bundle block employing images collected using rectilinear lenses, five well-distributed GCPs are generally sufficient to get a BBA with a good positional accuracy. The use of 10 GCPs on the BBA is not proven to offer a significant improvement in the accuracy. Whereas, in the case of a

bundle block utilising images composed from curvilinear lenses – recreational ultra-wide cameras, explicitly – the use of 10 GCPs provides a better resulting accuracy than five GCPs.

The distribution of GCPs, both horizontally and vertically, also has an impact on the accuracy refinement. Horizontally undistributed GCPs will systematically increase the error of the bundle block especially in areas far from the GCP. However, despite already having been distributed horizontally, the achievable accuracy of the BBA could be increased. If there is a surface feature with a height ratio of more than 20% of the UAV flight altitude, placing one control point on the top of the feature will increase the achievable accuracy, especially in the 4-GCP configuration. Yet, the scenario will produce the opposite in the lower height ratio; GCPs distributed horizontally across the study area will give better accuracies than placing a control point on the top of land features. Nevertheless, the distribution of GCPs does not significantly affect the BBA accuracy with an accurate image initial position such as the Ebee RTK. Eventually, a sufficient number and good distribution of GCPs can also produce a BBA with an accuracy nearly equal to the BBA with an accurate image position. Although, the sufficient number and distribution of GCPs need a BBA with a lower degree of motion blur in the image to be able to work well.

Flight altitude does not actually affect the achievable accuracy of the bundle block adjustment if there are no significant residuals of lens correction remaining. In spite of the Sigma and RMSE obtained by the Aibot X6 tending to decrease in response to the altitude increment, the decrement is likely the way for the bundle block to adjust the inevitable random error involving the GSD size at respective flight altitudes. In the DJI Phantom 2 cases, conversely, flight altitude increments will tend to improve the accuracy generated. After all, only the results from the DJI Phantom 2 confirm the findings of Tahar (2015) that the resulting accuracy tends to increase when the flight altitude increases.

The use of motion-blurred images in the bundle block will ultimately decrease the achievable accuracy, not only affecting the sparse point cloud product but also the densified point cloud product. Based on the result, it can be inferred that the impact of motion blur on the resulting accuracy of the Aibot X6 is in every single GSD addition of expected motion blur to the image, the resulting accuracy dropped down to 37% in the 5-GCP configuration and 10% in the 10-GCP configuration. The decrement of the accuracy, albeit it can be suppressed by adding more GCPs, will not be significantly reduced as good as the accuracy obtained from the bundle block utilising images without motion blur disturbance.

The motion-blurred images will affect the photogrammetry process by reducing the number of features that can be used in the key point matching process, and eventually will produce a less dense point cloud product with a higher positional error. Notwithstanding, taking images in a stop mode to ensure there is no blur assembled to the image was not proven to be the best method of image acquisition. A stop mode acquisition can ensure the best quality image is obtained, although this method requires an extremely time-consuming process yet shorter battery life. These costs at a certain point will not be reciprocal to the increment of the achievable accuracy. By combining a bundle block from a cruising mode acquisition with a sufficient number of GCPs and additional cross strips, the resulting accuracy can rival the achievable accuracy of the stop mode acquisition derived product, as long as the motion blur gathered does not exceed the GSD size. An accurate image initial position also seems to be beneficial in suppressing the deformation, as the resulting accuracy of the BBA from the Ebee RTK with an RTK solution is much better than without an RTK solution.

To increase the rigidity of the bundle block adjustment, an additional strip consisting of images from different flight altitudes and perpendicular to the direction of the main strip can be taken into consideration. This method significantly reduces the deformation of the bundle block in conditions where only a few GCPs can be used or the GCP cannot be properly distributed, less than five GCPs based on the experiment. The addition of cross strips is also able to suppress the vertical distribution influence on the 4-GCP configuration at a lower flight altitude. However, the additional cross flights method is not recommended particularly when the bundle block already has a sufficient number of GCPs. The cross flight addition to the bundle

block will eventually also add the error from the involved flight altitudes to the main block. The other way to gain bundle block rigidity is by taking images obliquely. However, this method requires more effort by taking images of the object from four different angles. Oblique images will produce a solid bundle block without substantial vertical error differences even if only a few GCPs or undistributed GCPs are available. A combination of nadir and oblique images in a bundle block does not provide any benefit except to aggravate the data processing time.

Increasing the baseline distance by reducing the percentage of forward overlap will contrarily decrease the achievable accuracy as fewer observations can be used by tiepoints during AAT and BBA. However, the reduction of the BBA accuracy can actually be suppressed by adding more GCPs to the bundle block or by a cross strips addition, although its accuracy will not be as high as a highly overlapped images bundle block. Nevertheless, this kind of compensation can be heavily exploited to speed up the processing time when dealing with a bundle block with numerous images yet abundant control points.

In the densification process, surface type affects the quality of the output. A rigid and textured surface such as paving setts has a lower sigma compared with a non-rigid surface such as grasses. Highly blurred images also have an impact in increasing the error as well as reducing the number of points generated. Moreover, several features detected in the study area such as sudden feature changes, a reflection of shadows on the water, and high contrast shadows likely create inaccurate point clouds in the dense image matching process.

Above all, there are no significant differences in the dense image matching product's accuracy from a variety of UAV configurations selected. Nevertheless, in terms of accuracy to GSD size ratio, the dense point cloud derived from the DJI Phantom 2 has the best accuracy result, as the configuration used in this test was the highest-flying altitude of the DJI Phantom 2; thus having a bigger GSD size compared with the others.

7. CONCLUSION AND RECOMMENDATION

7.1. Conclusion

The aim of this study is to improve understanding of the influence of different parameters in the chain process of deriving the product of UAV-based photogrammetry. The conclusions that can be drawn from the findings are as follows:

- a. *How does the theoretical Ground Sampling Distance (GSD) compare to the actual Ground Resolved Distance (GRD)?*
The theoretical GSD is defined based on the assumption of ideal values for the equipment parameters, photogrammetric process, and geometrical relations. The GSD value is only affected by the sensor's pixel size and the image scale, whereas GRD is not merely affected by these parameters, but also by other aspects that lie between the sensor and the object, such as lens quality, lens aperture being used, and image blurriness. GRD is calculated based on the actual capability of the sensor to resolve the smallest object in the world to be presented in the images. Under the circumstances of the predefined UAV configurations, it is only the GRD resulting from the DJI Phantom 2 that can achieve the same value as its GSD.
- b. *How does the theoretical vertical accuracy compare to the actual achievable accuracy?*
Despite both theoretical and actual accuracies involving multi-view stereo images, the actual achievable accuracy was affected by more parameters than the theoretical vertical accuracy, which eventually results in a more fluctuating accuracy. Further, the theoretical vertical accuracy is merely computed based on the ideal condition of the multi-view stereo images process. In most scenarios, the actual achievable accuracy is lower than the theoretical vertical accuracy.
- c. *What is the influence of the image initial position on the resulting accuracy?*
The greatest benefit of having an accurate georeferenced image is in a BBA process without control points, as it gives a better exterior parameter approximation during the block adjustment process. An accurate image initial position can also suppress the deformation in a bundle block with a few GCPs or undistributed GCPs conditions, as well as in a bundle block with highly blurred images.
- d. *How can different Ground Control Point scenarios affect the overall accuracy?*
The accuracy of the block adjustment process is highly dependent on the sufficiency of control points and their distribution. The adequacy of the number of GCPs depends in any case on the remaining errors of the lens calibration process. Meanwhile, the distribution of GCPs also has an influence on the accuracy refinement, both horizontal and vertical distributions.
- e. *How do the different flight altitudes affect the resulting accuracy?*
Flight altitude changes do not affect the achievable accuracy of the bundle block in terms of the error to GSD size ratio, as long as no significant lens correction residuals remain. Further, in terms of the resulting Sigma and RMSE, the accuracy tends to decrease with the increase of flight altitude. In contrast, in the bundle block with a large remaining lens correction error, flight altitude increments will tend to improve the resulting accuracy.
- f. *What is the effect of motion blur on photogrammetric image processing?*
The increase in the degree of motion blur on the images can reduce the accuracy of the bundle block adjustment. The impact not only occurs in sparse point cloud products, but also in densified point cloud products. A higher number of GCPs, however, can be used to suppress the impact of motion blur on the resulting accuracy.
- g. *To what extent can the different blocks consisting of different flight altitudes and directions affect the overall accuracy of the self-calibration process?*

The cross strips addition is beneficial in reducing the systematic error in a bundle block that has a large systematic error remaining, as well as capable of suppressing the vertical distribution influence on the 4-GCP configuration at a lower flight altitude. The additional cross flights method is not recommended particularly when the bundle block already has a sufficient number of GCPs.

- h. *What is the significance of oblique image acquisition to the block deformation refinement?*
Oblique images will generate a rigid bundle block without substantial vertical error differences even if only a few GCPs or undistributed GCPs are available. This configuration has the best accuracy result compared with the other configurations of the Aibot X6.
- i. *What is the impact of the number of overlapping images on the quality of image orientation?*
Reducing the percentage of forward overlap inevitably aggravates the achievable accuracy of the bundle block. However, in the case of a bundle block with a large remaining lens correction error, instead aggravates the accuracy; the forward overlap reduction will improve the achievable accuracy, resulting a better accuracy than a bundle block with a higher forward overlap.
- j. *How efficient is the stop mode compared with the cruising mode, with regard to the resulting accuracy of and the time taken for the data acquisition?*
A stop mode acquisition can guarantee that the best quality image is obtained, although this method requires an extremely time-consuming process yet shorter battery life. These costs at a certain point will not be reciprocal to the increase in the achievable accuracy.
- k. *What parameters significantly influence the dense image matching process according to the pre-defined schemes?*
In the dense image matching process, highly blurred images can potentially reduce the achievable accuracy and the density of the dense point cloud. The surface type also influences the accuracy of densified point cloud; a rigid surface such as paving sett is likely to have a higher accuracy than a non-rigid surface such as grass. However, the dense image matching process will also be prone to error in an area with sudden feature changes yet lack of texture, a reflection of shadows on the water, and high contrast shadows.

7.2. Recommendation

The quality of the derived 3D data depends on the geometric and radiometric quality of the image. In spite of the fact that this research involves most of the named influence parameters, several parameters are still under-examined. The influence of, and ways to reduce, residual lens error need to be investigated thoroughly, especially in ultra-wide lenses. Neale, Hessel, and Terpstra (2011) have conducted research on how the distortion from various lens focal lengths of perspective lenses affected the resulting images, but not on an ultra-wide lens. Several lens model algorithms have also been developed for ultra-wide and fisheye lenses (Rueß et al., 2012; Schneider, Schwalbe, & Maas, 2009); however most of the algorithms are tested on a “hi-grade” consumer lens, not in a “recreational grade” lens as in DJI Phantom 2 camera.

The influence of the image radiometric quality is also not really observed in this research, especially in determining the relation of the image exposure to the resulting accuracy. At a certain level of exposure, the images are believed to fail in delivering sufficient texture to be used in the image matching process.

Based on the research limitation mentioned above, several recommendations can be given:

- a. Expanding a research in analysing the impact of lens correction residuals and explore a method to suppress the error. This research will somehow be beneficial to improve the achievable accuracy of the BBA gathered from a recreational class UAV.
- b. Developing a research in analysing a correlation of image exposures and their resulting BBA accuracies.

LIST OF REFERENCES

- Abdullah, Q. (2014). Ground Control Requirement. In *GEOG 892 - Geospatial Applications of Unmanned Aerial System (UAS)*. Pennsylvania: The Pennsylvania State University. Retrieved from <https://www.e-education.psu.edu/geog892/node/649>
- Aerolution. (2016). Songbird 1400. Retrieved January 26, 2016, from <http://www.aerolution-systems.com/products/songbird-1400/>
- Aerometrex. (2012). A brief history of aerial photogrammetry | From High Above. Retrieved September 16, 2015, from <http://aerometrex.com.au/blog/?p=203>
- Aibotix. (2015). Aibotix AiProFlight. Kassel: Aibotix GmbH. Retrieved from <https://www.aibotix.com/en/software-aioproflight.html>
- American Institute of Aeronautics and Astronautics. (2004). Recommended Practice: Terminology for Unmanned Aerial Vehicles and Remotely Operated Aircraft (AIAA R-103-2004). In *Recommended Practice: Terminology for Unmanned Aerial Vehicles and Remotely Operated Aircraft (AIAA R-103-2004)*. American Institute of Aeronautics and Astronautics, Inc. <http://doi.org/doi:10.2514/4.477072.001>
- ArcadiaSky. (2015). Drone, UAV Operator certification by country - ArcadiaSky. Retrieved August 5, 2015, from <https://www.arcadiasky.com/drone-zone/regulation/drone-uav-operator-certification-by-country/>
- Atkins, B. (2007). Modulation Transfer Function - what is it and why does it matter? Retrieved October 10, 2015, from <http://photo.net/learn/optics/mtf/>
- Avery, T. E., & Berlin, G. L. (1992). *Fundamentals of Remote Sensing and Airphoto Interpretation* (5th ed.). New York: Macmillan.
- Bailey, M. W. (2012). *Unmanned Aerial Vehicle Path Planning and Image Processing for Orthoimagery and Digital Surface Model Generation*. (Master's thesis). Vanderbilt University. Retrieved from http://etd.library.vanderbilt.edu/available/etd-11302012-151303/unrestricted/Mark_Bailey_Thesis.pdf
- Bay, H., Ess, A., Tuytelaars, T., & Van Gool, L. (2008). Speeded-Up Robust Features (SURF). *Computer Vision and Image Understanding*, 110(3), 346–359. <http://doi.org/10.1016/j.cviu.2007.09.014>
- BunceDirect. (2015). Sirius Pro. Retrieved September 30, 2015, from <http://buncedirect.mybigcommerce.com/sirius-pro/>
- Burns, R. (2011). *Photogrammetry*. Sacramento. Retrieved from <http://www.dot.ca.gov/hq/row/landsurveys/LSITWorkbook/09.pdf>
- Campbell, J. B. (2002). *Introduction to Remote Sensing* (3rd ed.). London: Taylor & Francis.
- Caroti, G., Martínez-Espejo Zaragoza, I., & Piemonte, A. (2015). Accuracy Assessment in Structure from Motion 3D Reconstruction from UAV-Born Images: the Influence of the Data Processing Methods. *ISPRS - International Archives of the Photogrammetry, Remote Sensing and Spatial Information Sciences, XL-1/W4*(December), 103–109. <http://doi.org/10.5194/isprsarchives-XL-1-W4-103-2015>
- Chiabrando, F., Nex, F., Piatti, D., & Rinaudo, F. (2011). UAV and RPV Systems for Photogrammetric Surveys in Archaeological Areas: Two Tests in the Piedmont Region (Italy). *Journal of Archaeological Science*, 38(3), 697–710. <http://doi.org/10.1016/j.jas.2010.10.022>
- CloudCompare. (2015). CloudCompare Wiki. Retrieved January 11, 2016, from http://www.cloudcompare.org/doc/wiki/index.php?title=Main_Page
- CloudCompare (Version 2.6.2 64-bit) [GPL computer software]. (2015). Retrieved from <http://cloudcompare.org/>
- Colomina, I., Blázquez, M., Molina, P., Parés, M. E., & Wis, M. (2008). Towards a New Paradigm for High-Resolution Low-Cost Photogrammetry and Remote Sensing. In J. Cheng, J. Jiang, & A.

- Baudoin (Eds.), *XXIst ISPRS Congress: Technical Commission I* (Vol. XXXVII Par, p. 1201). Beijing: International Society for Photogrammetry and Remote Sensing. Retrieved from http://www.isprs.org/proceedings/XXXVII/congress/1_pdf/205.pdf
- Colomina, I., & Molina, P. (2014). Unmanned Aerial Systems for Photogrammetry and Remote Sensing: a Review. *ISPRS Journal of Photogrammetry and Remote Sensing*, 92, 79–97. <http://doi.org/10.1016/j.isprsjprs.2014.02.013>
- Congalton, R. G., & Green, K. (2008). *Assessing the Accuracy of Remotely Sensed Data: Principles and Practices* (2nd ed.). CRC Press. Retrieved from <https://books.google.com/books?id=T4zj2bnGldEC&pgis=1>
- Cramer, M. (2010). The DGPF-Test on Digital Airborne Camera Evaluation – Overview and Test Design. *Photogrammetrie - Fernerkundung - Geoinformation*, 2010(2), 73–82. <http://doi.org/10.1127/1432-8364/2010/0041>
- Dong, L., & Shan, J. (2013). A Comprehensive Review of Earthquake - Induced Building Damage Detection with Remote Sensing Techniques. *ISPRS Journal of Photogrammetry and Remote Sensing*, 84, 85–99. <http://doi.org/10.1016/j.isprsjprs.2013.06.011>
- Edmund Optics. (2014). Distortion. Retrieved December 10, 2015, from <http://www.edmundoptics.com/technical-resources-center/imaging/distortion/>
- Eisenbeiß, H. (2009). *UAV Photogrammetry. Institute of Photogrammetry and Remote Sensing*. Zurich. <http://doi.org/doi:10.3929/ethz-a-005939264>
- Eisenbeiss, H., & Sauerbier, M. (2011). Investigation of UAV Systems and Flight Modes for Photogrammetric Applications. *The Photogrammetric Record*, 26(136), 400–421. <http://doi.org/10.1111/j.1477-9730.2011.00657.x>
- Eling, C., Klingbeil, L., & Kuhlmann, H. (2015). A Direct Georeferencing System for Real-Time Position and Attitude Determination of Lightweight UAVS. In *FIG Working Week 2015*. Sofia: International Federation of Surveyors. Retrieved from https://www.fig.net/resources/proceedings/fig_proceedings/fig2015/papers/ts04h/TS04H_eling_klingbeil_et_al_7631.pdf
- Esri. (2015). ArcGIS for Desktop (Version 10.3.1) [Computer software]. Environmental Systems Research Institute, Inc. (Esri). Retrieved from <http://www.esri.com/software/arcgis/arcgis-for-desktop>
- Fairfield, J. (2015). Drones Fitted with Cameras to be Banned in Thailand. Retrieved August 5, 2015, from http://tech.thaivisa.com/drones-fitted-cameras-banned-thailand/3290/?utm_source=newsletter-20150126-1523&utm_medium=email&utm_campaign=news
- Federal Geographic Data Committee. (1998). *Geospatial Positioning Accuracy Standards Part 3: National Standard for Spatial Data Accuracy*. Virginia. Retrieved from <https://www.fgdc.gov/standards/projects/FGDC-standards-projects/accuracy/part3/chapter3>
- Förstner, W. (1998). *On the Theoretical Accuracy of Multi Image Matching, Restoration and Triangulation*. Bonn: Universität Bonn. Retrieved from <http://citeseerx.ist.psu.edu/viewdoc/summary?doi=10.1.1.42.8370>
- Furukawa, Y., & Ponce, J. (2009). Accurate Camera Calibration from Multi-view Stereo and Bundle Adjustment. *International Journal of Computer Vision*, 84(3), 257–268. <http://doi.org/10.1007/s11263-009-0232-2>
- Gerke, M. (2015). Modern Image Calibration, Orientation and Matching [Powerpoint slides]. Retrieved from https://blackboard.utwente.nl/bbcswebdav/pid-846621-dt-content-rid-1675675_2/courses/M15-EOS-102/SfMvsPhoto_prezentation%281%29.pdf
- Gruber, M., Perko, R., & Ponticelli, M. (2004). the All Digital Photogrammetric Workflow : Redundancy and Robustness. In O. Altan (Ed.), *XXth ISPRS Congress : Technical Commission I*. Istanbul: International Society for Photogrammetry and Remote Sensing. Retrieved from <http://www.isprs.org/proceedings/XXXV/congress/comm1/papers/43.pdf>

- Haala, N. (2009). Comeback of Digital Image Matching. In D. Fritsch (Ed.), *Photogrammetric Week '09* (pp. 289–301). Heidelberg. Retrieved from <http://www.ifp.uni-stuttgart.de/publications/phowo09/290Haala.pdf>
- Häcki, M. (2014). Legal information about flying multicopter drone UAV in different countries. Retrieved August 5, 2015, from <http://www.riot.ch/en/legal-information-about-flying-multicopter-drones-commercial/>
- Imatest. (2015a). Imatest Master (Version 4.2.9) [Computer software]. Imatest LLC. Retrieved from <http://www.imatest.com/products/imatest-master/>
- Imatest. (2015b). Sharpness: What is it and how is it measured? Retrieved November 11, 2015, from <http://www.imatest.com/docs/sharpness/>
- Imatest. (2016). SFR results: Edge and MTF (Sharpness) plot. Retrieved February 12, 2016, from http://www.imatest.com/docs/sfr_mtfplot/
- Kadaster. (2015). Coordinate Transformation. Retrieved November 24, 2015, from <http://www.kadaster.nl/web/Thematis/Registraties/Rijksdriehoeksmeting/Transformatie-van-coordinaten.htm>
- Koebler, J. (2013). City in Virginia Becomes First to Pass Anti-Drone Legislation - U.S. News. Retrieved August 5, 2015, from <http://www.usnews.com/news/articles/2013/02/05/city-in-virginia-becomes-first-to-pass-anti-drone-legislation->
- Koren, N. (2013a). Introduction to resolution and MTF curves. Retrieved November 8, 2015, from <http://www.normankoren.com/Tutorials/MTF.html>
- Koren, N. (2013b). Lens testing. Retrieved December 1, 2015, from <http://www.normankoren.com/Tutorials/MTF5.html#using>
- Koren, N. (2013c). Understanding image sharpness: Resolution and MTF curves in film and lenses. Retrieved October 10, 2015, from <http://www.normankoren.com/Tutorials/MTF1A.html#diffraction>
- Kraus, K. (1993). *Photogrammetry: Fundamentals and Standard Processes*. (P. Stewardson, Trans.) (4th ed., Vol. 1). Bonn: Dümmler.
- Kraus, K. (2007). *Photogrammetry: Geometry from Images and Laser Scans*. (I. Harley & S. Kyle, Trans.) (2nd ed.). Berlin: De Gruyter.
- Kurtsev, O. (2008). Resolution and MTF. Retrieved November 23, 2015, from <http://www.quickmtf.com/about-resolution.html>
- Lembicz, B. W. (2006). Minimizing Ground Control When GPS Photogrammetry isn't Practical. In *ASPRS 2006 Annual Conference*. Nevada: American Society for Photogrammetry and Remote Sensing. Retrieved from <http://www.asprs.org/a/publications/proceedings/reno2006/0085.pdf>
- Leofoo. (2000). Depth of Field: One of the most important elements in photography. Retrieved October 16, 2015, from <http://www.mir.com.my/rb/photography/fototech/htmls/depth.html>
- Li, J., Li, E., Chen, Y., Xu, L., & Zhang, Y. (2010). Bundled Depth-map Merging for Multi-view Stereo. *Proceedings of the IEEE Computer Society Conference on Computer Vision and Pattern Recognition*, 2769–2776. <http://doi.org/10.1109/CVPR.2010.5540004>
- Lowe, D. G. (2004). Distinctive Image Features from Scale-Invariant Keypoints. *International Journal of Computer Vision*, 60(2), 91–110. <http://doi.org/10.1023/B:VISI.0000029664.99615.94>
- Luhmann, T., Fraser, C., & Maas, H.-G. (2015). Sensor Modelling and Camera Calibration for Close-range Photogrammetry. *ISPRS Journal of Photogrammetry and Remote Sensing*. <http://doi.org/10.1016/j.isprsjprs.2015.10.006>
- Magic Lantern. (2014). Magic Lantern (Version 2.3) [Camera firmware software]. Retrieved from

- <http://www.magiclantern.fm/>
- Mansurov, N. (2011). What is Chromatic Aberration? Retrieved February 10, 2016, from <https://photographylife.com/what-is-chromatic-aberration>
- Mansurov, N. (2013). What is Distortion? Retrieved November 18, 2015, from <https://photographylife.com/what-is-distortion>
- MarketsandMarkets. (2015). Unmanned Aerial Vehicles Market by Class (Small, Tactical, Strategic, Special Purpose), Subsystem (Data Link, GCS, and Software), Application (Military, Commercial and Homeland Security), Procurement by Purpose (Procurements, RDT&E, O&M), Payload & Geogra. Retrieved February 4, 2016, from <http://www.marketsandmarkets.com/Market-Reports/unmanned-aerial-vehicles-uav-market-662.html>
- Martinec, E. (2008). Noise, Dynamic Range and Bit Depth in Digital SLRs. Retrieved October 20, 2015, from <http://theory.uchicago.edu/~ejm/pix/20d/tests/noise/>
- MAVinci. (2015). SIRIUS PRO Surveying UAS. Retrieved December 28, 2015, from <http://www.mavinci.de/en/siriuspro>
- Mount, D., & Arya, S. (2010). Approximate Nearest Neighbors Library (Version 1.1.2) [LGPL computer software]. The University of Maryland. Retrieved from <http://www.cs.umd.edu/~mount/ANN/>
- Navipedia. (2014a). Accuracy. Retrieved November 9, 2015, from <http://www.navipedia.net/index.php/Accuracy>
- Navipedia. (2014b). Real Time Kinematics. Retrieved January 28, 2016, from http://www.navipedia.net/index.php/Real_Time_Kinematics
- Neale, W. T., Hessel, D., & Terpstra, T. (2011). *Photogrammetric Measurement Error Associated with Lens Distortion* (No. 2011-01-0286). Englewood. Retrieved from <http://www.sae.org/technical/papers/2011-01-0286>
- Newhall, B. (1969). *Airborne Camera: The World from the Air and Outer Space*. London: the Focal Press.
- Nocerino, E., Menna, F., Remondino, F., & Lunazzi, R. S. (2013). Accuracy and Block Deformation Analysis in Automatic UAV and Terrestrial Photogrammetry - Lesson Learnt. In P. Grussenmeyer (Ed.), *ISPRS Annals: XXIV International CIPA Symposium* (Vol. II-5/W1, pp. 203–208). Strasbourg: International Society for Photogrammetry and Remote Sensing. <http://doi.org/10.5194/isprsannals-II-5-W1-203-2013>
- NovAtel. (2016). OEM615™ Dual-Frequency GNSS Receiver. Retrieved January 28, 2016, from <http://www.novatel.com/products/gnss-receivers/oem-receiver-boards/oem6-receivers/oem615/>
- Ok, A. Ö., Wegner, J. D., Heipke, C., Rottensteiner, F., Soergel, U., & Toprak, V. (2011). In-Strip Matching and Reconstruction of Line Segments from UHR Aerial Image Triplets. In U. Stilla, F. Rottensteiner, H. Mayer, B. Jutzi, & M. Butenuth (Eds.), *Photogrammetric Image Analysis* (Vol. 6952, pp. 61–72). Berlin, Heidelberg: Springer Berlin Heidelberg. <http://doi.org/10.1007/978-3-642-24393-6>
- Pacey, R., & Fricker, P. (2005). Forward Motion Compensation (FMC) - Is It the Same in The Digital Imaging World? *Photogrammetric Engineering and Remote Sensing*, 71(11), 1241 – 1242. Retrieved from <http://www.asprs.org/a/publications/pers/2005journal/november/highlight1.pdf>
- Pix4D. (2015a). Pix4Dmapper Capture (Version 0.4.0) [Mobile application software]. Pix4D SA. Retrieved from <https://pix4d.com/pix4dmapper-app/>
- Pix4D. (2015b). Pix4Dmapper Pro (Version 2.0.100) [Computer software]. Pix4D SA. Retrieved from <https://pix4d.com/pix4dmapper-pro/>
- Przybilla, H.-J., & Wester-Ebbinghaus, W. (1979). Bildflug mit ferngelenkten Kleinflugzeug [Image Flight with Remote-controlled Light Aircraft]. *Bildmessung Und Luftbildwesen*, 47, 137–142.
- Remondino, F., Spera, M. G., Nocerino, E., Menna, F., Nex, F., & Gonizzi-Barsanti, S. (2013). Dense

- Image Matching: Comparisons and Analyses. In *Proceedings of the DigitalHeritage 2013 - Federating the 19th Int'l VSMM, 10th Eurographics GCH, and 2nd UNESCO Memory of the World Conferences, Plus Special Sessions fromCAA, Arqueologica 2.0 et al.* (Vol. 1, pp. 47–54).
<http://doi.org/10.1109/DigitalHeritage.2013.6743712>
- Rizaldy, A., & Firdaus, W. (2012). Direct Georeferencing: a New Standard in Photogrammetry for High Accuracy Mapping. *ISPRS - International Archives of the Photogrammetry, Remote Sensing and Spatial Information Sciences*, 39(September), 5–9. <http://doi.org/10.5194/isprsarchives-XXXIX-B1-5-2012>
- Rock, G., Ries, J. B., & Udelhoven, T. (2011). Sensitivity Analysis of Uav-Photogrammetry for Creating Digital Elevation Models (Dem). *ISPRS - International Archives of the Photogrammetry, Remote Sensing and Spatial Information Sciences*, XXXVIII-1/, 69–73. <http://doi.org/10.5194/isprsarchives-XXXVIII-1-C22-69-2011>
- Rueß, D., Lubert, a., Manthey, K., & Reulke, R. (2012). Accuracy Evaluation of Stereo Camera Systems With Generic Camera Models. *ISPRS - International Archives of the Photogrammetry, Remote Sensing and Spatial Information Sciences*, XXXIX-B5(September), 375–380. <http://doi.org/10.5194/isprsarchives-XXXIX-B5-375-2012>
- Schneider, D., Schwalbe, E., & Maas, H. G. (2009). Validation of Geometric Models for Fisheye Lenses. *ISPRS Journal of Photogrammetry and Remote Sensing*, 64(3), 259–266.
<http://doi.org/10.1016/j.isprsjprs.2009.01.001>
- Seitz, S. M., Curless, B., Diebel, J., Scharstein, D., & Szeliski, R. (2006). A Comparison and Evaluation of Multi-View Stereo Reconstruction Algorithms. *2006 IEEE Computer Society Conference on Computer Vision and Pattern Recognition - Volume 1 (CVPR'06)*, 1, 519–528.
<http://doi.org/10.1109/CVPR.2006.19>
- Sensefly. (2015). Sensefly Ebee RTK Brochure. Retrieved November 24, 2015, from https://www.sensefly.com/fileadmin/user_upload/sensefly/documents/brochures/eBee_RTk_en.pdf
- Shin, M. C., Goldgof, D. B., Bowyer, K. W., & Nikiforou, S. (2001). Comparison of Edge Detection Algorithms using a Structure from Motion Task. *IEEE Transactions on Systems, Man, and Cybernetics. Part B, Cybernetics: A Publication of the IEEE Systems, Man, and Cybernetics Society*, 31(4), 589–601.
<http://doi.org/10.1109/3477.938262>
- Sieberth, T., Wackrow, R., & Chandler, J. H. (2014). Motion Blur Disturbs - the Influence of Motion-blurred Images in Photogrammetry. *The Photogrammetric Record*, 29(148), 434–453.
<http://doi.org/10.1111/phor.12082>
- Tahar, K. N. (2015). Multi Rotor UAV at Different Altitudes for Slope Mapping Studies. *ISPRS - International Archives of the Photogrammetry, Remote Sensing and Spatial Information Sciences*, XL-1/W4, 9–16.
<http://doi.org/10.5194/isprsarchives-XL-1-W4-9-2015>
- Tahar, K. N., & Ahmad, A. (2013). An Evaluation on Fixed Wing and Multi-Rotor UAV Images using Photogrammetric Image Processing. *World Academy of Science, Engineering and Technology*, 7(1), 391–396. Retrieved from <http://www.waset.org/publications/11861>
- The Center for Photogrammetric Training. (2008). History of Photogrammetry. Retrieved September 16, 2015, from <https://spatial.curtin.edu.au/local/docs/HistoryOfPhotogrammetry.pdf>
- Trinidad and Tobago. Ministry of Finance and the Economy. (2013). Supply and Installation of an Unmanned Aerial Vehicle Mapping System and Terrestrial Laser Scanner for the Division of Lands and Surveys, Ministry of Housing, Land and Marine Affairs, Government of the Republic of Trinidad and Tobago (GORTT). Retrieved May 28, 2015, from <http://www.finance.gov.tt/wp-content/uploads/2013/11/Supply-and-Installation-of-an-Unmanned-Aerial-Vehicle-Mapping-System-and-Terrestrial-Laser-Scanner-.pdf>
- UAV Insider. (2015). Aibotix X6. Retrieved September 30, 2015, from <http://www.uavinsider.com/aibotix-x6-and-leica-geosystems-partnership/>

- Udin, W. S., & Ahmad, A. (2014). Assessment of Photogrammetric Mapping Accuracy Based on Variation Flying Altitude Using Unmanned Aerial Vehicle. *IOP Conference Series: Earth and Environmental Science*, 18, 012027. <http://doi.org/10.1088/1755-1315/18/1/012027>
- Unmanned Aerial Vehicle System Association. (2015). Advantages of UAVs. Retrieved May 29, 2015, from <https://www.uavs.org/advantages>
- Vallet, J., Panissod, F., Strecha, C., & Tracol, M. (2011). Photogrammetric Performance of an Ultra Light Weight Swinglet UAV. In *UAV-g*. Zürich. Retrieved from https://www.sensefly.com/fileadmin/user_upload/images/newsandpress/Paper-vallet_UAVg.pdf
- Vosselman, G., & Dijkman, S. (2001). 3D Building Model Reconstruction from Point Clouds and Ground Plans. In M. A. Hofton (Ed.), *International Archives of Photogrammetry and Remote Sensing* (Vol. XXXIV–3/W4, pp. 22–24). Annapolis. Retrieved from <http://www.isprs.org/proceedings/xxxiv/3-w4/pdf/vosselman.pdf>
- Warner, T. A., Nellis, M. D., & Foody, G. M. (2009). Remote Sensing Scale and Data Selection Issues. In T. A. Warner, M. D. Nellis, & G. M. Foody (Eds.), *The SAGE Handbook of Remote Sensing* (Vol. 2, p. 568). London: SAGE Publications. Retrieved from <https://books.google.com/books?id=uIv82prTp4IC&pgis=1>
- Wester-Ebbinghaus, W. (1980). Aerial Photography by Radio Controlled Model Helicopter. *The Photogrammetric Record*, 10(55), 85–92. <http://doi.org/10.1111/j.1477-9730.1980.tb00006.x>
- Westoby, M. J., Brasington, J., Glasser, N. F., Hambrey, M. J., & Reynolds, J. M. (2012). “Structure-from-Motion” photogrammetry: A low-cost, effective tool for geoscience applications. *Geomorphology*, 179, 300–314. <http://doi.org/10.1016/j.geomorph.2012.08.021>
- Who. (2013). NO DRONES: Iowa City Passes Uncommon Ordinance - Who TV. Retrieved August 5, 2015, from <http://whotv.com/2013/06/19/no-drones-iowa-city-passes-uncommon-ordinance/>

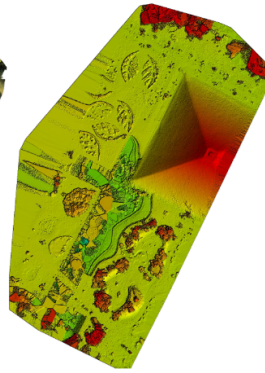
APPENDICES

1. The resulting Orthomosaic, DEM before densification process, and the number of overlapping images in all flight configurations (based on the Quality Report of 5-GCPs configuration)

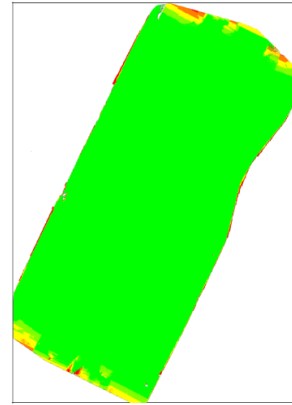
Aibot X6: Flight-1



Orthomosaic



Digital Surface Model (DSM) before densification

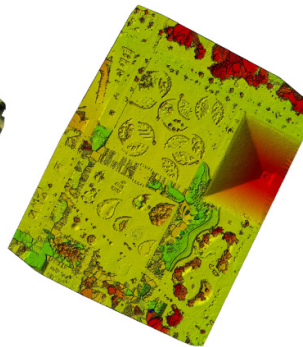


Number of overlapping images: 1 2 3 4 5+

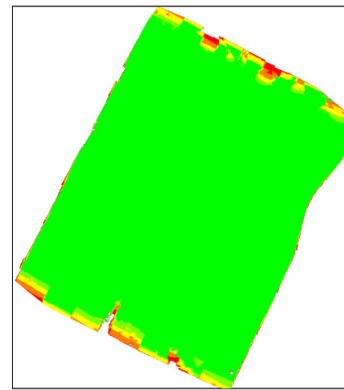
Aibot X6: Flight-2



Orthomosaic



Digital Surface Model (DSM) before densification

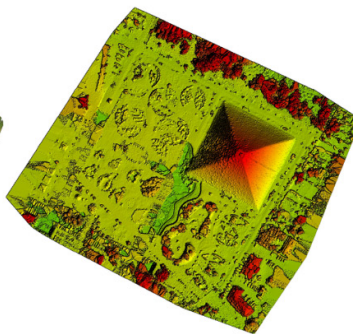


Number of overlapping images: 1 2 3 4 5+

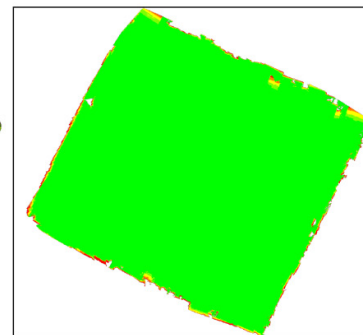
Aibot X6: Flight-3



Orthomosaic



Digital Surface Model (DSM) before densification

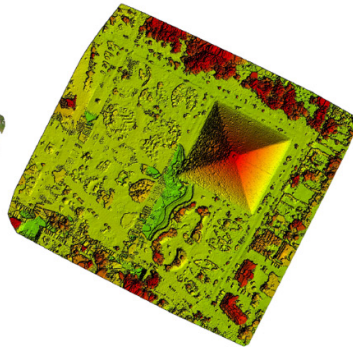


Number of overlapping images: 1 2 3 4 5+

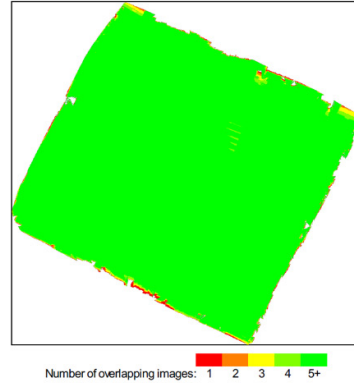
Aibot X6: Flight-4



Orthomosaic



Digital Surface Model (DSM) before densification

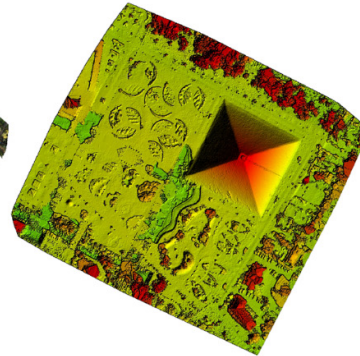


Number of overlapping images: 1 2 3 4 5+

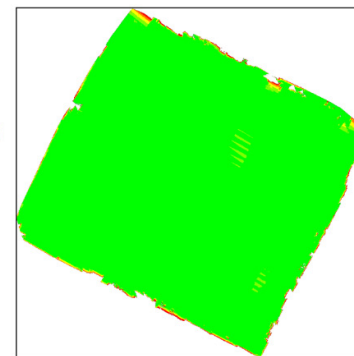
Aibot X6: Flight-5



Orthomosaic



Digital Surface Model (DSM) before densification

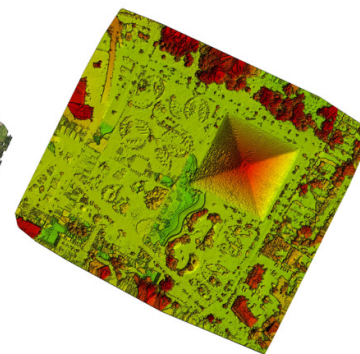


Number of overlapping images: 1 2 3 4 5+

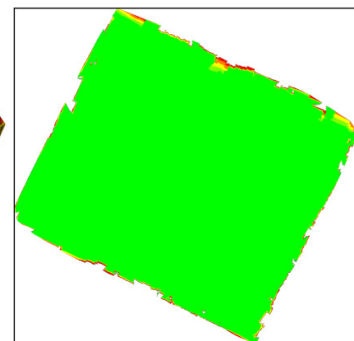
Aibot X6: Flight-6



Orthomosaic



Digital Surface Model (DSM) before densification

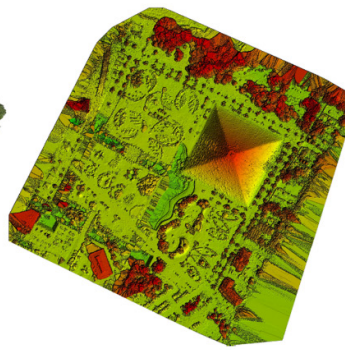


Number of overlapping images: 1 2 3 4 5+

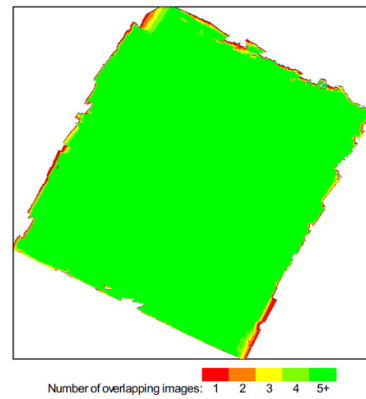
Aibot X6: Flight-7



Orthomosaic



Digital Surface Model (DSM) before densification

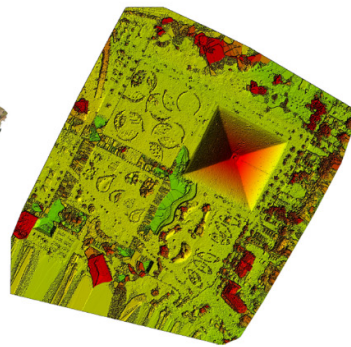


Number of overlapping images: 1 2 3 4 5+

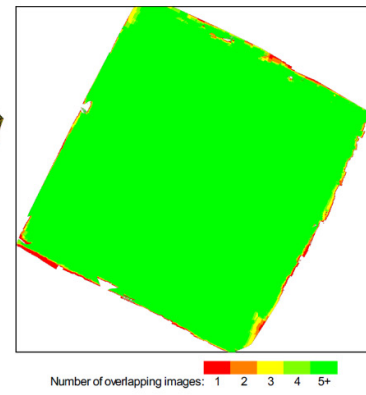
Aibot X6: Flight-8



Orthomosaic



Digital Surface Model (DSM) before densification

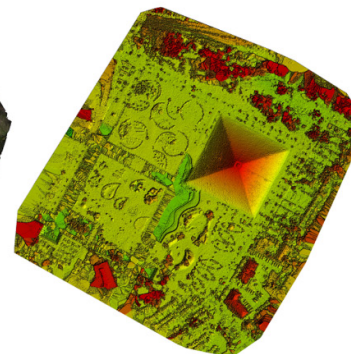


Number of overlapping images: 1 2 3 4 5+

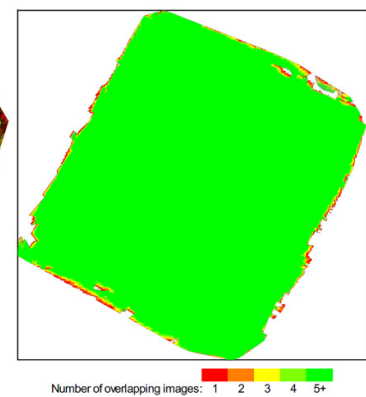
Aibot X6: Flight-9, 10, 11, 12 (Oblique images)



Orthomosaic



Digital Surface Model (DSM) before densification

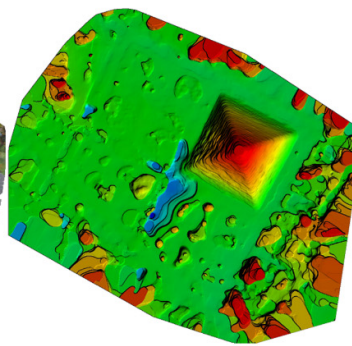


Number of overlapping images: 1 2 3 4 5+

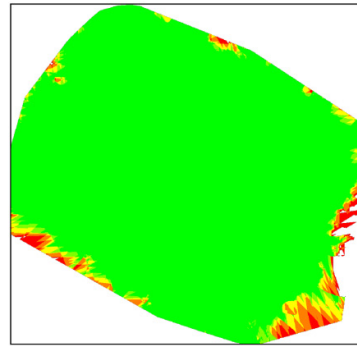
DJI Phantom 2 Vision+: Flight-13



Orthomosaic

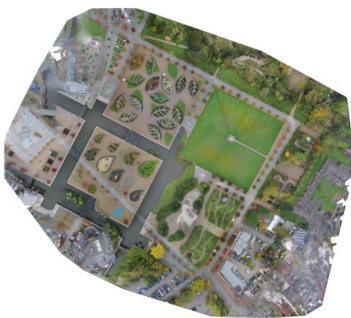


Digital Surface Model (DSM) before densification

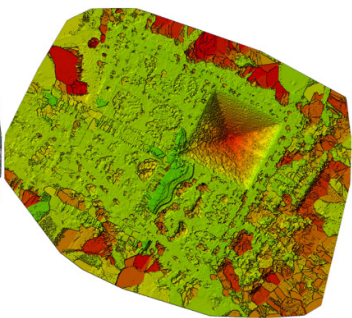


Number of overlapping images: 1 2 3 4 5+

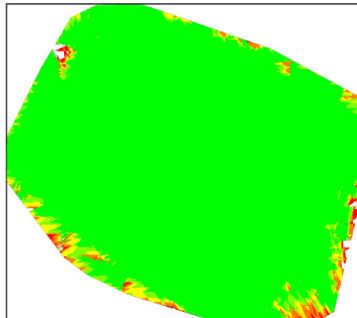
DJI Phantom 2 Vision+: Flight-14



Orthomosaic



Digital Surface Model (DSM) before densification

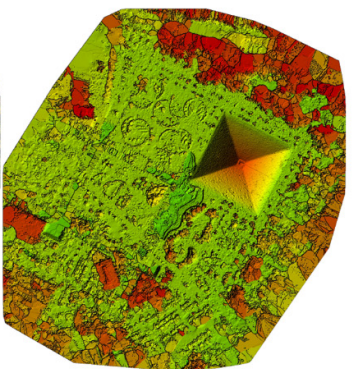


Number of overlapping images: 1 2 3 4 5+

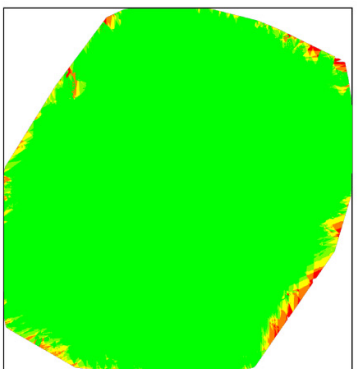
DJI Phantom 2 Vision+: Flight-15



Orthomosaic



Digital Surface Model (DSM) before densification

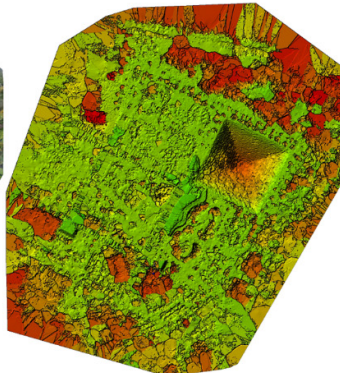


Number of overlapping images: 1 2 3 4 5+

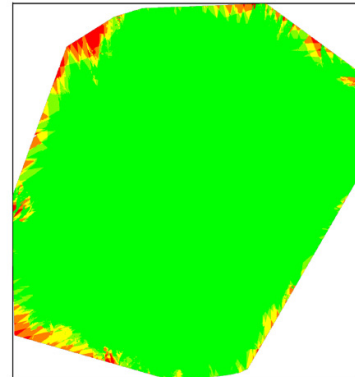
DJI Phantom 2 Vision+: Flight-16



Orthomosaic



Digital Surface Model (DSM) before densification

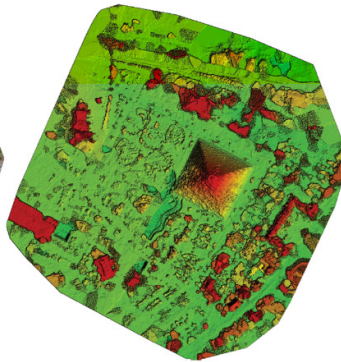


Number of overlapping images: 1 2 3 4 5+

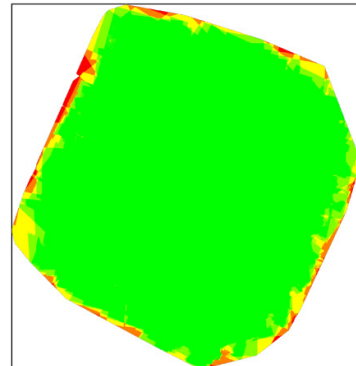
Ebee RTK: Flight-17



Orthomosaic



Digital Surface Model (DSM) before densification

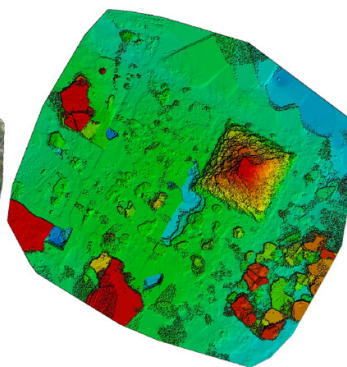


Number of overlapping images: 1 2 3 4 5+

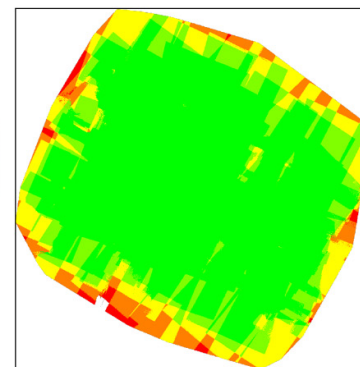
Ebee RTK: Flight-19



Orthomosaic



Digital Surface Model (DSM) before densification



Number of overlapping images: 1 2 3 4 5+

2. Residuals at checkpoints in different GCP configurations

Flight Config.	Num. of GCPs		σ X (cm)	σ Y (cm)	σ Z (cm)
1	0	Sigma	-	-	-
		RMSE	-	-	-
	4	Sigma	1.52	1.31	3.07
		RMSE	2.64	2.01	3.16
	5	Sigma	1.07	1.12	2.92
		RMSE	1.24	1.42	3.66
	5	Sigma	3.56	1.65	5.94
		RMSE	4.54	2.84	7.88
	Undist.	Sigma	-	-	-
		RMSE	-	-	-
2	0	Sigma	13.78	12.96	14.48
		RMSE	39.50	97.67	129.42
	4	Sigma	2.04	2.00	7.01
		RMSE	2.07	2.13	7.83
	5	Sigma	1.63	1.51	3.50
		RMSE	3.12	3.11	8.21
	5	Sigma	3.74	2.55	8.00
		RMSE	5.07	2.61	12.22
	Undist.	Sigma	1.70	1.42	2.95
		RMSE	1.77	2.18	3.36
3	0	Sigma	10.79	13.20	21.40
		RMSE	48.27	61.17	136.02
	4	Sigma	1.16	1.35	3.56
		RMSE	1.21	1.48	11.54
	5	Sigma	1.14	1.31	2.27
		RMSE	1.25	1.35	2.90
	5	Sigma	2.29	2.26	2.33
		RMSE	2.29	2.87	2.63
	Undist.	Sigma	1.27	1.30	1.78
		RMSE	1.30	1.56	1.90
4	0	Sigma	31.07	32.56	45.53
		RMSE	79.15	89.95	72.37
	4	Sigma	2.03	1.15	5.81
		RMSE	2.34	1.20	17.98
	5	Sigma	1.41	1.11	1.50
		RMSE	1.44	1.42	1.51
	5	Sigma	2.80	2.49	2.99
		RMSE	3.32	3.31	3.63
	Undist.	Sigma	1.08	1.15	1.72
		RMSE	1.08	1.39	1.75
5	0	Sigma	39.94	37.80	14.23
		RMSE	51.78	105.67	98.01
	4	Sigma	1.72	1.85	8.00
		RMSE	1.75	1.87	22.75
	5	Sigma	1.64	1.87	2.49
		RMSE	1.68	1.88	2.70
	5	Sigma	2.12	2.17	2.22
		RMSE	2.13	2.75	2.43
	Undist.	Sigma	1.57	1.47	2.12
		RMSE	1.69	2.35	2.55
6	0	Sigma	27.28	28.29	32.36
		RMSE	105.70	37.73	32.51
	4	Sigma	2.83	8.68	5.03
		RMSE	3.07	8.85	13.28
	5	Sigma	1.35	1.15	1.67
		RMSE	1.38	1.34	1.76
	5	Sigma	2.45	2.47	1.82
		RMSE	3.22	3.31	2.99
	Undist.	Sigma	1.37	0.90	2.19
		RMSE	1.37	1.31	2.35
8	0	Sigma	33.55	37.42	31.02
		RMSE	115.92	39.95	205.83
	4	Sigma	1.18	1.39	2.89
		RMSE	1.38	1.90	8.03
	5	Sigma	1.20	1.35	2.37
		RMSE	1.28	1.51	2.49
	5	Sigma	1.57	1.59	6.60
		RMSE	1.74	2.77	7.84
	Undist.	Sigma	1.18	1.36	2.43
		RMSE	1.22	1.77	2.51
13	0	Sigma	22.44	20.93	61.34
		RMSE	42.35	172.45	1260.37
	4	Sigma	10.23	10.97	11.77
		RMSE	11.19	11.10	11.77
	5	Sigma	11.45	10.54	9.44
		RMSE	11.62	10.82	18.19
	5	Sigma	20.92	12.63	7.92
		RMSE	29.09	16.76	9.88
	Undist.	Sigma	8.66	5.87	6.58
		RMSE	8.67	6.08	6.63
14	0	Sigma	27.26	19.96	92.08
		RMSE	27.29	159.11	842.58
	4	Sigma	11.20	9.36	10.59
		RMSE	11.75	9.62	21.11
	5	Sigma	11.16	9.54	7.68
		RMSE	11.20	9.54	12.73
	5	Sigma	19.10	8.91	9.19
		RMSE	28.39	12.63	13.17
	Undist.	Sigma	6.59	4.73	5.87
		RMSE	6.78	4.80	6.03
15	0	Sigma	46.76	34.79	166.81
		RMSE	53.50	236.04	735.06
	4	Sigma	9.79	5.98	8.31
		RMSE	11.96	6.06	16.64
	5	Sigma	9.15	6.15	6.42
		RMSE	9.60	6.34	17.33
	5	Sigma	12.13	7.10	9.88
		RMSE	17.12	7.72	11.23
	Undist.	Sigma	7.20	6.09	2.96
		RMSE	8.10	6.30	4.62
16	0	Sigma	25.80	26.37	38.08
		RMSE	96.28	65.24	657.76
	4	Sigma	10.62	6.47	12.98
		RMSE	13.56	7.95	41.85
	5	Sigma	9.86	6.48	6.84
		RMSE	10.46	6.61	15.52
	5	Sigma	13.87	8.48	9.53
		RMSE	21.18	11.54	10.40
	Undist.	Sigma	6.36	5.03	2.98
		RMSE	7.11	5.08	4.91
17	0	Sigma	1.95	1.45	2.51
		RMSE	12.77	1.45	16.69
	4	Sigma	2.06	1.53	1.79
		RMSE	2.08	1.54	2.35
	5	Sigma	2.10	1.41	1.79
		RMSE	2.15	1.61	1.90
	5	Sigma	1.20	1.51	2.40
		RMSE	2.44	1.52	2.40
	Undist.	Sigma	2.14	1.69	1.61
		RMSE	2.17	1.87	1.63

7	0	Sigma	31.12	39.67	8.86
		RMSE	51.42	63.51	30.46
	4	Sigma	1.38	2.15	2.21
		RMSE	1.44	2.29	2.54
	5	Sigma	1.38	1.88	1.97
		RMSE	1.39	1.91	2.12
	5	Sigma	1.72	1.97	1.20
		RMSE	1.86	2.09	2.06
	Undist.	Sigma	1.56	1.37	2.07
		RMSE	1.57	1.44	2.08

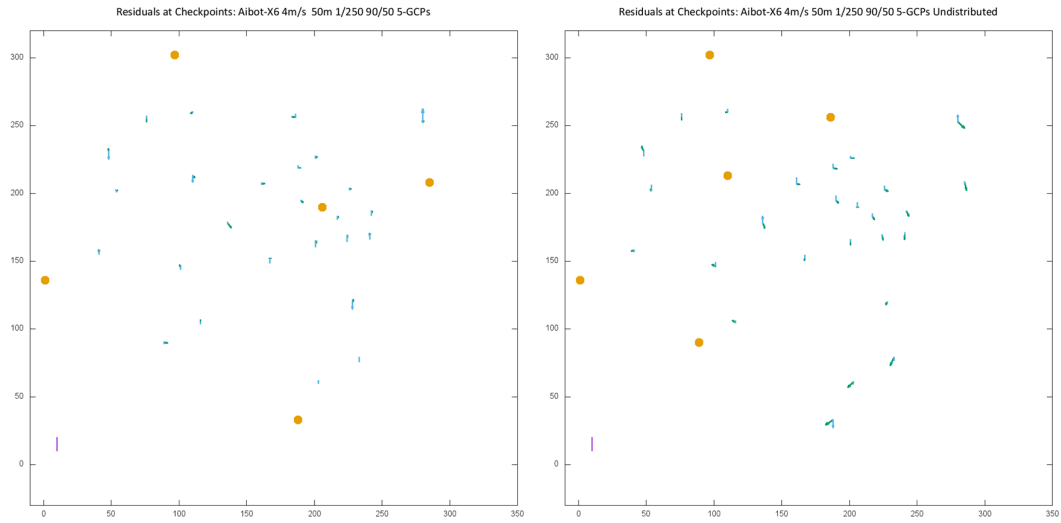
No RTK	0	Sigma	5.68	5.91	6.42
		RMSE	14.91	7.45	19.19
	4	Sigma	2.06	1.58	4.16
		RMSE	2.06	1.58	11.33
	5	Sigma	2.12	1.54	2.59
		RMSE	2.12	1.65	2.65
	5	Sigma	1.59	2.33	6.92
		RMSE	2.91	2.76	7.13
	Undist.	Sigma	2.42	1.69	2.43
		RMSE	2.42	2.07	2.55

3. Residuals plot of 5 well-distributed GCPs and undistributed GCPs in every flight number

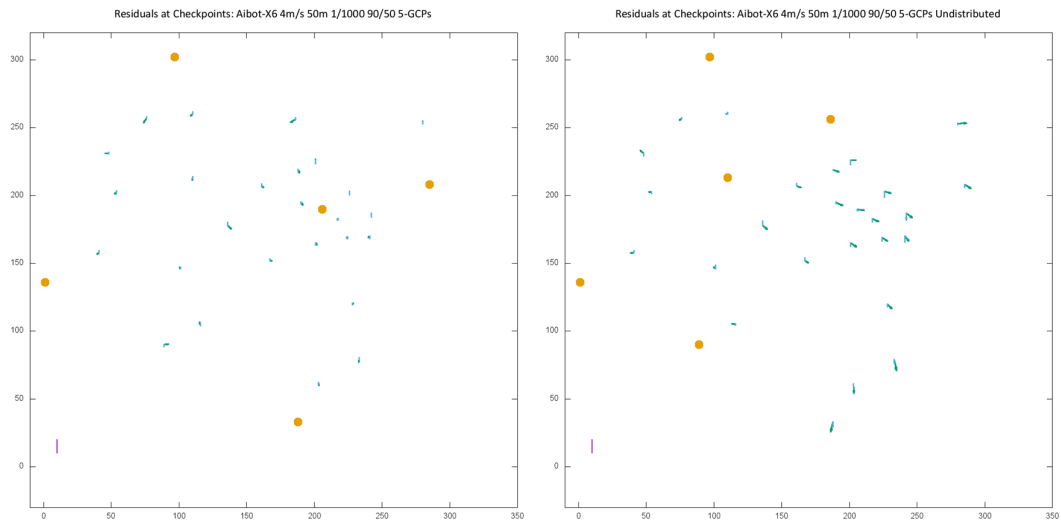
Evenly distributed 5-GCPs

Unevenly distributed 5-GCPs

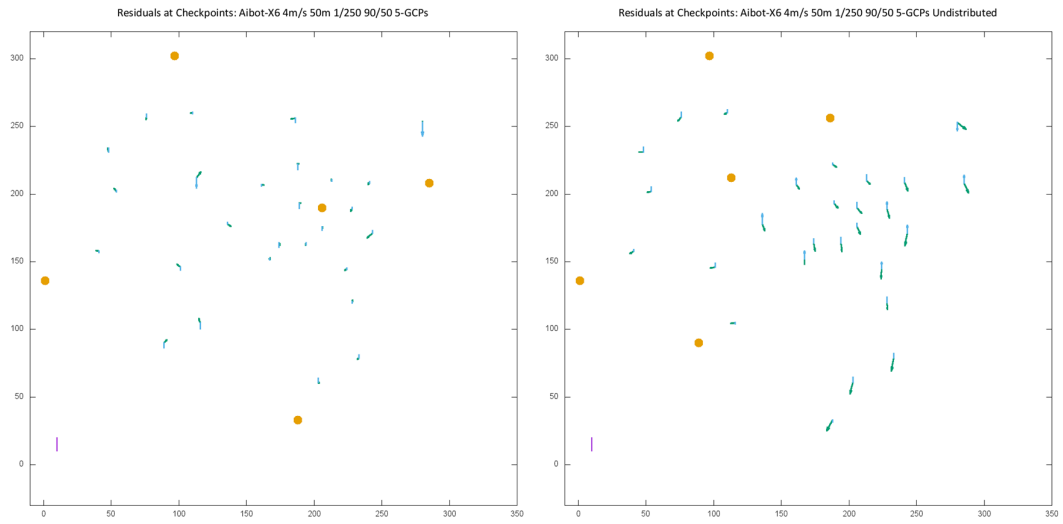
Aibot X6: Flight-3



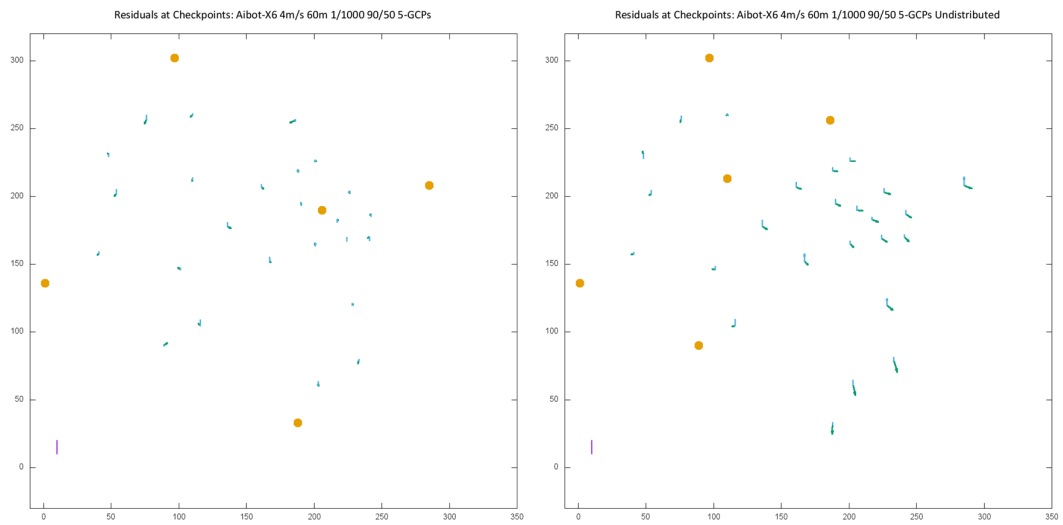
Aibot X6: Flight-4



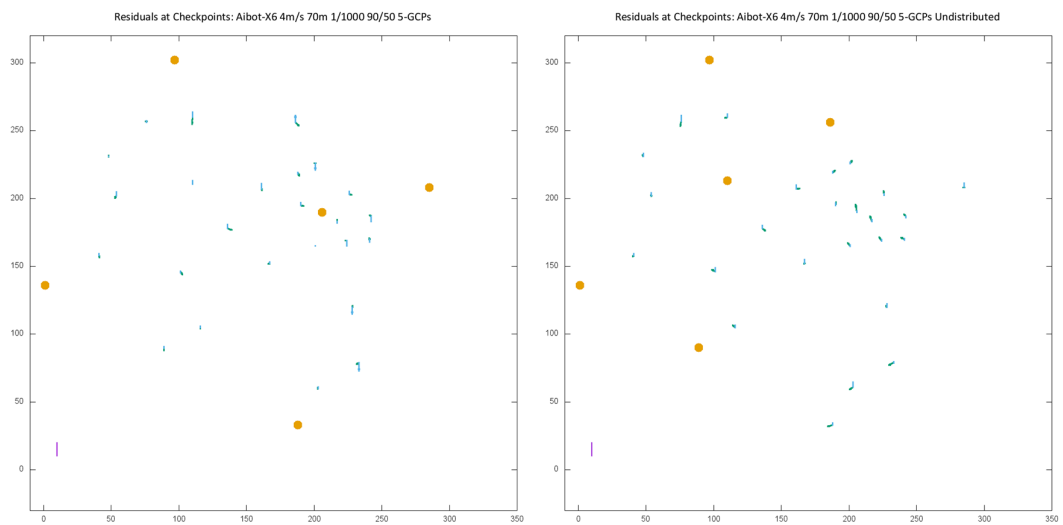
Aibot X6: Flight-5



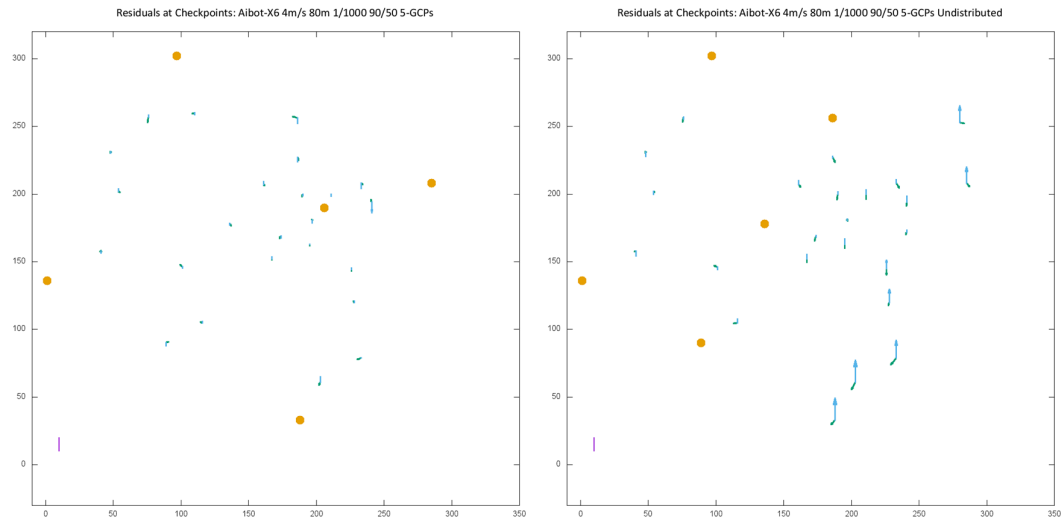
Aibot X6: Flight-6



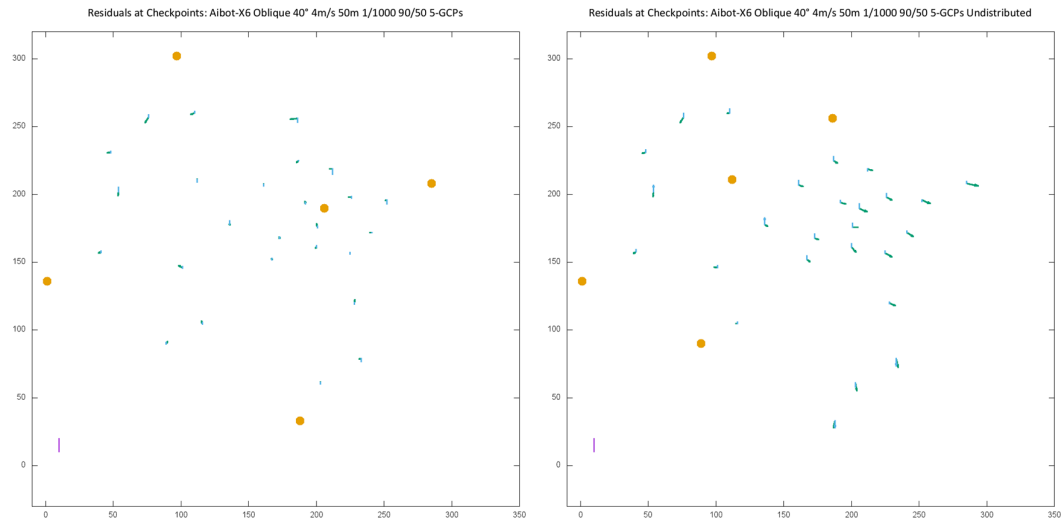
Aibot X6: Flight-7



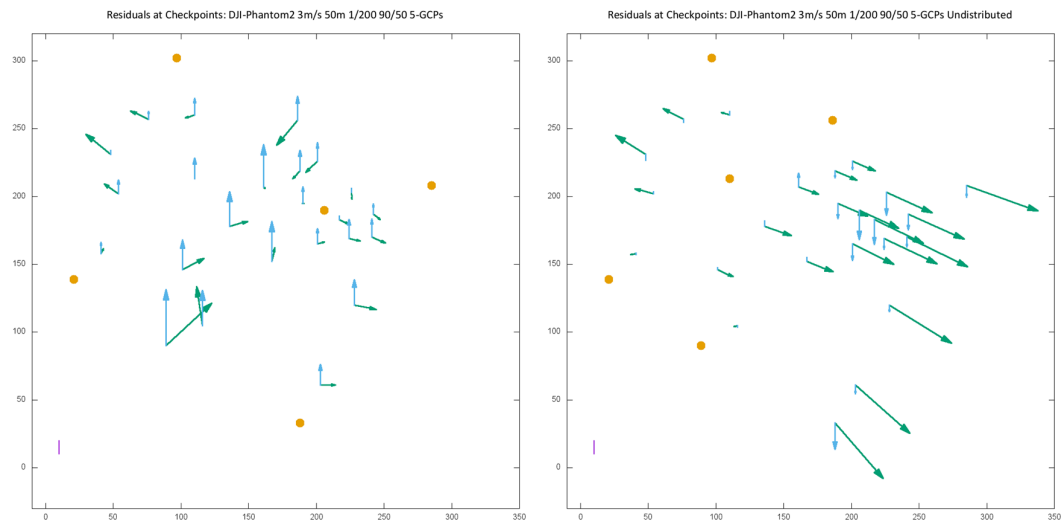
Aibot X6: Flight-8



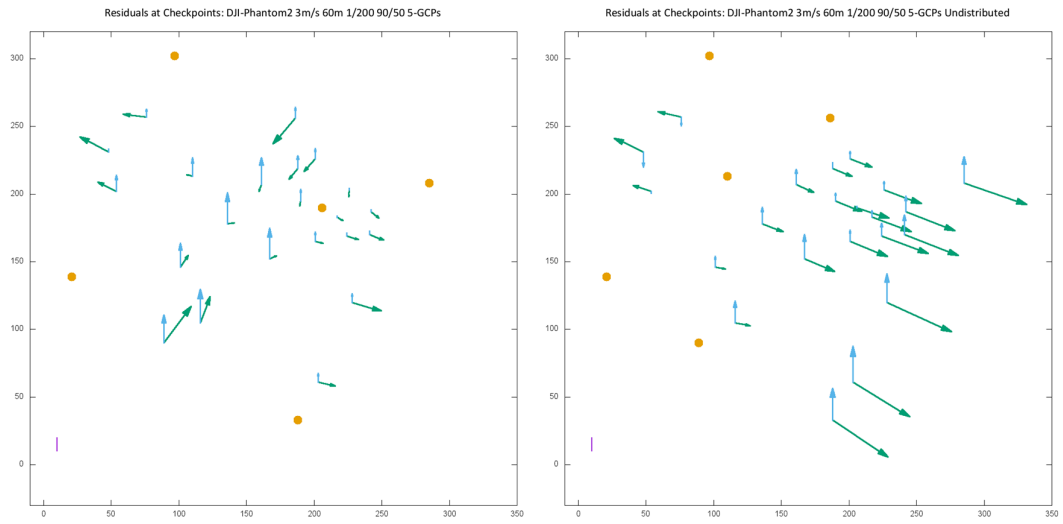
Aibot X6: Oblique images (Flight 9, 10, 11, 12)



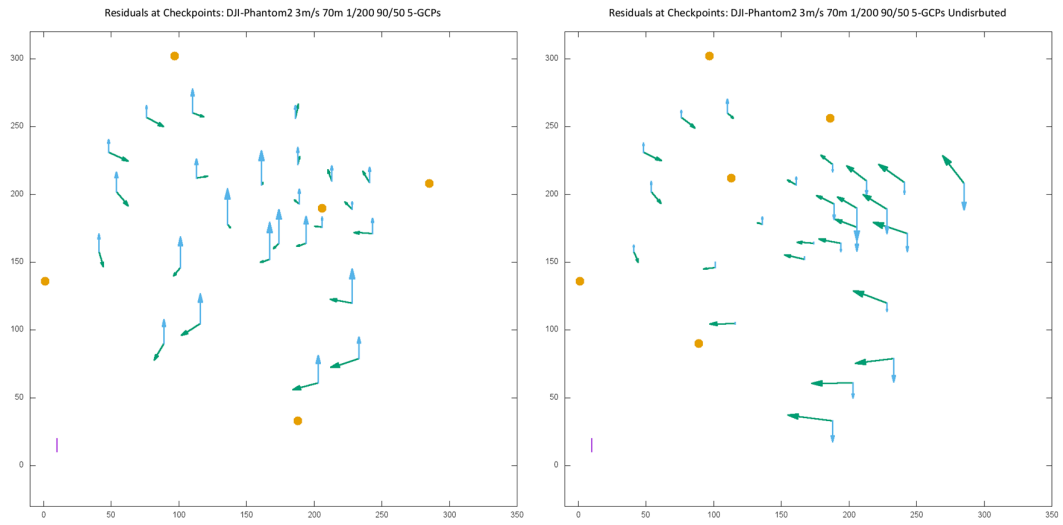
DJI Phantom 2 Vision+: Flight-13



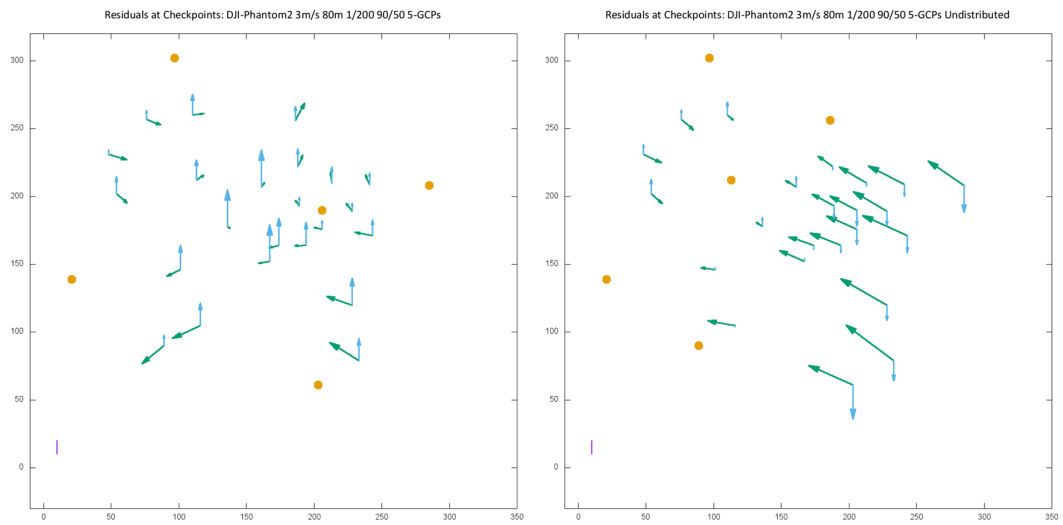
DJI Phantom 2 Vision+: Flight-14



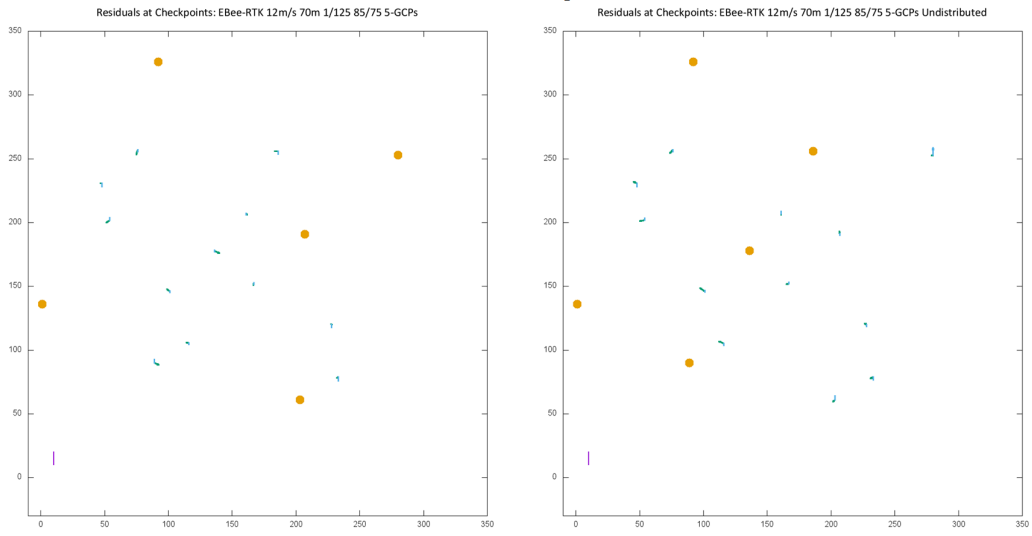
DJI Phantom 2 Vision+: Flight-15



DJI Phantom 2 Vision+: Flight-16



Ebee RTK: Flight-17



4. The Sigma of the theoretical vertical accuracy and the actual vertical accuracy in every GCPs configuration (in Centimetres)

